Lithospheric Structure beneath the Colorado Rocky Mountains and Support for High Elevations

by

Jonathan MacCarthy

Submitted in Partial Fulfillment

of the Requirements for the Degree of

Doctor of Philosophy in Earth and Environmental Science

with Dissertation in Geophysics

New Mexico Institute of Mining and Technology

Socorro, New Mexico

December, 2010

Science does not know its debt to imagination.

Ralph Waldo Emerson

ABSTRACT

The Southern Rocky Mountains (SRM) have long been the object of fascination in western US geology. Their enigmatic high elevations (>2.5 km), above an already high broad Cenozoic orogenic plateau, and cryptic uplift history have motivated much speculation on the source and timing uplift. The CREST (Colorado Rockies Experiment and Seismic Transects) project represents the highest resolution seismic experiment yet deployed to address these questions, and indeed CREST is a uniquely high–quality dataset among temporary broadband deployments in the world. This dissertation is primarily focussed on leveraging the scientific facility that CREST provides in order to interrogate the 3D architecture and state of the upper mantle beneath the SRM from body wave tomography, and also to develop new tomography tools to do so. These data are used to develop a method for simultaneous inversion of teleseismic travel time and gravity data, as well as to exploit emerging stochastic matrix diagonal estimation methods to produce estimates of the resolution matrix diagonal for large geophysical inverse problems.

Keywords: lithosphere; Colorado; seismic tomography; joint inversion; Southern Rocky Mountains; mantle; resolution

ACKNOWLEDGMENTS

I'd first like to thank my advisor, Rick Aster. His support and encouragement has made this work possible during the last four and a half years, and his example of thoughtfulness, fairness, and professionalism will serve me many more. Equally important has been the support of my family. Particularly my wife, Megan, who has made my life as easy as possible in the pursuit of my degree. I am forever indebted.

Thanks also to my committee, Susan Bilek, Brian Borchers, Kent Condie, and Charlotte Rowe, for your unwavering support, patience, and advocacy. I owe much to the greater CREST Team, but particularly Ken Dueker, Steve Hansen, and Josh Stachnik for many insightful scientific conversions and for logistical support during station deployment. Also, Noël Barstow, Eliana Arias-Dotson, and Michael Johnson for indispensable support in the field and with data. Finally, enduring gratitude goes to my friends at NMT,especially Hunter and James Knox, and Julien Chaput, who have made all other things possible, and made the impossible things bearable.

The CREST project is funded by the National Science Foundation Continental Dynamics Program under award EAR-0607693. Additional travel and project support came from the New Mexico Tech Grad. Student Association, IRIS, AGU, and SSA.

This dissertation was typeset with LaTeX[1] by the author.

[1]The LaTeX document preparation system was developed by Leslie Lamport as a special ver-

sion of Donald Knuth's TEX program for computer typesetting. TEX is a trademark of the American Mathematical Society. The LATEX macro package for the New Mexico Institute of Mining and Technology dissertation format was written for the Tech Computer Center by John W. Shipman.

CONTENTS

LIST OF FIGURES

This dissertation is accepted on behalf of the faculty of the Institute by the following committee:

Richard C. Aster, Advisor

I release this document to the New Mexico Institute of Mining and Technology.

Jonathan MacCarthy Date

CHAPTER 1

INTRODUCTION

Advances in seismological techniques and instrumentation during the past 20 years have resulted in a dramatic uncovering of the lithosphere-scale structure of the Earth. These studies reveal that the uppermost mantle that makes up the asthenosphere and lithosphere is rich with structures that reflect both ongoing thermal and/or fluid processes, and the record of ancient continent building and altering events. The western United States is a particularly intriguing area for such investigations because of an exceptionally broad plate boundary zone that extends from the Pacific-North America plate boundary to the Great Plains.

Recent tomographic seismic imaging of the western United States (Burdick et al., 2009; Obrebski et al., 2010; Schmandt & Humphreys, 2010) verifies earlier images showing low velocity zones in the mantle co-located with structurally or geochemically defined crustal province boundaries that are possible sutures from Proterozoic continental assembly (Dueker et al., 2001; Karlstrom et al., 2002; Yuan & Dueker, 2005) (Figure 1.1). Low velocities in the mantle beneath western Colorado underlie the highest elevations in the Colorado Rocky Mountains, and are also associated with a possible inherited Proterozoic feature in the lithosphere that is within the Colorado Mineral belt (COMB) (Tweto & Sims, 1963; MCCOY et al., 2005) (Figure 1.2). We are motivated by the coincidence of high topography, evidence of Cenozoic uplift, slow mantle velocities, magmatism, and inherited

Proterozoic lithospheric structure, that together suggest that these low velocities may be a significant geodynamic influence on the evolution of the Southern Rocky Mountains through to the present day.

This dissertation is comprised of three efforts relating to tomographic interrogation of the upper mantle beneath Southern Rocky Mountains, and methodological contributions related to tomographic imaging, as applied to the CREST dataset. Chapter 2 presents high resolution tomographic results from teleseismic body wave imaging of the Southern Rocky Mountains upper mantle. These results, along with forthcoming discontinuity and surface wave imaging from CREST colleagues Ken Dueker, Steve Hansen, and Josh Stachnik, comprise the most extensive and highest resolution geophysical investigations yet of upper mantle architecture of the Southern Rocky Mountains. This chapter is in preparation for submission to the *Journal of Geophysical Research* with co–authors Rick Aster, Ken Dueker and other members of the CREST scientific team. Chapter 3 is a synthesis and application of new stochastic methods to estimate the diagonal of a large unavailable matrix, towards producing accurate estimates of the model resolution matrix and generalized cross validation (GCV) function in large geophysical inversions. The method was applied to the CREST teleseismic dataset. This chapter was submitted to *Geophsical Research Letters* with co–authors Brian Borchers, and Rick Aster. Chapter 4 describes the development of methods for joint inversion of teleseismic travel time and Bouguer gravity data, with applications in the Southern Rocky Mountains.

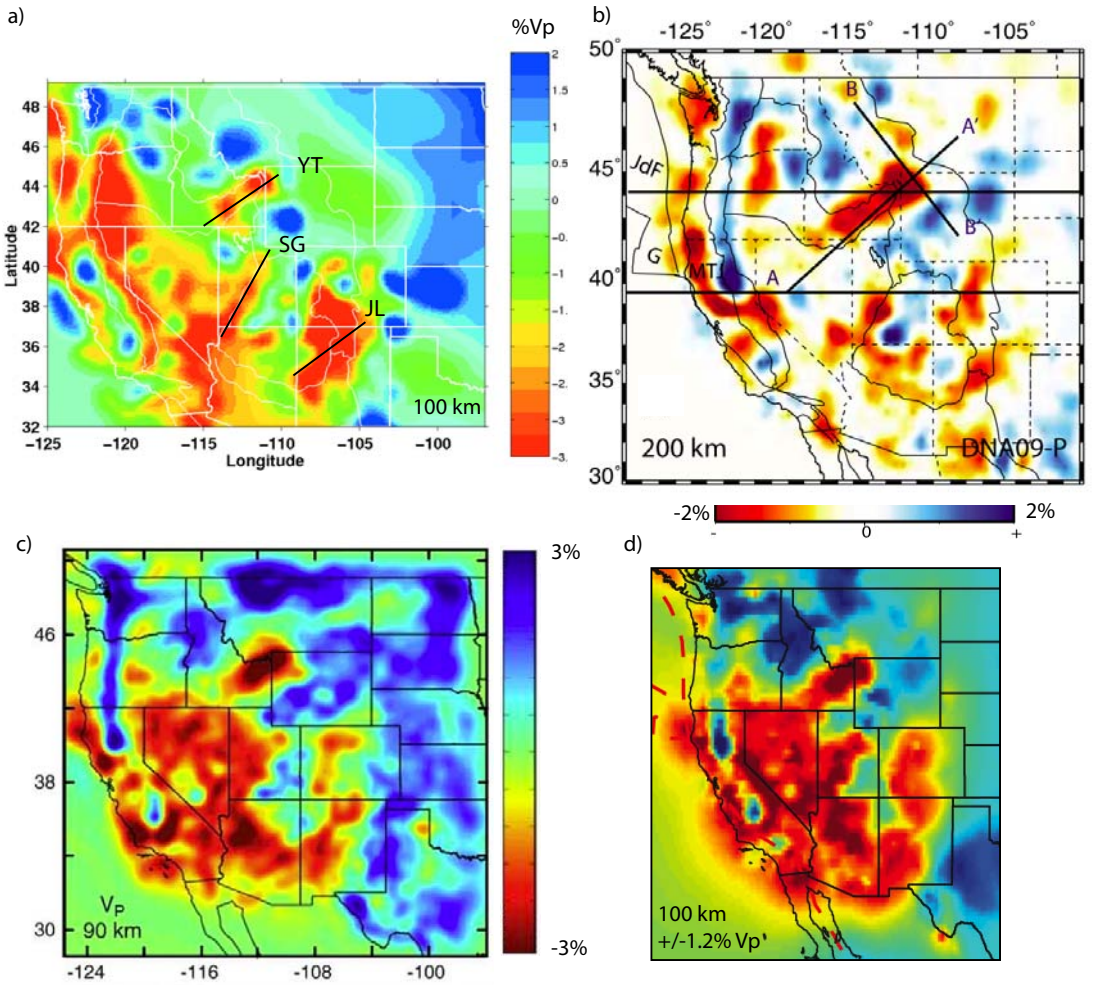

Figure 1.1: Compilation of earlier and recent western US scale P wave anomaly tomography. a) $\Delta\%V_p$ 100 km depth from Dueker et al. (2001), YT - Yellowstone trend, SG - Saint George volcanic trend, JL - Jemez Lineament, b) $\Delta\%V_p$ at 200 km from Obrebski et al. (2010), c) $\Delta\%V_p$ from Schmandt & Humphreys (2010), d) $\Delta\%V_p$ from Burdick et al. (2009)

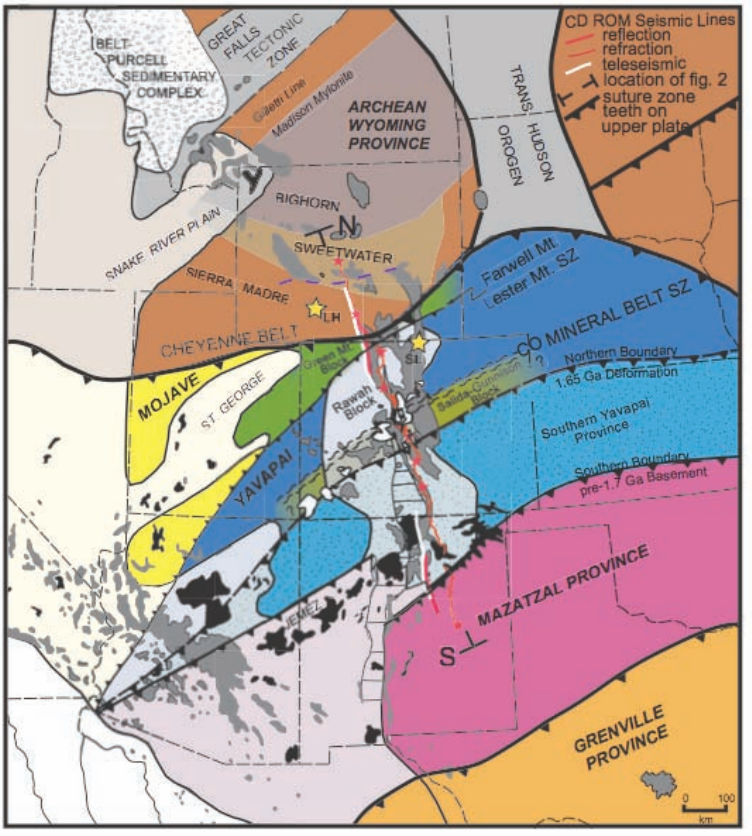

Figure 1.2: Geologic components of the Southern Rocky Mountains and adjacent regions (from Karlstrom et al. (2002)).

CHAPTER 2

UPPER MANTLE SUPPORT FOR HIGH ELEVATIONS BENEATH THE SOUTHERN ROCKY MOUNTAINS

Abstract

Recent estimates of crustal thickness and shear wave velocity from the CREST (Colorado Rockies Experiment and Seismic Transects) CD-ROM experiment indicate that the highest elevations of the Colorado Rocky Mountains ($<$ 2.5 km) are not primarily supported in the crust, and that mantle buoyancy and dynamics are therefore of fundamental importance. We present results of teleseismic body wave tomography of the upper mantle beneath western Colorado from CREST. Using a network of over 160 CREST and USArray stations with a minimum spacing of $\sim$24 km, we invert approximately 14,600 P– and 3,600 S–wave arrival times for regularized 3-D models of upper mantle V_p and V_s structure. We find V_p perturbations relative to AK135 of 7% and V_s variations of 8%, with structure being largely confined to the upper 300 km of the mantle. The previously identified broad "Aspen Anomaly" of low uppermost mantle velocities in this region is revealed to be bifurcated, with the lowest V_p and V_s velocities lying beneath the San Juan mountains being clearly distinct from low velocities associated with the northern Rio Grande Rift. The San Juan anomaly probably represents thermal and/or chemical heterogeneity in the uppermost mantle related to voluminous Cenozoic magmatism. A northeast-southeast grain in shallow V_s

parallel to the Colorado Mineral Belt may be controlled by uppermost mantle Proterozoic accretionary lithospheric architecture. We find that the low velocity anomalies beneath southwest Colorado in particular may provide significant support for high elevations.

2.1 Introduction

The Southern Rocky Mountain (SRM) orogenic plateau contains some of the highest average elevations in North America (McMillan et al., 2006), despite being approximately 1000 km from the North American/Pacific plate boundary. Support for this elevation in various locales has been attributed to thermal and/or chemical buoyancy contributions from the crust, (Li et al., 2002) [Stachnik et al., (in review)], uppermost mantle (Roy et al., 2004) (van Wijk et al., 2010), and deeper mantle (Moucha et al., 2008). Others have suggested that inherited pre-Laramide lithospheric structure may have a strong geodynamic influence on Laramide and subsequent deformation tectonics in the SRM (Karlstrom & Humphreys, 1998; Mutschler et al., 1998; Dueker et al., 2001; Karlstrom et al., 2002).

The importance of inherited structures has gained additional credence through increasingly high resolution tomographic images of the western US that confirm anomalously slow mantle beneath Proterozoic province boundaries, suggesting recent/present-day mantle modification and tectonic forcing in the Rocky Mountain corridor (Gao et al., 2004; Sine et al., 2008; Schmandt & Humphreys, 2010; Obrebski et al., 2010). Further supporting the hypothesis of young mantle reorganization are observations of late Miocene accelerated river incision (McMillan et al., 2006; Karlstrom et al., 2008), and tilted epierigenic flanks (McMillan et al.,

2002; Eaton, 2008). The SRM thus provides a view of processes attending the modification of old lithosphere by recent mantle influences, and the mechanisms by which this happens. Tomographic results from the CREST (Colorado Rockies Experiment and Seismic Transects) experiment illuminate the architecture and dynamics of the upper mantle of the SRM at a spatial resolution previously unachieved, and provide important constraints on the genesis of and mode of support for the Colorado Rocky Mountains.

2.1.1 Geological History

The SRM lithosphere is comprised of numerous accreted Proterozoic terranes of mixed oceanic and continental affinity, defined primarily by geochemistry (Bennett & Depaulo, 1987; Condie & Selverstone, 1999). The southern margin of Laurentia (present coordinates) was the locus of multiple arc and/or micro plate accretions, analogous to the present-day southeastern margin of Asia, beginning in the late Paleoproterozoic (Whitmeyer & Karlstrom, 2007). The Green Mountain (1.79–1.78 Ga (Condie & Shadel, 1984)) and Rawah (1.76–1.73 Ga (Premo & Van Schmus, 1989)) arc blocks were sutured onto the southern edge of the Archean Wyoming cratonic province along the Cheyenne belt, arcuate zone of thick crust, high Bouguer gravity (Crosswhite & Humphreys, 2003), and high velocity lithosphere (Yuan & Dueker, 2005) in southeastern Wyoming and far northwestern Colorado (CO). Teleseismic P wave tomography from Dueker & Yuan (2004) also imaged fast velocities of up to 4% south of the Cheyenne belt, beneath the Green Mountain and Rawah blocks (Figure 2.1).

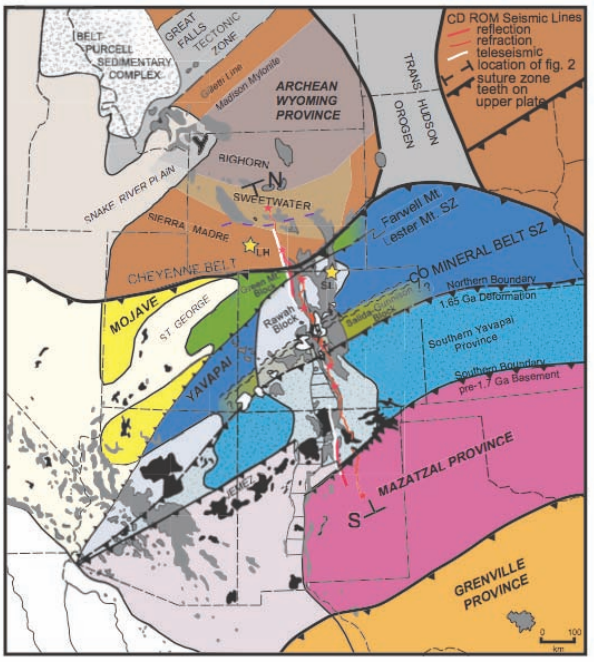

Figure 2.1: Geologic components of the Southern Rocky Mountains and adjacent regions (from Karlstrom et al. (2002)).

The Yavapai province was an amalgamation of mostly juvenile arc crust accreted south of the Wyoming province between 1.8 Ga and 1.7 Ga (Whitmeyer & Karlstrom, 2007), and it comprises the majority of CO lithosphere. Its southern border is in present day northern New Mexico, approximately coinciding with the Jemez volcanic lineament (Figure 2.1), but there is a notable internal boundary between the northern and southern Yavapai province. The Colorado Mineral Belt (COMB) is a $\sim$200 km wide zone of Proterozoic through Phanerozoic shearing and subvertical differential movement (MCCOY et al., 2005), low gravity (McCoy et al., 2004), mineralization (Tweto & Sims, 1963), and magmatism (Mutschler et al., 1998). This zone of persistent weakness, as well as other Proterozoic crustal province boundaries, has been hypothesized to have exerted geodynamic control over the partitioning of Laramide and younger lithospheric

modification (Karlstrom & Humphreys, 1998; Mutschler et al., 1998; Dueker et al., 2001; Karlstrom et al., 2002).

The SRM region was largely stable, with low relief and low elevation through the Paleozoic following Proterozoic continental assembly, with the exception of the block uplifts of the Ancestral Rocky Mountains in the Pennsylvanian (Kluth & Coney, 1981). This produced northwest–southeast oriented uplifts and basins in southwestern CO, which were subsequently largely eroded. At the end of the Mesozoic, the SRM and Colorado Plateau were near sea level (Elder & Kirkland, 1994). In the early to middle Cenozoic, rapid shallow subduction of an oceanic slab during the Laramide orogeny produced widespread deformation, hydration, refrigeration, and uplift of the western US lithosphere (Coney & Reynolds, 1977; Humphreys et al., 2003) as far east as the Front Range in CO, producing much of the elevation and topography of the present CP and SRM. The precise timing and mode of uplift is still the subject of intense debate (Livaccari & Perry, 1993; Spencer, 1996; Roy et al., 2009; Morgan, 2003; Moucha et al., 2008)

During the Laramide, magmatism in CO was primarily limited to plutonism along the COMB, but extensive western US ignimbrite volcanism followed the presumed removal of the Farallon slab in the middle Tertiary (Coney & Reynolds, 1977). Volcanism in Colorado was pronounced beneath the San Juan volcanic field (Farmer et al., 2008), with numerous magmatic centers along the COMB and Rio Grande Rift (Mutschler et al., 1998).

2.1.2 Previous Geophysical Work

The Rocky Mountain Front (RMF) experiment was a deployment of 36 broadband seismometers in Colorado and western Kansas in 1991-1992. The stations had a nominal 100 km spacing and were deployed for approximately seven

months. The RMF experiment was designed to determine the scale and location of the transition from stable cratonic lithosphere to more modified tectonic lithosphere at the Colorado Rockies. Images from body wave tomography revealed pronounced low velocities above 250 km depth beneath the highest elevations in Colorado (-2%Vp and -4% V_s), and a sharp positive eastward velocity gradient 200 km east of the Front Range in the Kansas Great Plains (Lee & Grand, 1996; Lerner-Lam et al., 1998). Total V_s variation of 9% from beneath the Rockies to the Great Plains was interpreted as temperature variations of 350 C with 1% partial melt, assuming reasonable values of Q_β and velocity/density/melt scaling relations (Lee & Grand, 1996). P wave velocity models also resolve similar structures, but with only 4% total variation. A total variance reduction of 40%, however, implies that significant small-scale heterogeneity is yet unresolved in this region (Lerner-Lam et al., 1998).

Receiver function studies and gravity modeling by Sheehan et al. (1995) require thick crust beneath the westernmost Great Plains and the Colorado Rockies. The results are inconsistent with an Airy-type root beneath the SRM, and the favored model includes a strong mantle component to compensation of high elevations. The topography on the 410 and 660 discontinuities reflects a slab extending through the transition zone (Dueker & Sheehan, 1998), consistent with low velocities observed in North America S wave tomography by Van der Lee & Nolet (1997). Null shear wave splitting measurements observed beneath the highest elevations in Colorado were interpreted as either convergent or divergent small-scale asthenospheric flow (Savage et al., 1996). Due to the spatial coincidence of high mantle-supported topography, low body wave speeds, and large negative Bouguer anomalies, and a lithosphere too thin to generate significant splitting,

these results are most consistent with passive asthenospheric upwelling beneath the SRM, and not due to a strong fabric in the lithosphere (Savage et al., 1996).

The Continental Dynamics of the Rocky Mountains (CD-ROM) program was a multi-institutional collaborative study of the crust and mantle beneath the southern Rocky Mountain region. Data from both controlled source and passive source seismic studies were used to produce images of discontinuity and velocity structure to approximately 150-250 km. A dense controlled source seismic line was deployed N-S from northern New Mexico, across central Colorado, and into southern Wyoming. Two passive seismic lines were focused on two boundaries of lithospheric assembly: the Cheyenne Belt at the southern margin of the Archean Wyoming Craton, and the Jemez lineament at the zone where the 1.73 Ga Yavapai province meets the 1.67 Ga Mazatzal province (Karlstrom & Bowring, 1988). Results from these data reflect a complex history of Proterozoic lithosphere assembly and subsequent modification in the Phanerozoic.

Refraction and reflection results indicate 5-10 km of relief on the Moho near the Colorado Mineral belt (Levander et al., 2005; Snelson et al., 2005), and 15 km total relief in southern Rocky Mountians region (Keller et al., 2005). A widespread high velocity lower crustal layer 5-10 km thick was seen as evidence for extensive mafic underplating in the Proterozoic, with possible localized magmatic addition during the subsequent Laramide, mid-Teriary ignumbrite flare-up, and Rio Grande Rift events (Snelson et al., 2005; Keller et al., 2005). Low crustal and uppermost mantle velocities beneath the Colorado Mineral belt may be a manifestation of local magmatic addition via a preferred pathway in the lithosphere (Levander et al., 2005). The Colorado Mineral belt is associated with 45-50 km thick crust, and relatively thicker lower crust, interpreted as addition

by mafic underplating subsequent to continental assembly (Levander et al., 2005). Gilbert & Sheehan (2004) employed receiver functions using data from CD-ROM, the earlier Rocky Mountain Front experiment, and several other regional and local arrays, to map crustal thickness. Their results support the conclusions derived from crustal studies, that the crust in the southern Rocky Mountains region has widely varying thickness and does not appear to correlate with topography, indicating that the high elevations of the Colorado Rocky Mountains are not compensated by a simple Airy crustal model.

Body wave and surface wave tomography from the CD-ROM experiment focused on suspected lithospheric suture zones (the Jemez lineament and the Cheyenne belt), and was poorly resolved in central Colorado. Data from the earlier Rocky Mountain Front experiment, however, were used to supplement CD-ROM data to provide new support for the hypothesis that inherited lithospheric structure has influenced recent modification in the southern Rocky Mountains region (Karlstrom et al., 2005). Investigators identified dipping velocity domains that project onto crustal manifestations of Proterozoic suture zones.

2.2 Data and Methods

2.2.1 Stations and sources

Stations used in this study are primarily from two networks: the USArray Transportable Array (TA) and the CREST network, with additional stations from three other networks. The TA facility was fully deployed in Colorado in 2008 and 2009, and provided 101 broadband stations in the study area with approximately uniform 70 km spacing. These stations reported continuous data in near real-time at 40 samples per second. Three stations are part of the Intermountain

West Broadband Seismic network (IW), three are part of the United States National Seismic Network (US), and one is part of the University of Utah Regional Network (UU). These four networks are subsequently referred to by the virtual network, US-ALL (Figure 2.2). CREST stations were embedded within the footprint of existing networks, including the TA. Combined minimum station station is 18 km, and the mean spacing within the CREST footprint is 23 km. The aperture of the combined network is $\sim$ 300 km.

The CREST network itself consisted of 59 broadband stations, of which 55 were Guralp CMG-3T sensors and 4 were CMG-ESP sensors. This standalone temporary deployment was supported by the Incorporated Research Institutions for Seismology-Program for Array Seismic Studies of the Continental Lithosphere (IRIS-PASSCAL). The stations were embedded inside the US-ALL network, and recorded continuously from July 2008 to October 2009 (14 months). Stations were deployed on private lands throughout the high elevations of western Colorado, and were powered by a combination of battery packs and solar panels. Sensors were placed on a concrete pad two feet below the surface, the vaults were filled sand and were buried with soil to a height of 1 foot above grade to minimize both high frequency acoustic noise and long period thermal noise. Data at each station were digitized using a Reftek RT-130 DAS onto two 2GB flash disks at 40 samples per second. Regular station visits every 2-4 months were performed to refresh memory and maintain station equipment. Data from the CREST network were processed into SEED format and submitted to the IRIS Data Management Center. We find data quality from this station construction to be comparable to that of the TA.

We inspect teleseismic direct P and S arrivals from earthquakes occurring between April 1, 2008 and October 14, 2009, beginning from the time that USAr-

ray had sufficient coverage in Colorado to the time that CREST stations were removed. Candidate P events were restricted to those with epicentral distances (Δ) of $25^\circ \leq \Delta \leq 85^\circ$ and magnitude ≥ 5.3, as determined by the Weekly Hypocenter Data File (WHDF) catalog from the National Earthquake Information Service (NEIS). While we recognize that signal-to-noise ratio (SNR) for earthquakes as small as magnitude 5.3 is generally low, SNR thresholding was done at a later part of the data processing and we wished to retain as many useful events as possible.

In order to avoid the superposition of direct arrivals with surface or core reflected phases, additional constraints were imposed such that events with $25^\circ \leq \Delta < 30^\circ$ must be deeper than 30 km, events with $30^\circ \leq \Delta < 35^\circ$ must be deeper than 20 km, and events with $35^\circ \leq \Delta$ must be deeper than 10 km. Of 348 candidate P events, 235 were recorded with a SNR greater than 2, and 183 produced travel time residuals with estimated to be ≤ 0.15 seconds (Figure 2.3). S events were restricted to those with epicentral distances of $25^\circ \leq \Delta \leq 90^\circ$ and magnitude ≥ 5.3, with depth restrictions matching those for P events. Of 337 candidate S sources, 104 were recorded with a signal-to-noise ratio (SNR) greater than 2, and 93 produced travel time residuals with estimated standard deviations to be ≤ 0.3 seconds (Figure 2.4).

The distribution of both P and S sources is dominantly from Pacific rim subduction beneath the Pacific Northwest, the Aleutian Islands, Kamchatka, and Japan, and from the southwest beneath South America. A large number of sources also originate from Tonga-Fiji subjection in the southwest, and a small number of shallow, low magnitude events originate along oceanic-oceanic plate boundaries. The subduction-related sources from the northwest and southeast, and to

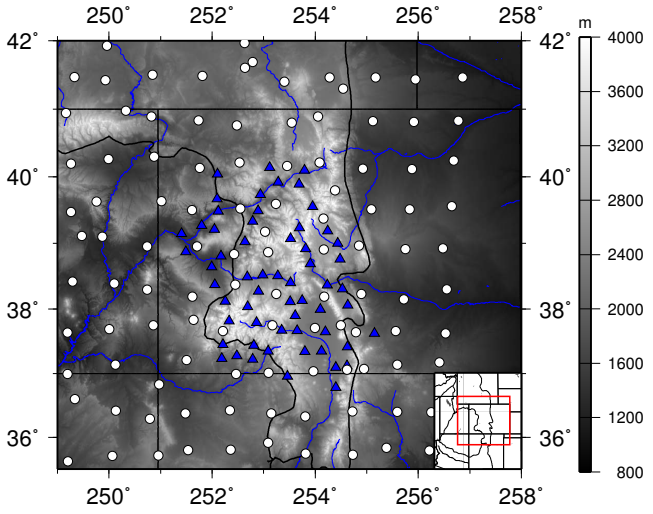

Figure 2.2: Location of CREST stations (blue triangles) and US-ALL stations (white circles). Physiographic provinces are outlined. Inset: the study area is outlined in red.

a smaller degree the southwest, provide a wide range of origin magnitudes and depths. This increases the number and spatial distribution of crossing rays within the image volume, and results in higher model resolution along those source back azimuths in the resulting models (Section 2.2.7).

2.2.2 Travel time residual measurement

Fine-grained data selection and automatic windowed downloading of US-ALL data were done using the Standing Order for Data software (SOD) (Owens et al., 2004). Data from all networks were then combined into a single css3.0 database and were processed in Matlab using the Antelope Toolbox for Matlab. For P residual measurement, vertical component seismograms were bandpass

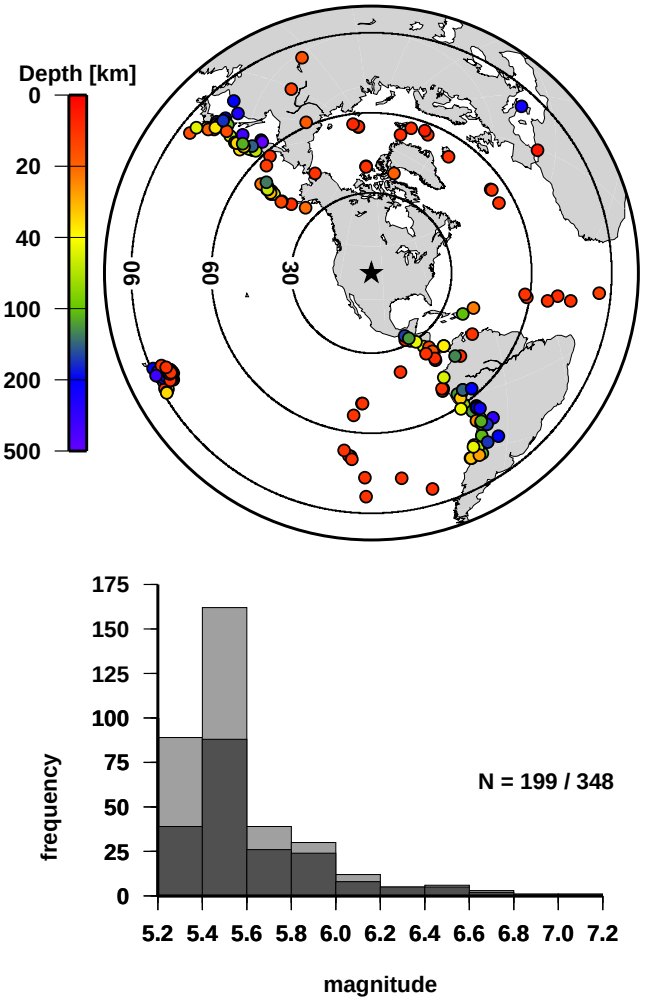

Figure 2.3: a) Source distribution for teleseismic events used in P travel time tomography, events colored by depth. b) Magnitude histogram of inspected (light) and used (dark) events.

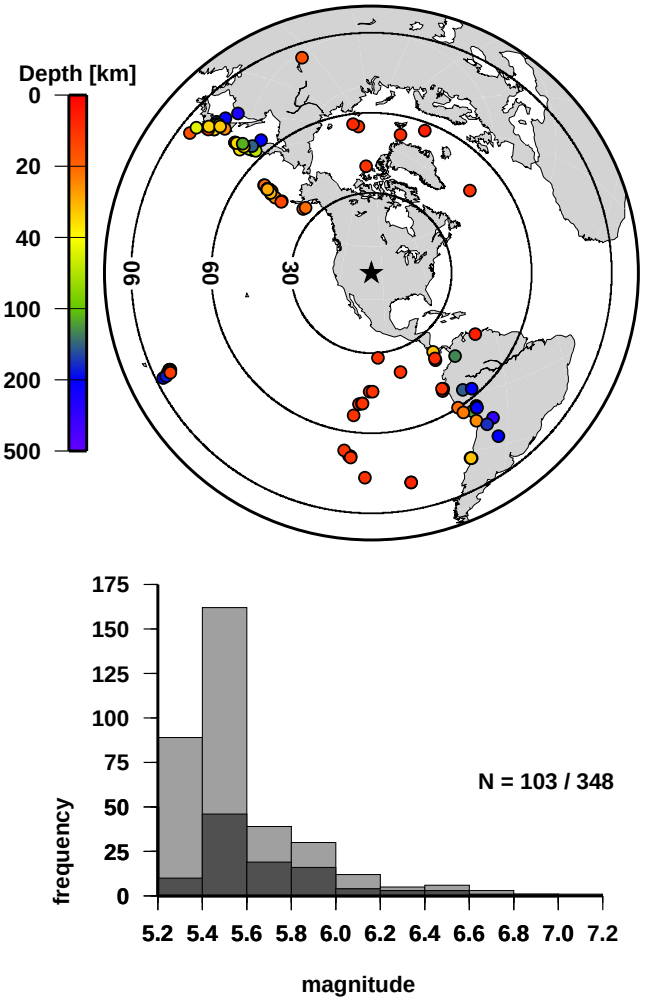

Figure 2.4: a) Source distribution for teleseismic events used in S travel time tomography, events colored by depth. b) Magnitude histogram of inspected (light) and used (dark) events.

filtered between 0.25 Hz and 8 Hz in order to avoid possibly coherent microseism expected at 0.1-0.3 Hz, and higher frequency local noise that may interfere with the cross correlation (Wilson et al., 2002). S wave residual measurements were made on transverse component waveforms that were filtered between 0.015 Hz and 0.5 Hz.

We apply the cross correlation optimized method of Vandecar & Crosson (1990) for semi-automated measurement of mean-removed travel time residuals and estimation data standard errors. Predicted arrival times from the ak135 reference model were used to guide cross correlation window selection for travel time residual measurement. Waveforms were formed into event gathers and were decimated to 40 samples per second. Because the residual measurement method produces mean-removed residuals for each event gather, it is important that each gather samples a large part of the the image volume, so that gather means are approximately equal. We therefore rejected gathers fewer than 10 used arrivals, or those that are spatially limited across the network. Waveforms were then aligned on predicted P or S arrival times and truncated to 30 seconds before and after the arrival. Waveforms for P arrivals were automatically rejected if the maximum of the signal envelope in the 60 second window was less than twice the mean of the signal envelope. For S arrivals, for which the microseismic noise spectrum overlaps with the signal spectrum, this ratio threshold was set at 4. Cross correlation windows for aligned waveforms were manually selected such that 1-2 cycles of the arrival pulse were included. For P arrivals, this window was 2-5 seconds long, depending on the dominant frequency of the arrival. For S arrivals, this window was appropriately larger, due to the lower frequency content of S waves.

Cross correlation produces a length $n(n-1)/2$ vector of waveform pair time shifts, where n is the number of waveforms in the gather. We add an addi-

tional constraint equation that sets the mean time shift equal to zero, and solve an overdetermined set of linear equations for a vector of n individual station time shifts (residuals) relative to a gather mean of zero (Allen et al., 2002; Yuan & Dueker, 2005). Iterative outlier removal was also performed for each gather, whereby residuals larger than normal 2σ for the gather were removed and the cross correlation measurement was performed again until an approximate normal distribution was achieved (Yuan & Dueker, 2005). Almost 25,000 P residuals and almost 11,000 S residuals were measured that met the quality criteria outlined above. From these data, we selected residuals with estimated standard errors no larger than 0.15 seconds for P arrivals and 0.3 seconds for S arrivals. This dataset consists of 19,602 P residuals and 9,794 S residuals, with a root-mean-square (RMS) of 0.37 sec and and 1.01 sec, respectively (Figures 2.5a and 2.6a).

The cross correlation method also produces an estimate of data standard deviations, which were later used to scale data equations in the linear tomographic inversion (Section 2.2.5). The range and mean of standard errors for the P dataset were 0.007–0.15 sec and 0.03 sec, respectively, and those for the S dataset were 0.01–0.3 sec and 0.10 sec (Figures 2.5b, 2.6b). Though these errors are consistent with similar values in the SRM region (Yuan & Dueker, 2005), it has been noted that manually assigned pick errors for broadband teleseismic body wave residuals in the region are up to an order of magnitude larger than those assigned by the cross correlation method, and that the smallest standard deviations may too optimistic (Waite et al., 2006; Pavlis & Vernon, 2010). The stability of residuals and their standard deviations were investigated for a random subset of 20 P events with a variety of source depths, magnitudes, and frequency content. Semiautomated measurement was repeated using both the original passband and more narrow bands of 0.25–1 Hz and 0.25–4 Hz. It was found that

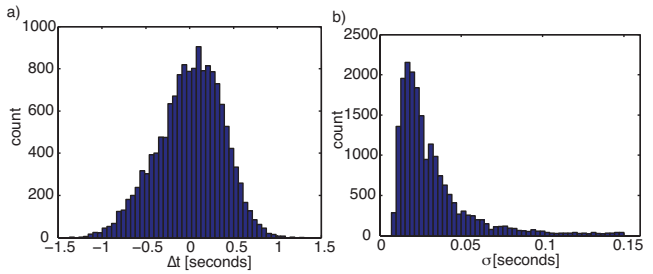

Figure 2.5: Histograms of measured P travel time residuals (a) and estimated standard deviations (b) from the cross correlation method.

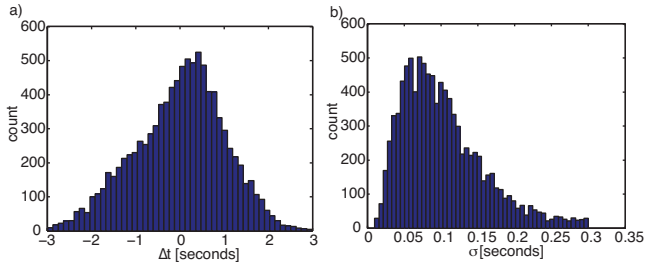

Figure 2.6: Histograms of measured S travel time residuals (a) and estimated standard deviations (b) from the cross correlation method.

residual measurements did not change appreciably, but standard deviations fluctuated by as much as an order of magnitude, depending on the manually chosen correlation window. In order to maintain consistency with manually assigned picks, we scaled the crosscorrelation–determined error estimates by a factor of 4. The P and S velocity models presented hereafter are those using the modified standard errors.

2.2.3 Crustal Correction

As seismic velocities in the crust beneath the Colorado Rocky Mountains vary at length scales below the resolution of most teleseismic experiments, it is

necessary to correct data for travel time variations owing to topography, crustal thickness, and crustal velocity. Realistic variations in crustal properties can produce crustal travel time corrections on the order of the data themselves, so failure to properly account for crustal contributions to travel time can lead to decreased resolution and mantle velocity artifacts (Waldhauser et al., 2002).

Several different approaches have been proposed to account for crustal heterogeneity in mantle tomography. First, if station spacing is sufficiently small, crustal velocity can be resolved in the inversion (Yuan & Dueker, 2005). A second approach involves including "station terms" in the inversion (Dziewonski & Anderson, 1983; Zhou & Wang, 1994). These are free parameters in the inversion that account for travel time anomalies unresolved in the mantle. If stations are sufficiently far apart, one runs the risk of incorrectly absorbing mantle velocity heterogeneity into the station term, and care must be taken to damp these parameters. If an *a priori* crustal velocity model is known, another approach is to generate crustal travel times from each source-station pair by raytracing through the crust, and subtracting those values from the data (Allen et al., 2002; Waldhauser et al., 2002). A final approach is a hybrid between the previous two, whereby one inverts for crustal parameters but penalizes deviations from an *a priori* crustal model (Li et al., 2008a; Xue & Allen, 2010).

The mean station spacing of the CREST+US-ALL network is over 20 km, too large to resolve lateral crustal velocity changes directly and large enough to possibly absorb mantle heterogeneity, therefore crustal corrections are calculated using an *a priori* crustal model. The crustal thickness model consists of high resolution crustal thickness variations from 96 stations within the CREST footprint [Hansen and Dueker, in prep], and 71 stations reprocessed from the EarthScope

Automated Receiver Function Survey (EARS) (Crotwell & Owens, 2005) [Lowry and Perez-Gussinye, in prep]. The composite crustal thickness model was then smoothed using a 30 km mean filter to minimize the effect of spurious crustal thicknesses derived from single-station estimates. A one dimensional crustal P_g model derived from USArray data was used to account for bulk lateral crustal P velocity variations (Steck et al., 2009). A constant V_p/V_s ratio of 1.75 was used to estimate crustal V_s. Uppermost mantle velocities were interpolated from CRUST2.0, a global $2^\circ \times 2^\circ$ crustal model (Bassin et al., 2000). Teleseismic rays were traced through ak135 to the ellipsoid below a station, then assumed vertical through topography (Figure 2.7).

Crustal travel times for each gather were calculated relative to the ak135 crustal thickness of 35 km at sea level, then demeaned and subtracted from the zero mean travel time residuals. The range of crustal corrections for the P dataset was -0.43–0.60 sec, with an RMS of 0.18 sec. For the S dataset, the range and RMS was -0.76–1.02 sec and 0.31 sec. Correcting P travel time residuals increased their RMS from 0.37 sec to 0.40 sec. S travel time residual RMS was also increased after correction, from 0.95 sec to 0.99 sec. While the P and S crustal corrections are slightly larger than that observed for the greater western US (Schmandt & Humphreys, 2010), this is likely due in part to strong lateral gradients in thermal and chemical properties of the crust relating to the transition to from modified to cratonic lithosphere beneath the network. That the travel time RMS increased after correction is an indication that integrated crustal and mantle travel time variations are not everywhere spatially correlated.

It is notable that the largest crustal corrections are generally at the edge of or outside of the CREST network footprint (Figures 2.8). Crustal thickness within

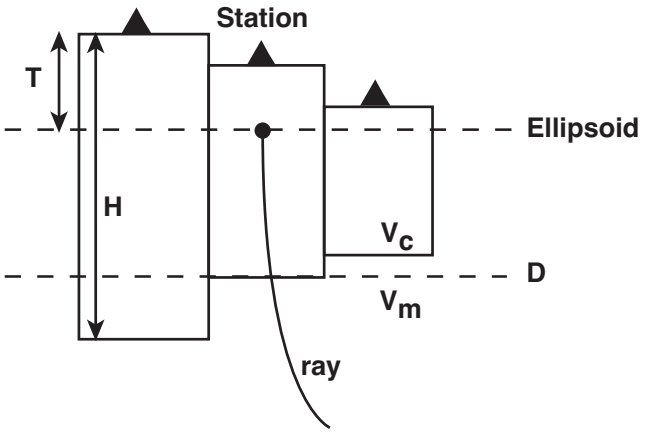

Figure 2.7: Crustal correction schematic. Incoming teleseismic ray is traced through the 1D reference model to the ellipsoid and assumed vertical through topography. T represents topography, H is crustal thickness, D is the crustal correction depth of 35 km, and Vc and Vm are crustal and mantle velocities, respectively.

the CREST footprint is well constrained by multiple stations [Hansen and Dueker, in prep.], while thickness outside the footprint is generally constrained by single-station receiver function studies [Lowry and Perez-Gussinye, in prep]. The process of combining two crustal thickness models with different lateral and depth resolutions may produce artifacts, likely to appear at the stitching boundary between the models. While the composite crustal model used here was smoothed in order to reduce such artifacts, large inaccuracies in the crustal model will persist and manifest themselves as correlated errors in the travel time data. As described later, velocity inversions are heavily regularized in order to minimize the influence of these inaccuracies.

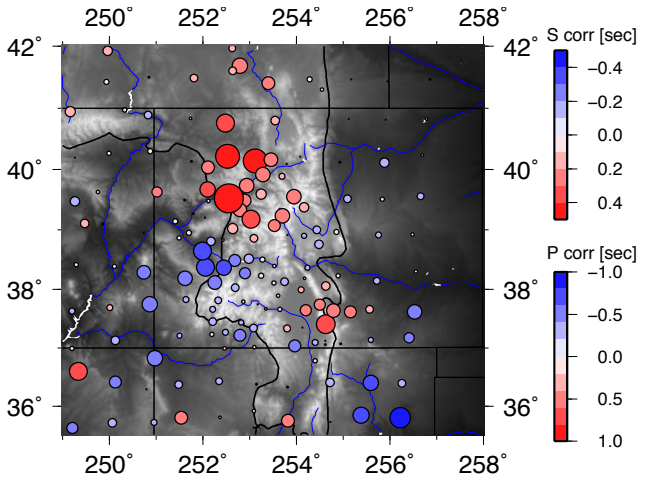

Figure 2.8: P and S crustal travel time variations for a gather recorded on all stations, scaled according to magnitude and colored according to polarity. Red represents seismically "slow" crust, and blue represents "fast" crust. Crustal corrections represent travel time differences owing to crustal thickness, crustal velocity, and topography variations across the network, and are subtracted from measured residuals.

2.2.4 Travel Time Residual Patterns

Travel time residuals are a result of path integrated variations in velocity. The spatial distribution of crust corrected travel time residuals indicate the approximate location of high and low velocity domains in the image volume. Figures 2.9 and 2.10 show crust corrected residuals used in the inversion. Data are plotted at each station, colored by polarity, and scaled by magnitude. Residuals at each station are depicted on a polar plot by back azimuth and incidence angle at 200 km depth. Broadly, the most negative residuals were recorded in southern Wyoming and the Great Plains of eastern Colorado, and most positive residuals were recorded beneath the high elevations of western Colorado and south near the Jemez Lineament and northern Rio Grande Rift. In these regions, residuals from many back azimuths and incidence angles indicate either strong anomalies near the stations or less pronounced anomalies distributed more broadly along

ray paths to these stations. Stations in westernmost Colorado and on the northern Colorado Plateau exhibit a more complicated residual pattern, with positive and negative arrivals grouped by back azimuth, indicating the presence of a complex boundary between anomalously slow and fast regions in the mantle.

The RMS of corrected P residuals is 0.40 seconds, with a range of -1.29–1.44 seconds. The latest P arrivals (residual $>$ 1 second) were recorded at stations T22A and S19 within the San Juan Mountains and U22A in the San Juan Basin of New Mexico. Modest late arrivals from southern back azimuths were also recorded at stations behind the Front Range near Denver and Boulder. The earliest P arrivals (residual $<$ 1 second) were recorded at stations R26A and S26A on the Great Plains of eastern Colorado. Corrected S residuals range from -3.50–3.27 seconds, with an RMS of 0.99. Residuals $>$ 2.5 seconds were recorded within the San Juan and Sawatch Mountains, and residuals $<$ -3 seconds were recorded near the Cheyenne Belt of southern Wyoming, where fast lithospheric velocities have been previously imaged (Yuan & Dueker, 2005). We note that numerous large magnitude P and S residuals were recorded at stations on the edge of the network, such as in southern Wyoming, the Four Corners region and the Rio Grande Rift. These stations, however, serve mainly to increase the model depth resolution beneath the Colorado Rockies in the resulting velocity models, and residuals at these stations are not fully explored here.

2.2.5 Geometric Ray Tracing

The image volume beneath the Colorado Rockies was parameterized by constant slowness blocks $0.25^\circ \times 0.25^\circ$ laterally, and 25 km in depth. The full

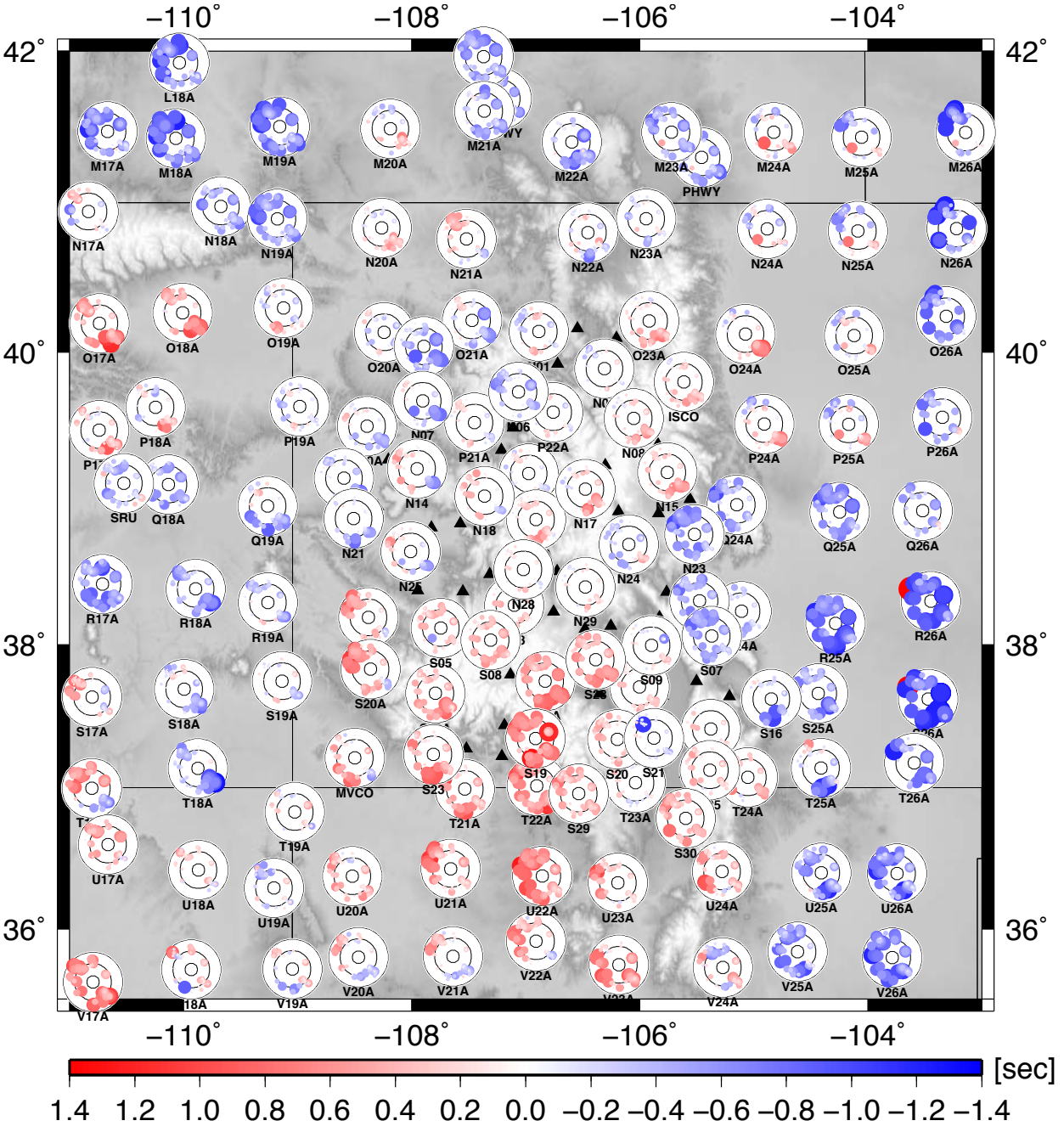

Figure 2.9: P residuals at selected stations, scaled by magnitude and colored by polarity. Residuals at each station are plotted on a stereographic polar projection by back azimuth and piercing angle at 200 km. Piercing angle contours are 10°, 30°, and 50°, from inner to outter. In order to aid visualization, residuals for select stations are not plotted (black triangles).

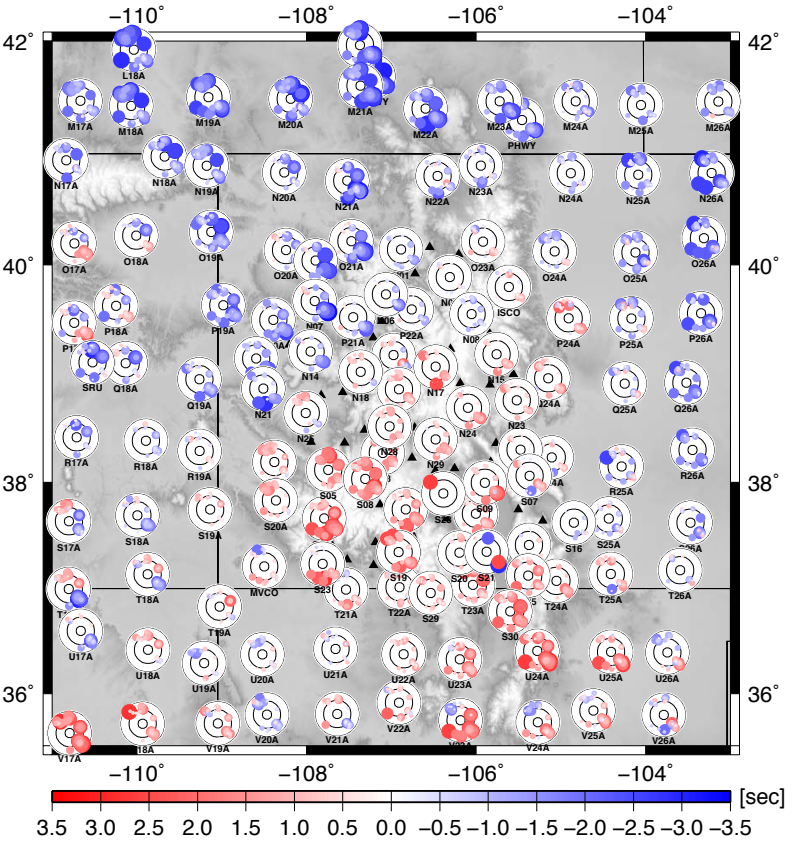

Figure 2.10: S residuals at each station, scaled by magnitude and colored by polarity. Residuals at each station are plotted on a stereographic polar projection by back azimuth and piercing angle at 200 km.

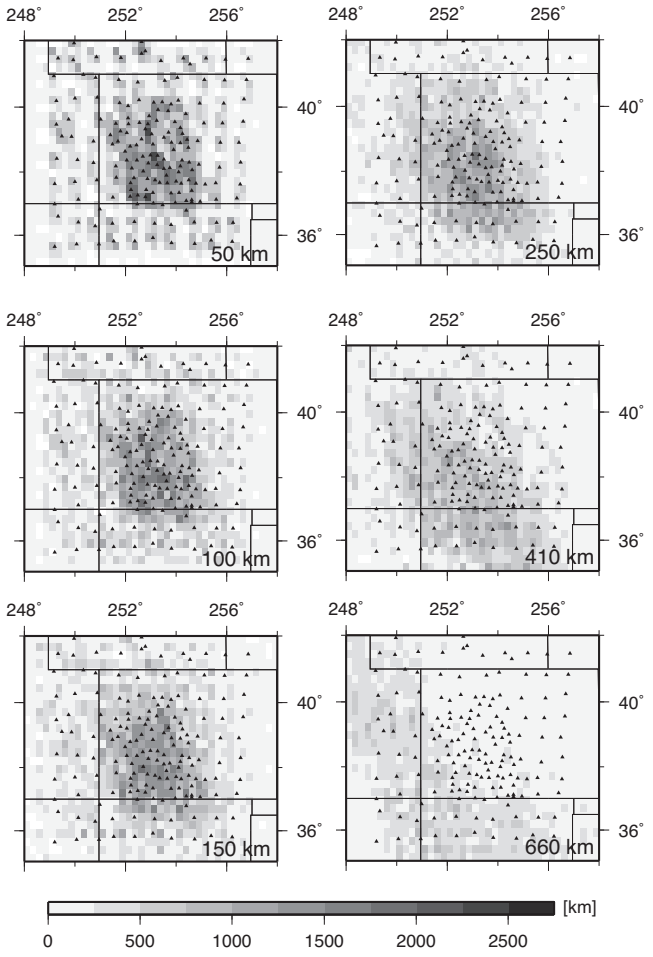

Figure 2.11: Depth slices of total P ray length through parameters in the image volume. Slice depths are in the lower right of each tile.

model dimensions span longitudes -118 to -96 and latitudes 29.25 to 48.25, and from the surface to 1000 km depth. The resulting model vector consists of 267,520 block-centered slowness parameters. A large image volume was intentionally chosen so that velocity anomalies would not be constrained to an inappropriately small region, and to facilitate later edge-damping "squeeze" tests of appropriate model size.

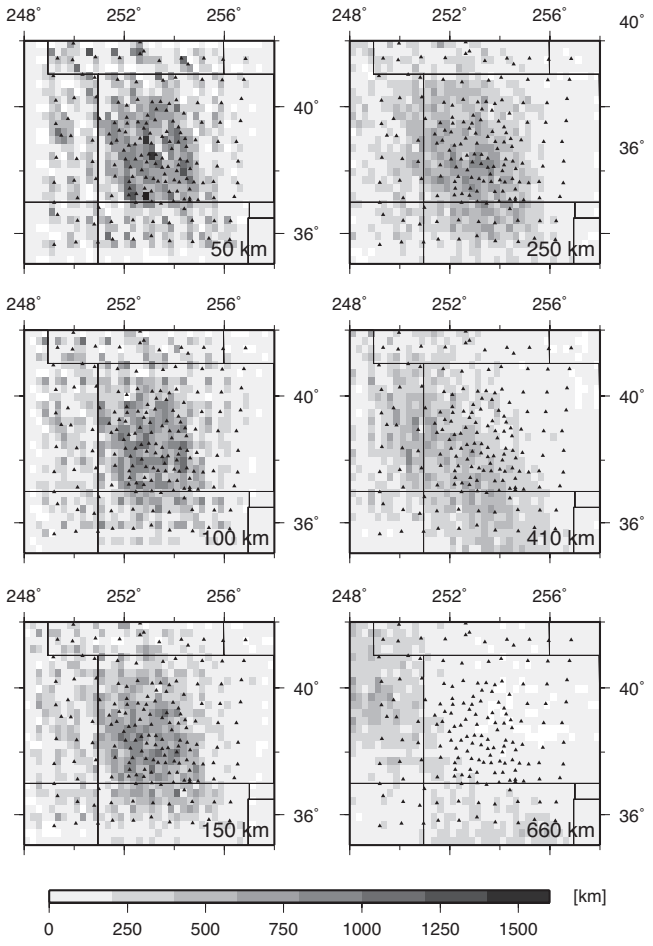

Figure 2.12: Depth slices of total S ray length through parameters in the image volume.

Teleseismic rays were traced through the 1D reference model ak135 to the ellipsoid beneath each station using geometrical ray tracing. Depth sampling of the ray was increased by a factor of 20 relative to the model depth discretization during the tracing process in order to more accurately represent ray curvature. Ray density through the image volume may be used as a qualitative proxy for the spatial resolving power of a data set (Zhang & Thurber, 2007). Model parameters traversed by many rays from many azimuths are generally more well resolved. Regions of highest ray density are directly beneath stations, as arriving rays are converging the receiver (Figures 2.11 and 2.12). These shallow regions, however, have poor resolution between stations, and poor vertical resolution because incoming rays are nearly vertical and parallel. Because of this, the upper 50 km of the image volume have been heavily damped during inversion. Anomalies within the crust were removed during crustal correction, so none should be present in the inverted models. The cone-shaped region of highest ray crossing in both P and S models extends beneath the CREST footprint to depths of 400 km, but then migrates southwest beneath the Four Corners region and bifurcates. This is a result of the uneven distribution of sources to the north, west, and south of the network.

The use of geometrical ray tracing to represent inherently band-limited data results in underestimated velocity heterogeneity because of wavefront healing and insensitivity to the first Fresnel volume (Montelli et al., 2004; Song & Helmberger, 2007). This effect is less pronounced for relatively small aperture networks versus global studies, as the Fresnel volume collapses towards the geometrical ray at shallow depths, and the amount of healing possible across a small image volume is low. Regardless, these effects must be taken into consideration.

The dominant period of teleseismic P and S wave energy measured was ∼3 seconds and ∼10 seconds, respectively. These correspond to wavelengths of ∼30 km and 50 km for mean transition zone velocities. The Fresnel volume diameter can be calculated by

$$q(x) = 2\sqrt{\frac{\lambda x(L-x)}{L}}, \tag{2.1}$$

where x is distance from the source, L is the total ray length, λ is the wavelength (Spetzler & Snieder, 2004). For a ray length of 10,000 km, the Fresnel volume diameter at ∼350 km depth is approximately 175 km for P and 275 km for S. At ∼175 km depth, the Fresnel diameter is 125 km and 200 km wide. Anomalies smaller than the width of the first Fresnel zone will be poorly imaged without accounting for finite frequency effects in the inversion.

Additionally low velocity zones deep in the image volume will tend to be underestimated due to the effects of wavefront healing, where the least time path deviates from the geometric ray at large distances from the anomaly. For a teleseismic arrival with ∼30 km wavelength, it is estimated that delayed arrivals generated from a 200 km wide anomaly at the bottom of the upper mantle will remain largely unhealed (Nolet & Dahlen, 2000; Waite et al., 2006). For longer wavelength S arrivals, the effects of healing are more severe at similar depths.

The combined effects of limited aperture, finite frequency considerations, and wavefront healing make resolving velocity anomalies less than ∼200–300 km wide at the base of the upper mantle difficult using teleseismic tomography and geometric ray theory. The pattern of large residuals in western Colorado, however, suggests that slow anomalies are broad and deep, and/or narrow and shallow. Either of these cases would be well resolved by the CREST dataset.

2.2.6 Inversion Method

We use the iterative linear least squares inversion method LSQR (PAIGE & SAUNDERS, 1982) to produce independent regularized models of isotropic ΔV_p and ΔV_s. We minimize the following composite objective function:

$$\varepsilon = ||\mathbf{Gm} - \mathbf{d}||^2 + \alpha_L ||\mathbf{L_2 m}||^2 + \alpha_m ||\mathbf{m}||^2 + \alpha_D ||\mathbf{Dm}||^2 \ . \tag{2.2}$$

The first term represents data misfit; $\mathbf{G}$ is the $m \times n$ data kernel matrix, $\mathbf{m}$ is $n \times 1$ the model slowness vector, and $\mathbf{d}$ is the $m \times 1$ crust corrected data vector. Rows of $\mathbf{G}$ and corresponding entries in $\mathbf{d}$ are divided by each datum's estimated standard error. The other three terms represent model smoothing, norm damping, and edge damping, respectively, weighted by corresponding regularization weighting parameters, $\alpha_{L,m,D}$. $\mathbf{L_2}$ is a second–difference (Laplacian) roughening matrix, and $\mathbf{D}$ is a matrix that damps one layer on the top of the model and three layers on the sides and bottom. The choice of α_L and α_m was made through the use of trade–off curves and the discrepancy principle (Hansen & O'Leary, 1993). A suite of damping and smoothing regularization parameters were investigated, implemented as fractions of the corrected and scaled data vector norm $R_0 = ||\mathbf{d}|| = ||(\mathbf{\Delta t} - \mathbf{\Delta t_{crust}})/\mathbf{s_e})||$, where $\mathbf{s_e}$ is the standard error vector. Inversions were performed using all combinations of α_L and α_m, and variance reduction surfaces and l–curves were plotted. Edge damping was kept constant at $500R_0$. For the P data vector, R_0 is equal to 664, and equal to 340 for the S data vector. Figures 2.13a and 2.14a show a contoured variance reduction surface over the regularization parameter domain for the P and S inversions. Here, variance reduction is

$$\Delta Var = 1 - \frac{||\mathbf{Gm} - \mathbf{d}||}{||\mathbf{d}||}. \tag{2.3}$$

The discrepancy principle simply states that a model should not try to fit noise in the data, when the level of noise is known. If the data equations in (2.2) are scaled by appropriate data errors, then the noise level of the data is approximately equal to $\sqrt{m}$ (Aster et al., 2005). For the P dataset, this corresponds to a ΔVar of 81.8%, and 82.8% for S. The discrepancy principle ΔVar contour is shown in Figures 2.13 and 2.14 as a dashed line. Models along these contours fit the data to the level of the noise equally well, despite varying levels of smoothing and damping. The models we present here are conservative, in that smoothing and/or damping are generally larger than that prescribed by the discrepancy principle. This is common in geophysical inversions where data are inconsistent and noisy (Parker, 1972).

A joint inversion of V_p and V_s was also performed, following the method of Schmandt & Humphreys (2010), in which the individual P and S cost functions were combined with an additional V_p/V_s smoothness constraint:

$$\varepsilon_{V_p/V_s} = \varepsilon_{Vp} + c\varepsilon_{Vs} + \alpha_{Vp/Vs} \left|\left| \mathbf{L_{1,V_p/V_s}} \mathbf{m_{p,s}} \right|\right|^2 \tag{2.4}$$

The first two terms of the joint cost function (2.4) are the individual cost functions for the V_p and V_s inversions. The V_s term is scaled by a factor, $c = \left|\left|\mathbf{d_p}\right|\right| / ||\mathbf{d_s}||$, used to equalize the influence of P and S data. For these data, $c = 1.64$. The third term is a smoothness constraint that penalizes the gradient of the V_p/V_s ratio, but does not penalize deviations from background (ak135) V_p/V_s. $\mathbf{L_{1,V_p/V_s}}$ is the V_p/V_s gradient operator and $\mathbf{m_{p,s}}$ is the $(n_p + n_s) \times 1$ composite model slowness vector. The gradient operator is constructed, following Hammond &

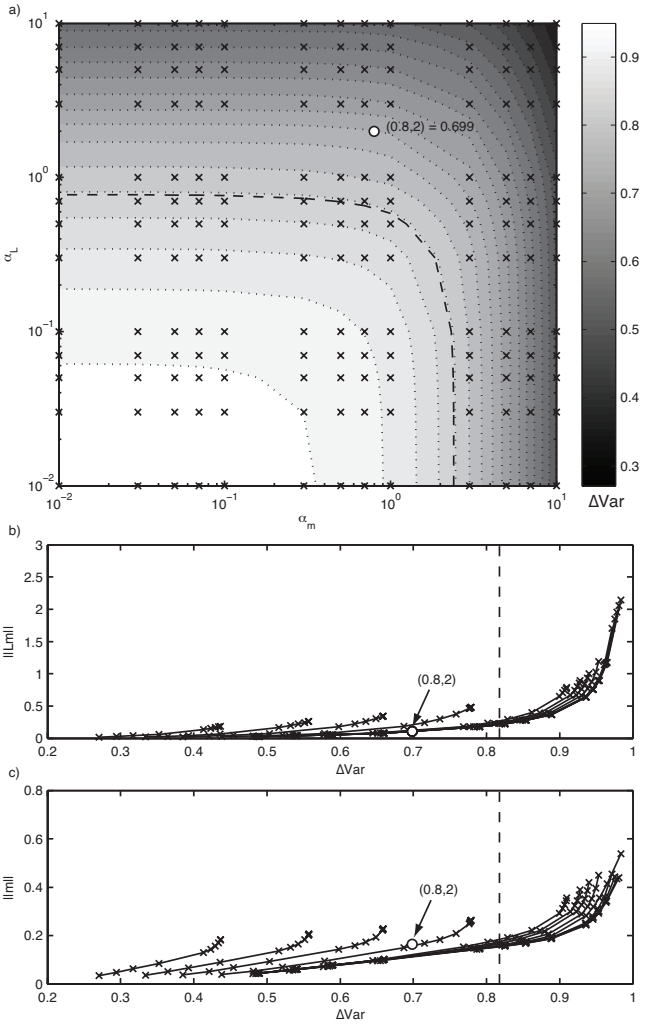

Figure 2.13: a) Contoured P data set variance reduction (ΔVar) surface over the damping parameter (α_m) and smoothing parameter (α_L) domain. Points represent tested regularization parameters (control points). Dashed line is the variance reduction prescribed by the discrepancy principle of 81.8%. The preferred parameter combination is the labeled white circle, corresponding to a ΔVar of 70.1%. b) Trade–off curve between ΔVar and model roughness. α_L varies along each curve, and α_m varies between curves. As above, tested parameters (crosses), preferred combination (white circle), and discrepancy principle value (dashed) are labeled. c) Trade–off curve between ΔVar and model length. α_m varies along each curve, and α_L varies between curves.

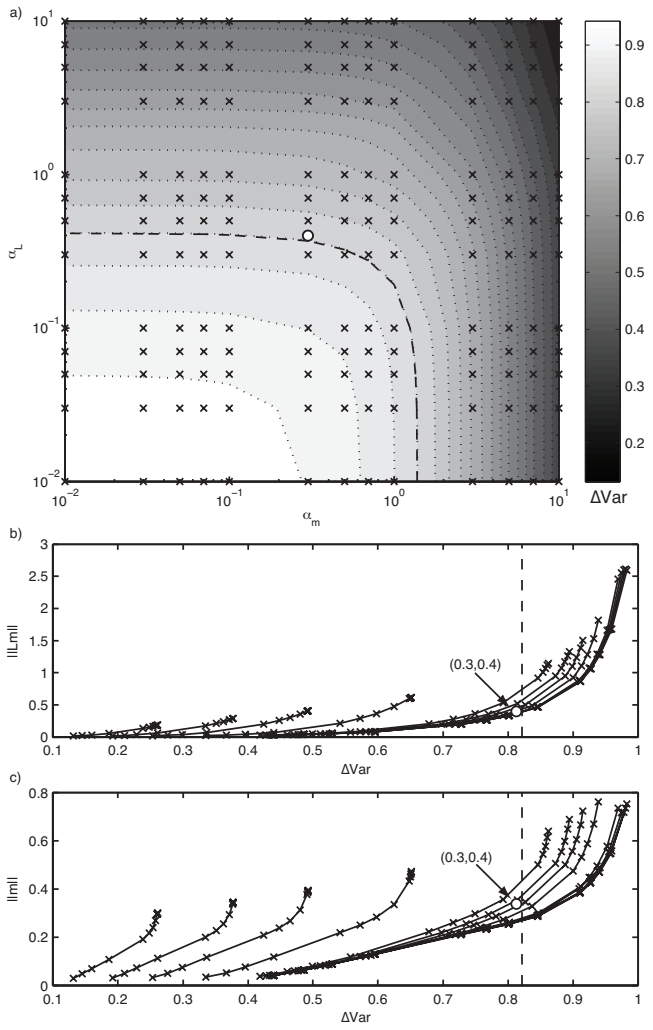

Figure 2.14: a) Contoured variance reduction (ΔVar) surface over the damping parameter (α_m) and smoothing parameter (α_L) domain for the S data set . Tested regularization parameters (control points) are crosses. Dashed line is the variance reduction prescribed by the discrepancy principle (82.2%). The preferred parameter combination is the labeled white circle, corresponding to a ΔVar of 81.3%. b) Trade–off curve between ΔVar and model roughness. As above, preferred parameters and discrepancy principle are labeled. c) Trade–off curve between ΔVar and model length.

Toomey (2003), by penalizing the spatial derivative of V_p/V_s, or equivalently, the derivative of the slowness ratio, S_s/S_p:

$$\Delta\left(\frac{S_s}{S_p}\right) = \frac{S_p\Delta S_s - S_s\Delta S_p}{S_p^2}\,. \tag{2.5}$$

One can calculate this ratio by multiplying the composite slowness vector $\mathbf{m_{p,s}}$ times a scaled composite gradient operator:

$$\mathbf{L_{1,V_p/V_s}} = [-\mathbf{L_1W_p}, \mathbf{L_1W_s}]\,, \tag{2.6}$$

where $\mathbf{L_1}$ is a three dimensional gradient operator, $\mathbf{W_p}$ is an $n \times n$ diagonal matrix whose diagonal elements contain the appropriate reference model slowness ratio S_s/S_p^2, and $\mathbf{W_s}$ is a similar matrix whose diagonal elements contain the ratio $1/S_p$, or just the reference P velocity. $\mathbf{L_1}$ was constructed using a seven–point central difference kernel.

A range of α_{V_p/V_s} were investigated, also implemented as fractions of the scaled and crust corrected P data norm, R_0, from 0 (unconstrained) to $10R_0$. Smoothing and damping parameters for V_p and V_s were kept constant at their preferred values. At $\alpha_{V_p/V_s} = 0$, the resulting V_p/V_s model is essentially the ratio of the individual V_p and V_s models, and ranged from almost -2.6 to 2.4% from the background model. The maximum weighting resulted in a V_p/V_s range of -0.4% to 0.6%, and decreased the V_p and V_s model variance reductions to 65% and 64%, respectively. The preferred weighting corresponded to $\alpha_{V_p/V_s} = 0.4R_0$, had minimal impact on the V_p and V_s model variance reductions (2%–4% decrease) and produced variations of -1.4% to 1.9%, consistent with those seen in western US scale images (Schmandt & Humphreys, 2010).

2.2.7 Resolution Tests

The resolving power of the experiment is determined by the source-station geometry, and the parameterization and regularization of the inversion. We perform "checkerboard" tests to qualitatively investigate the ability of the inversion to recover features ∼75 km in dimension across the model space. Alternating 3^3 block clusters of ±2% perturbation were used to generate synthetic travel time data using the identical source-station geometry in the P and S velocity inversions. In order to simulate noise, normally distributed random noise with zero mean and the same standard deviation as the estimated data standard errors was added to the synthetic data. Data equations were scaled by the standard errors used in the final P and S inversions. The synthetic data were then inverted using the same smoothing and damping used to produce the final models. Spatial variations in recovery of the input checkerboard pattern approximate the resolving power of the inversion across the image space, and highlight smearing regions of smearing.

Lateral resolution of the input model is high in central and western Colorado to depths of ∼ 300–350 km (Figure 2.15). Maximum amplitude recovery in these depths is approximately 70% for both P and S inversions. Some northeast-southwest smearing is visible beneath the CREST footprint, particularly in the S inversion, where one third as many rays are used compared to the P inversion. The relative paucity of crossing rays from northeastern backazimuths likely hampers better northeast-southwest resolution. Horizontal resolution is generally better than vertical resolution in teleseismic body wave tomography, due to the steep incidence angles of most incoming rays. No input spikes were supplied at 150 km depth, and vertical smearing is evident from the ∼0.5% amplitudes at these depths in the recovered model (Figure 2.15). The smoothing and

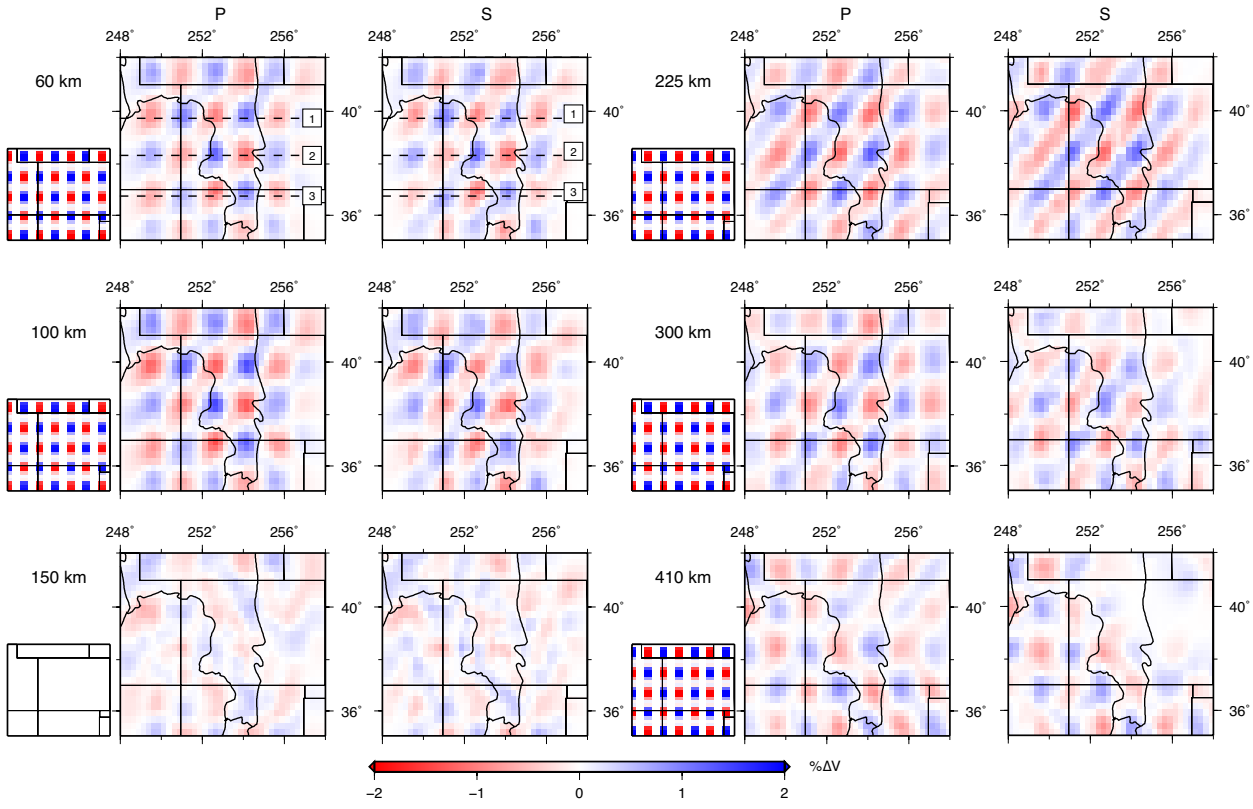

Figure 2.15: Depth slices of P and S checkerboard resolution tests. An input model of alternating clusters of ±2% P (S) velocity perturbation (small tiles) was used to generate synthetic travel time data. Synthetic data with added noise were inverted with the same smoothing and damping as final P (S) velocity models (large tiles). Maximum amplitude recovery for both P and S tests was approximately 70% to depths of 300 km. No input checkers were supplied at 150 km depth. Cross section lines for Figure 2.16 are labeled in the top slice.

vertical smearing inherent in the inversion is more clear in cross section (Figure 2.16), where recovered checkers are generally more broad than those in the input model. Sharp edges of the input spikes are better recovered in the P inversion. Lateral and depth recovery is poor outside of longitudes 249–257 and below 400–450 km depth. Almost no input model recovery is seen in northern and eastern Colorado for the S inversion.

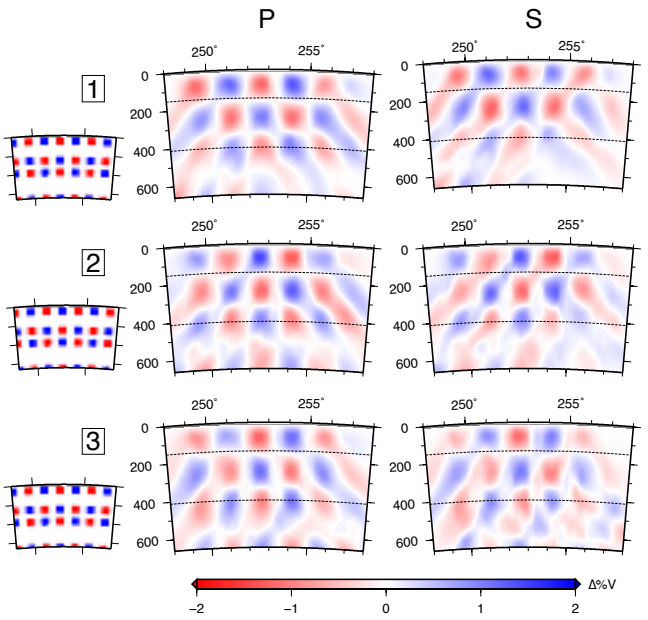

Figure 2.16: Checkerboard resolution test results for P and S inversions. Input model (left), cross sections of P (middle) and S (right) checkerboard resolution tests at latitude 40 (top), 38.5 (middle), and 36.75 (bottom).

We also apply the resolution analysis of MacCarthy et al. (2010) in order to estimate the independent resolvability of model parameters, given the CREST station-source geometry and regularization. This method produces estimates of the diagonal of the resolution matrix, R, for a regularized least squares linear inversion (2.7, 2.8).

$$R = G^{\sharp}G, \tag{2.7}$$

where $G^{\sharp}$ is

$$G^{\sharp} = (G^T G + \alpha^2 L^T L)^{-1} G^T, \tag{2.8}$$

and L is the regularization matrix. Characterization of the resolution matrix diagonal quantifies the degree of parameter underestimation due to smearing in each of the velocity inversions. For further discussion of this method, we refer the reader to MacCarthy et al. (2010) and references therein.

The V_p and V_s inversions have a peak diagonal resolution of 0.17 and 0.25, respectively, in the most highly sampled region of the model space. The difference between these values are largely due to the varying degrees of regularization applied to each inversion, as one would expect the P inversion to achieve higher resolution due to its higher number of used rays. The P inversion is more heavily smoothed and damped compared to that for S (Figures 2.13 and 2.14, Section 2.3.1). As a result, velocities in V_p model parameters are smeared into adjacent blocks to a higher degree than in the V_s model. Also, the choice of relatively small model blocks decreases the resolution of any single model parameter, due to the inherently sparse sampling of the image volume in teleseismic tomography. Larger blocks are sampled by more rays, which results in higher resolution for a given regularization.

2.3 Results

The P and S velocity patterns are broadly consistent across both models, with some anticorrelations (Figures 2.17 and 2.18). The largest amplitude anomalies are primarily above 200-250 km, where the resolving power of the inversions is concentrated. Peak-to-peak anomalies are approximately 7% for V_p and almost 8% for V_s. Apparent northeast-southwest oriented velocity domains are imaged in the upper $\sim$200 km of both models. This is the smearing direction of the images, but the CREST lateral resolution is quite high particularly in the uppermost mantle, so we feel that these apparent domain orientations are robust. Velocities in the northern Colorado Plateau, the Cheyenne belt of southern Wyoming, and the Colorado Great Plains are high above 150 km depth. Slow P and S velocities are present beneath the San Juan and Sawatch mountains and beneath

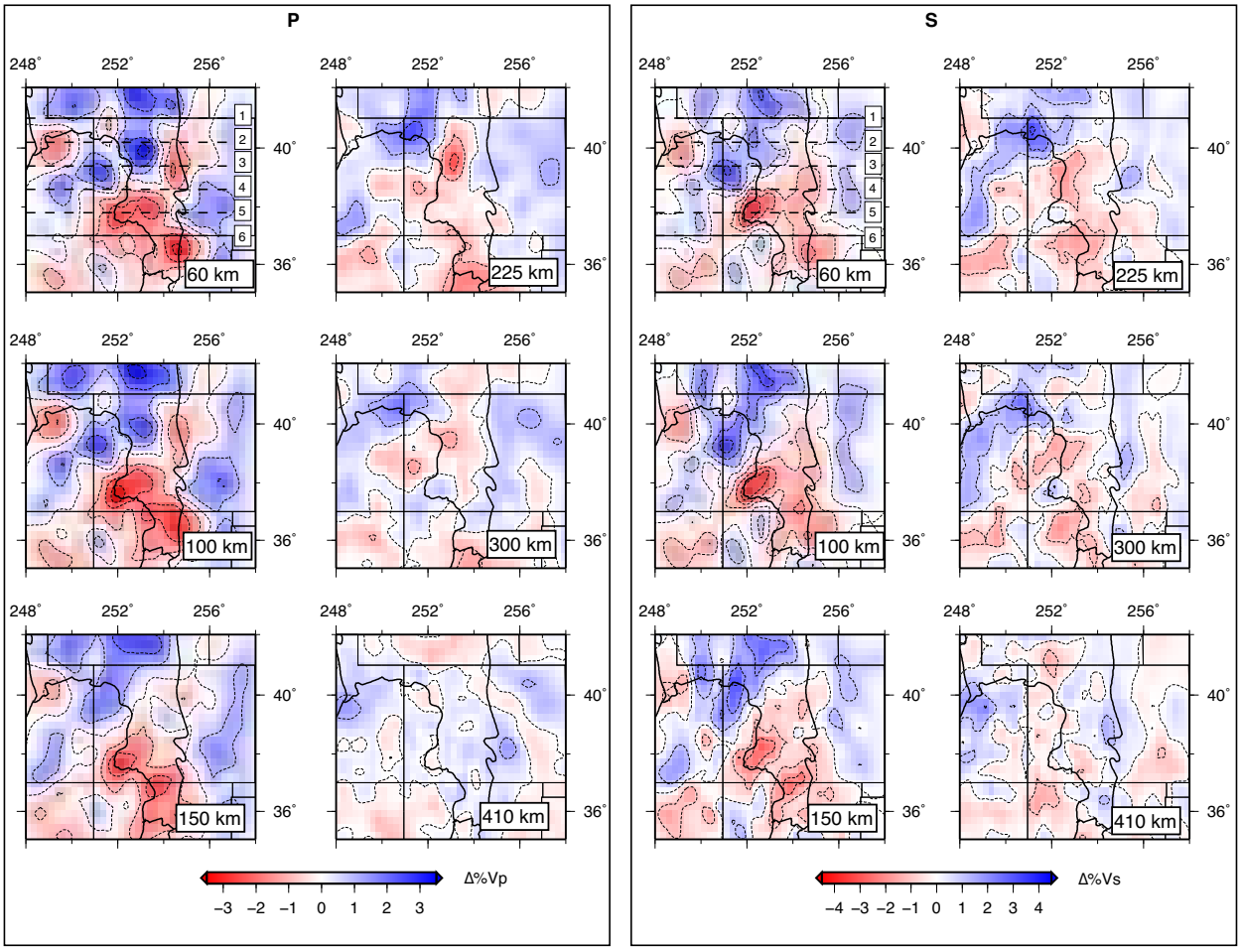

Figure 2.17: P and S velocity model depth slices.

north-central New Mexico to nearly 200 km depth. A broad northeast dipping low velocity channel extends from west–central CO approximately to the top of the mantle transition zone.

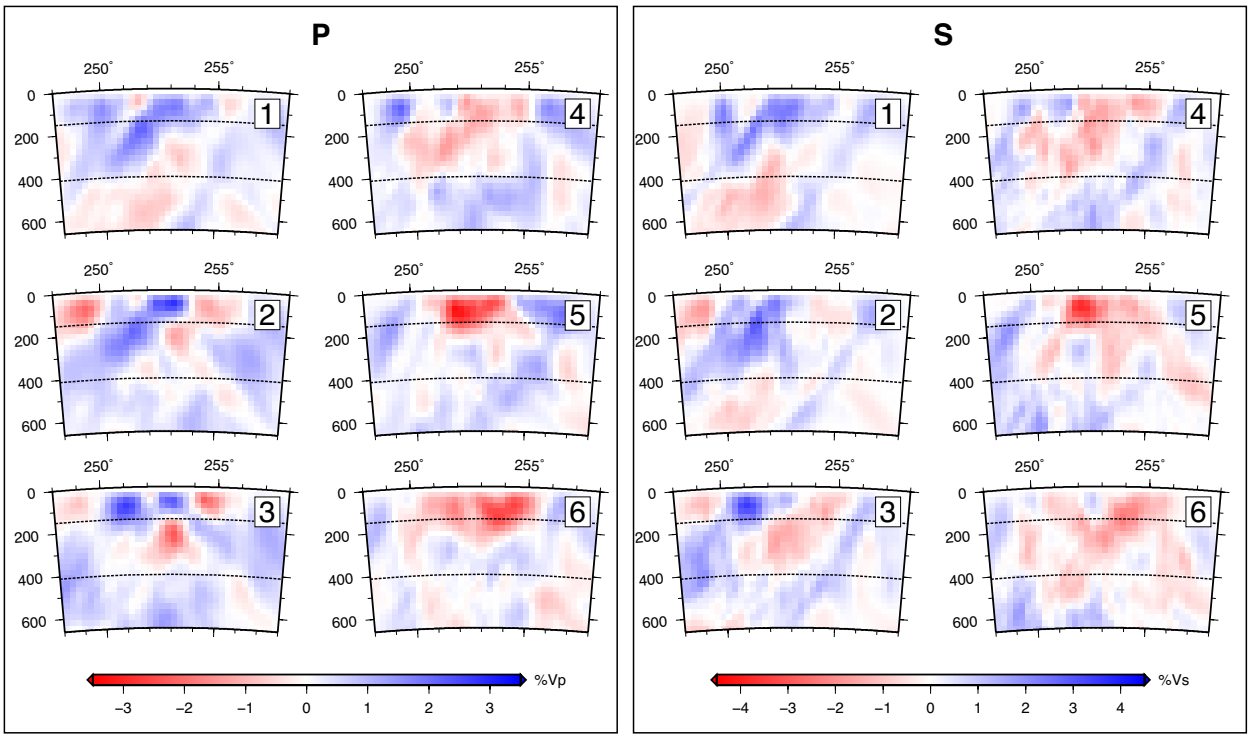

Figure 2.18: P and S velocity model cross sections.

2.3.1 V_p Velocity Structure

The 14,695 relatsive P travel times used in the V_p inversion had an initial RMS of 0.40 seconds, and an RMS after inversion (residue) of 0.14 seconds. The highest RMS station residues were generally at stations at the edge of the network, and near the regions with the largest crustal corrections (Figure 2.8). The RMS of the data standard errors was 0.09 seconds, implying that a component of measured travel times greater than the estimated noise level remains unfit by the preferred velocity model. The regularization weighting was chosen to produce a conservative, slightly over-regularized model, corresponding to a variance reduction of 70.1% (Figure 2.13). This was done in order to minimize the influence of errors in the data and in the model used to produce the crustal corrections. The observation that some of the largest unfit travel times were at stations with the

largest crustal corrections suggests that improvements in the crustal model will likely improve data fit overall.

The primary velocity anomaly beneath the CRM is a low velocity domain in the uppermost mantle beneath the San Juan Mountains, and the eastern margin of the Colorado Plateau (CP) (Figure 2.17). It is -3 to -3.5% V_p and 200-250 km in diameter above 200 km depth, and shows sharp positive gradients onto the CP. Lateral resolution is >75 km in this region of the image volume (Figure 2.15). By 200 km depth, the anomaly is -1 to -2%, has narrowed to <100 km across, and has migrated laterally westward beneath the Uncompahgre Plateau and CP margin. At this depth, it is clearly distinct from low velocities in north central New Mexico possibly associated with the Rio Grande Rift and Jemez Lineament. At 400 km depth, the anomaly is no longer resolved. In cross section, this San Juan anomaly is broad above 200 km depth, but narrows to a west-dipping channel until its terminus at $\sim$ 400 km (Figure 2.18).

Two other low velocity anomalies are imaged beneath the northern CREST footprint. A -1.5 to -2.5% anomaly $\sim$100 km wide is resolved approximately beneath the Front Range near Boulder at 60–125 km depth. Another, possibly associated, -1.5% velocity channel extends from 175 km to 300 km depth roughly beneath the Flat Top Mountains. The Front Range anomaly, the San Juan anomaly, and a high velocity embayment near Cañon City, CO form an irregular boundary between low velocities beneath the CRM and the high velocities of the Great Plains.

At depths above $\sim$150 km, a northeast trending zone of high velocity anomalies extends between the north-central CP and Cheyenne Belt, bordering the low velocities discussed above to the west. It includes previously imaged

high velocities associated with the Wyoming craton and the Green Mountain block ((Dueker & Yuan, 2004)). Peak anomalies in the upper 100 km of this region are 2–3%. The high velocities in southern Wyoming and northwest Colorado form a discontinuous northwest dipping domain that extends to approximately 250 km depth. Below this depth smearing in the inversion makes the anomaly difficult to constrain (Figure 2.16). The 2–2.5% high velocities beneath the northern CP in Utah are primarily above 200 km depth, and are underlain by low velocities that are continuous with the San Juan anomaly.

Recent body wave tomographic results of the western US using data from USArray are broadly consistent with those presented here. V_p anomaly maps from Schmandt & Humphreys (2010) and (Obrebski et al., 2010) both image a corridor of similar amplitude high velocities above 150 km from easternmost Utah to southern Wyoming. This corridor is part of a larger arm of fast, thick lithosphere that extends southwest from northern Wyoming. In these images, low velocities beneath the CRM are slightly lower amplitude than presented here, and are resolved as a single north-south aligned domain. This difference is likely due to higher spatial resolution afforded by the CREST network. An earlier high resolution experiment produced 2D images from Yellowstone to northwestern Colorado (Dueker & Yuan, 2004). Low P velocities of -3 to -4% to $\sim$150 km were resolved at the end of two linear networks, beneath the Uncompahgre highlands and Grand Mesa volcanic field in western Colorado, similar in amplitude to those underneath Yellowstone. High velocities of 3% were also imaged beneath the Green Mountain block of northwestern Colorado.

2.3.2 V_s Velocity Structure

The RMS travel time residue after inversion of 3662 relative S residuals was 0.26 seconds, from an initial RMS of 0.99 seconds. The variance reduction was 78.8%, close to the discrepancy principle value of 82.2% (Figure 2.14). The V_s model is generally positively correlated with the V_p model. In the upper 200 km of the model, northeast-trending fast velocities beneath in eastern Utah, northwest Colorado, and southern Wyoming have a peak anomaly of 3–3.5%, and appear to dip northwestward to approximately 300 km depth (Figures 2.17, 2.18).

A $\sim$7% lateral gradient across the eastern CP margin in Colorado separates northwestern fast velocities from low velocities beneath the San Juan and Elk mountains. Peak anomalies in this $\sim$75 km wide northeast trending feature are –3.5% at 75–100 km depth. Low velocities of -1 to -3.5% extend northeast from the Colorado Four Corners to the eastern Elk Ranges near Aspen, CO. By 200 km depth, the anomaly is -1 to -1.5%, approximately 75 km laterally, and centered beneath the eastern CP (Colorado Plateau) near Grand Junction, CO. The extent to which this feature is continuous with low velocities previously imaged near the Navajo Volcanic Field of Arizona is unclear (Gao et al., 2004), as the Four Corners region is not well resolved in our images. The feature does appear to be continuous with a diffuse zone of -1 to -1.5% anomalies that underlies the CP margin of western Colorado between 200 and 400 km depth.

Velocity patterns the V_s model differ from those in the V_p model in two primary locations. Slightly positive S anomalies are imaged above 150 km beneath the northern San Juan basin in northwestern New Mexico, whereas P velocities are -0.5 to -1% there. Schmandt & Humphreys (2010) also imaged a pattern of

slightly fast V_s anomalies in northwestern New Mexico that differed from V_p patterns. Their anomalies reached ∼200 km, slightly deeper than those imaged here. The low velocity anomaly near Boulder in the P image is not as pronounced in the S image. To test the possibility that variations in P and S crustal correction patterns may be causing these differences in velocity patterns, P and S inversions were performed with no crustal corrections. Turning off crustal corrections reduced data fit (variance reduction) in the P and S inversions by 1–2% and changed some details in the velocity anomaly patterns. Overall V_p variations are reduced from ±3.5% to ±2.75%, and V_s variations were unchanged. The high velocity San Juan anomaly in the S image is reduced in size and amplitude, but the Boulder low P velocity anomaly is largely unchanged by removing crustal corrections.

Without crustal corrections, V_s and V_p images are in slightly closer agreement. If it is assumed that true crustal and mantle V_p and V_s variations correlate positively, than the regions of negative correlation between mantle V_p and V_s models introduced by crustal corrections are due to relative P and S variations in the crustal velocity model, as crustal thickness is constant in the corrections and P and S rays are very similar through the crust. True P and S velocities in the earth very likely do not correlate positively everywhere, because V_p and V_s have different sensitivities to mantle state and velocity anisotropy (Cammarano et al., 2003; Schutt & Lesher, 2006; Moschetti et al., 2010). This makes it difficult to conclusively attribute the two features described above solely to errors in the crustal model. New high resolution V_s models of the crust and uppermost mantle in the CRM region that utilize data from USArray and CREST stations are forthcoming, but are currently unavailable [Dueker, pers. comm.]. Once obtained, these will be integrated into the CREST teleseismic tomography, and will greatly improve the accuracy of teleseismic crustal corrections and the resulting mantle velocity

models. Until these are available, however, caution should be taken in strictly interpreting the two velocity features discussed above.

2.3.3 V_p/V_s Structure

Peak-to-peak V_p/V_s variations are $\sim$3.3% and are generally negatively correlated with both P and S velocity (Figure 2.19) west of the Rocky Mountain Front, and positively correlated in the Colorado Great Plains. Regions of northwestern Colorado, eastern Utah, and southern Wyoming are -1 to -1.5% V_p/V_s to approximately 300 km. Positive V_p/V_s anomalies of up to 1.75–2.0% are present beneath the central Colorado high elevations to approximately 200 km. The Great Plains of southeastern Colorado, however, are generally positively correlated with P and S velocities, with 0.5–1.5% V_p/V_s anomalies throughout the image volume.

Several prominent low V_p/V_s anomalies are imaged beneath western Colorado. Above $\sim$125 km depth, a corridor of 1-2% V_p/V_s extends northward from the San Juan Mountains to the Flat Top Mountains in northwestern CO (Figure 2.19). Between 150–225 km depth, this anomaly is centered beneath Boulder, CO. A $\sim$1.5% V_p/V_s anomaly is imaged beneath the Wet Mountains, primarily above 125 km depth. Below this depth, the anomaly is more broad and associated with high V_p/V_s beneath the Great Plains.

2.4 Mantle State

Body wave velocity variations in the mantle reflect in mantle state, including temperature, bulk composition, anelasticity, nominal volatile/hydrogen content, partial melt, grain size, and mineral orientation/fabric. The linear/nonlinear

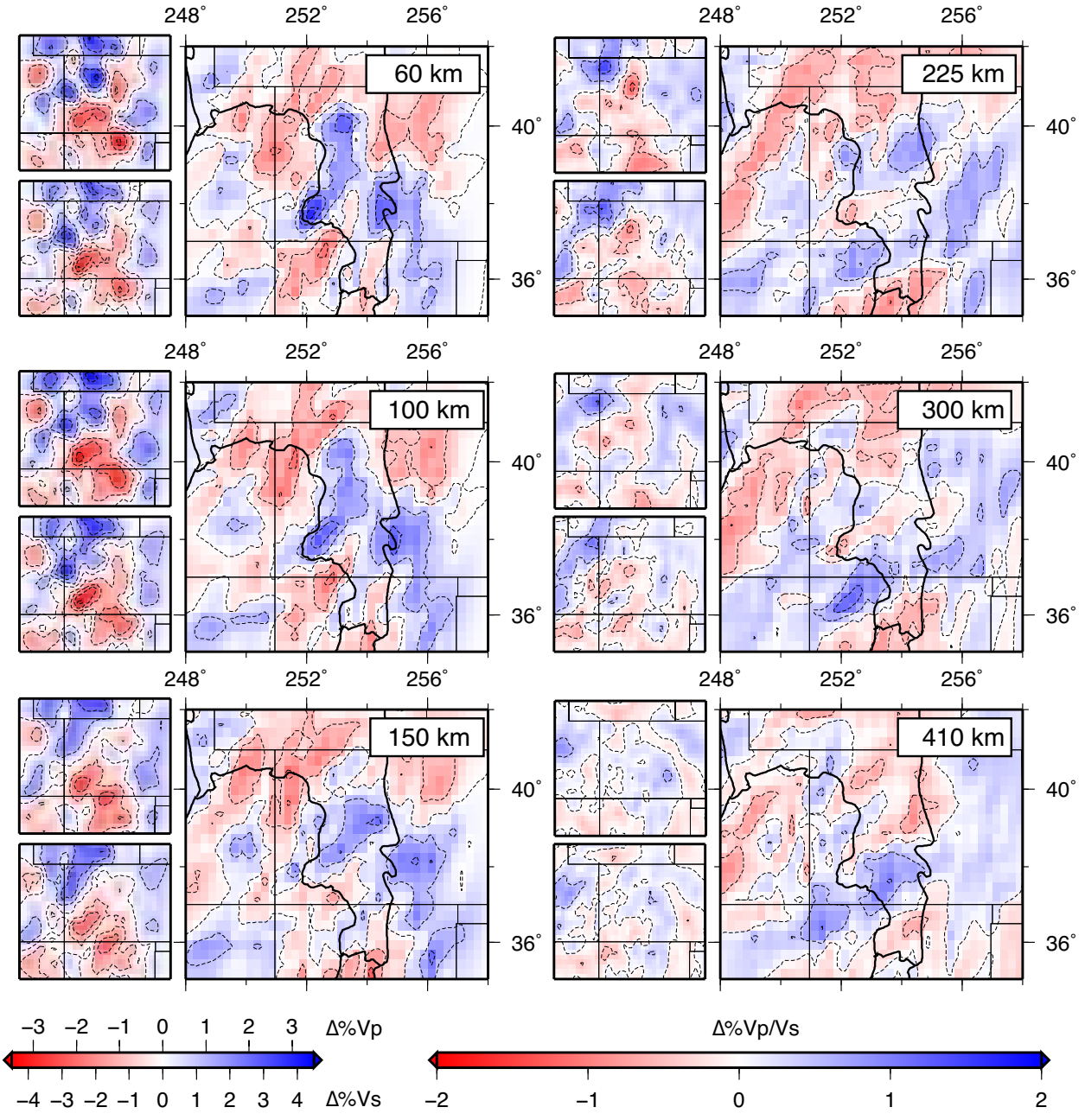

Figure 2.19: Depth slices of V_p, V_s, and V_p/V_s models from joint inversion. Large tiles are the V_p/V_s model, and the upper and lower small tiles are the corresponding joint V_p and V_s slices, respectively.

relationships between seismic velocity (V_p, V_s) and temperature (T), magnesium number ($Mg\# = Mg/(Mg + Fe)$), weight percent hydrogen, density (ρ), quality factor (Q), partial melt fraction (ϕ), grain size (d), and anisotropy form a complex multi-dimensional domain in which velocity anomalies are a function of a non-unique combination factors. Identifying the relative contributions of these competing factors is difficult, but critical in order to understand the state and possible dynamics of the mantle beneath the CRM. Here, we examine three of the most widely accepted factors: temperature, composition, and anisotropy.

2.4.1 Thermal anomaly

Upper mantle velocity anomalies are thought to be largely caused by thermal variations (Goes et al., 2000; Cammarano et al., 2003). The sensitivity of velocity to temperature is heavily dependent on anelasticity (quality factor, Q), particularly in the uppermost mantle where Q is relatively low (KARATO, 1993). Additionally, the sensitivity of seismic velocities to temperature is nonlinear, such that absolute velocity information is important in order to make thermal interpretations (Cammarano et al., 2003). Nonetheless, temperature is a first-order influence on seismic velocity and needs to be considered.

We first consider a simple chemically homogeneous upper mantle composed of "dry" peridotite at a mantle potential temperature of 1300°C and a 1D Q structure. Using $\partial V_p/\partial T$ = -1.2%V_p/100 K (Cammarano et al., 2003), the 5.5% V_p variations in western CO at 100 km depth correspond to almost 450 K temperature variation. For $\partial V_s/\partial T$ of -2%V_s/100 K, the implied temperature variation is 400 K. The smaller 4–4.5% V_p and V_s variation at 200 km in western CO, implies

similar temperature variations, because velocity is less sensitive to temperature with depth.

Because of nonlinearity in the temperature scalings, knowledge of background temperature is critical for interpreting predicted temperature variations greater than 200 K (Cammarano et al., 2003). Increasing background temperature at a constant pressure amplifies velocity–temperature partial derivatives, and thus reduces the implied temperature variation. The CRM region is located within a sharp lateral thermal gradient between relatively cold Great Plains mantle temperatures and relatively hot tectonic western US mantle temperatures, and background temperatures in the southwestern part of the image volume may be 200–400 K hotter than in northeastern CO at $\sim$100 km (Goes & van der Lee, 2002; Godey et al., 2004). Accordingly, the larger amplitude velocity gradients in western CO may be caused by the same scale of thermal variation as the somewhat smaller velocity contrasts in central and eastern CO. A 1% V_s anomaly at 200 km, for example, may imply a temperature difference of 80 K in northeastern CO, but only 45 K in southwestern CO. Temperature variations predicted in western (eastern) CO, therefore, may represent maximum (minimum) values.

Variations in Q affect predicted temperature, and the assumption of laterally constant Q is likely unrealistic. Lower Q means smaller $\partial V/\partial T$, or larger predicted temperature perturbation for the same velocity anomaly (KARATO, 1993; Cammarano et al., 2003). Boyd & Sheehan (2005) did an analysis of relative shear attenuation (Q_s) beneath Colorado. They found that the lowest was beneath parts of the northern Front Range to 150 km depth, coincident with low shear velocities (Lee & Grand, 1996), and was interpreted as thermal in origin. The highest Q_s was beneath the San Juan mountains of southwestern CO, also

coincident with low velocities. This was interpreted as due either to a temperature increase of ∼300 K or to the presence of phlogopite, a hydrous mineral resulting from metasomatism. This relative attenuation pattern would increase the predicted temperature perturbation beneath the Boulder anomaly, and decrease that for the San Juan anomaly. The degree to which the competing effects of variations in background temperature and Q negate each other is unclear, as there are significant uncertainties associated with the thermal models and velocity scaling (Cammarano et al., 2003).

The existence of partial melt in the mantle reduces seismic velocity, and may reduce the predicted thermal variation in the CRM lithosphere if present. Hammond & Humphreys (2000) find that 1% partial melt can cause at least 3.5% V_p and 7.9% V_s reduction. Supersolidus mantle conditions due to higher temperature, lowering of the solidus temperature from hydration, or both could produce partial melt. Given the large volumes of melt extracted from the mantle to produce the San Juan volcanics (Farmer et al., 2008), it is difficult to conceive of a significant fraction of partial melt currently beneath the San Juan anomaly in the absence of a later melting event. Additionally, the depleted lithospheric mantle resulting from basalt extraction would no longer be as fertile as just after Farallon hydration, and would require higher temperatures to melt in the absence of later refertilization.

It is possible, however, that small amounts of partial melt were retained after San Juan volcanisim or a later hydrating event reduced the solidus temperature. A melt fraction as low as 0.25% would reduce the predicted temperature variation to 385 K for V_p and 255 for V_s. Forming and removing even small amounts of partial melt can affect solid state anelastic properties and therefore

velocity–temperature derivatives, so the above partial melt scalings also depend on the "pre–melt" hydration state of the mantle. Karato & Jung (1998) note that generation and removal of partial melt from hydrated mantle can increase seismic velocities by decreasing anelastic effects. In situ partial melt of dry mantle reduces seismic velocities through reduction of elastic moduli (Hammond & Humphreys, 2000).

2.4.2 Compositional anomaly

While there is geological and geophysical evidence for post-Laramide regional heating in Colorado that suggests a thermal origin for low velocities beneath the CRM (McMillan et al., 2002; Eaton, 2008; Reiter, 2008), it is likely that the predicted temperature variations of 400–450 K are too high, as strong evidence also exists for profound chemical modification of CRM mantle lithosphere that may accommodate some observed velocity variation (Lee, 2003; Roy et al., 2004; Farmer et al., 2008). Two Cenozoic geological events modified the thermal and chemical state of western US lithosphere. Shallow subduction of a young oceanic slab during the Laramide orogeny hydrated and refrigerated continental lithosphere as far east as the CRM (Bird, 1984; English et al., 2003; Humphreys et al., 2003). It's subsequent removal in the mid-Tertiary and replacement with hot asthenosphere resulted in widespread magmatism throughout the western US (Coney & Reynolds, 1977; Humphreys et al., 2003). It is estimated that the $\sim$35–18 Ma San Juan volcanic field required a minimum mantle source volume of 7 M km^3 with up to 5% melting by mass (Farmer et al., 2008). The geometry of such a source region and mechanism of magma transfer is unknown, but the result of 5% depletion of lithospheric mantle peridotite can affect seismic velocities and thermal interpretations.

Interpretation of SRM mantle velocities are very dependent on the anelasticity structure. If water (hydrogen) is nominally present (<1%) in minerals such as olivine, pyroxenes, or amphiboles, the sensitivity of seismic velocities to temperature is increased relative to "dry" mantle peridotite. For "wet" conditions, the temperature variations implied by the observed velocity structure are smaller than for dry conditions. For example, V_s sensitivity to temperature is reduced by approximately half when Q_s of 50 (wet) increases to 200 (dry). There is xenolith evidence for widespread hydration of western US lithosphere resulting from oceanic plat shallow subduction during the Laramide (Lee, 2003; Dixon et al., 2004; Li et al., 2008b), however the eastward extent is of hydration is unclear. Xenoliths exhibiting cold temperatures and high water content from the Navajo volcanic field in the central CP are well documented (Smith, 2000; Li et al., 2008b), but Laramide and younger xenoliths are rare in CO. The Laramide hydration state of the SRM is thus unclear, though it is understood that generation of large volumes of granites, such as the Laramide plutons along the COMB and the volcanics of the San Juan volcanic field, requires the presence of water. The extent to which middle Tertiary magmatism may have "dried" the upper mantle is also unclear. Young volcanism in the Basin and Range and the Rio Grande Rift show chemical characteristics consistent with hydrated mantle sources (Dixon et al., 2004), so it seems possible to retain presumed Laramide–age hydration into the middle–late Miocene. These locations, however, did not experience mantle partial melting to the same extent as that for the San Juan volcanic centers (Farmer et al., 2008). It is important, then, to interpret mantle state in southwest Colorado in terms of both wet and dry mantle conditions.

The anharmonic sensitivity of seismic velocities to basalt depletion is still debated (Jordan, 1981; Lee, 2003; Schutt & Lesher, 2006; Afonso et al., 2010), but

it is generally agreed that partial melting can change the anelastic properties of mantle lithosphere, and significantly affect seismic velocities (Karato & Jung, 1998). Even very small amounts of fractional melting of nominally hydrated olivine will preferentially remove the hydrous components and increase the Q of the residuum, resulting in higher seismic velocities if the melt is removed. Spatially varying melt extraction following widespread hydration of the base of the western US lithosphere is a possible mechanism to generate hydration–related velocity heterogeneity. Regions where (nominally) hydrous partial melt has been extracted may remain hot, but will have a higher Q than adjacent hot regions with lower or no extraction, or where melt was generated but not removed. Hot, depleted mantle may manifest in seismic images as anomalously slow, but with low relative attenuation, as with the San Juan low velocity anomaly compared to the Boulder anomaly (Lee & Grand, 1996; Boyd & Sheehan, 2005). The San Juan anomaly, therefore, may represent relatively unhydrated mantle lithosphere within the SRM. If this is the case, the San Juan anomaly low velocities imply unreasonably high temperatures, and seem to require large amounts of partial melt.

2.4.3 Effects of anisotropy

The V_p and V_s models presented here are produced under the assumption of isotropic velocity variations. The CRM mantle, however, is within a region of changing anisotropic regimes (Yuan & Romanowicz, 2010a,b). Joint inversion of long-period waveforms and SKS splitting measurements by Yuan & Romanowicz (2010a) reveal $\sim$1% northeast oriented anisotropy in southwestern CO above 100 km, diminishing to the northeast. Roughly uniform $\sim$1.5% northwest oriented anisotropy is modeled at 200 km depth across CO. By 400 km, however,

two nearly orthogonal regimes of low anisotropy are modeled straddling the Front Range. When uniform anisotropy is present in an image volume, measured travel time delays are uniformly affected across the network and the removal of event mean delays also removes this effect. However, when varying anisotropy is present, the emerging wavefront beneath a network is warped nonuniformly depending on the event backazimuth and the seismogram component used in the measurements. For example, below 300 km, a northeast oriented fast direction is modeled beneath eastern CO and the fast direction is northwest oriented in western CO. P waves arriving from an event in the northwest will travel faster through western CO relative to eastern CO in this depth interval (all other things being equal), possibly increasing (decreasing) mantle P velocities beneath western (eastern) CO in the isotropic velocity model. The effect is more complicated for S arrivals, which must be measured in a projected coordinate system, the orientation of which may have significant effect on measured travel time residuals resulting from a polarizing medium.

Anisotropy is one of the mechanisms through which anticorrelation between P and S velocity variations can be generated (Yuan & Dueker, 2005). The actual effects of 3D anisotropy beneath the CRM region is difficult to calculate without incorporating anisotropy into the inversion, or correcting measured residuals before inversion for the integrated effects of predicted isotropic variations. We note, however, that the strongest anisotropy in the image volume is a layer of uniform $\sim$1.5% northwest oriented fast direction at 150–250 km depth, which does not influence the isotropic velocity images as mean travel time variations are removed Yuan & Romanowicz (2010a). Above and below the uniform layer, little anisotropy is modeled beneath eastern CO, so we might expect imaged velocity anomalies beneath eastern CO to be quite close to the true isotropic values. In western CO, polarization above and below the uniform layer are roughly

orthogonal in orientation and of similar magnitude (∼1%). These two regimes have somewhat opposite effects on measured residuals depending on the event azimuth and measurement system, but because mantle velocities increase with depth and the effect of anisotropy is an integrated value, we might expect the shallow southwest oriented fast direction to have a larger effect on the data. Our event distribution is dominated by northwestern and southeastern azimuths (Figures 2.3 and 2.4). We adopted the transverse component system for S residual measurements. From northeastern/southwestern event azimuths, this system is parallel to the fast direction west of the Front Range above 150 km. S arrivals would therefore "see" faster mantle west of the Front Range relative to eastern CO, and relative to P arrivals from the same events. This "coloring" of S data may help explain a relatively low S to P residual slope of 2.15, determined by least squares linear regression of residuals from approximately 1,800 shared sources and stations. Using a Q_p of 200 and a Q_s of 85, KARATO (1993) predicts a slope of 2.9 for purely thermal effects. The degree to which P and S residuals may change is unknown without correcting for modeled anisotropy, but we feel that the S to P residual slope would likely increase, and S velocities west of the Front Range would be lower.

2.5 Discussion

2.5.1 Influence of Proterozoic lithospheric structure

The velocity anomalies imaged above approximately 100–150 km depth by CREST show a remarkable correlation with northeast–oriented Proterozoic lithospheric structures (Figure 2.17). High velocities in northwestern CO follow

the southern tectonic boundaries of the Proterozoic Green Mountain arc and Mojave Province (Dueker & Yuan, 2004; Whitmeyer & Karlstrom, 2007). The San Juan and Boulder low velocity anomalies are aligned with the Colorado Mineral Belt (COMB) (Tweto & Sims, 1963; Karlstrom & Humphreys, 1998), and a third low velocity anomaly in northern New Mexico is below the intersection of the Jemez Lineament and the northern Rio Grande Rift, near the Latir volcanic field (Yuan & Dueker, 2005). Below ∼150 km velocity domains are less correlated with proposed lithospheric features, and in some places anticorrelated with shallower velocities (Figure 2.18). The depth range of 100–150 km also roughly corresponds to a change in azimuthal anisotropy from that oriented with plate motion generated shear to that oriented with proposed mantle flow, from joint inversion of long period waveforms and SKS splitting measurements (Yuan & Romanowicz, 2010a,b). For these reasons, we feel that body wave tomography is consistent with a heterogeneous but mostly intact lithosphere to approximately 125–150 km depth throughout most of the SRM.

High velocity mantle lid is absent beneath the San Juan anomaly, and its proximity to the extended San Luis basin of the northern Rio Grande Rift suggests the possibility of replacement by asthenosphere. The same observation may, however, be explained by the thermal "astenospherization" of otherwise mechanically strong lithosphere. While predicted temperatures beneath the San Juan anomaly are high, it would be difficult to erode the base of the lithosphere given the increase in viscosity incurred from removing partial melt from large volumes of upper mantle (Karato & Jung, 1998; Farmer et al., 2008; Roy et al., 2004) without a later hydrating event. Additionally, lithospheric layering is preserved beneath western CO to depths of ∼100 km, as imaged by receiver functions [Hansen and Dueker, in prep.]. This model is consistent with a chemically

depleted, thermally conductive layer beneath Proterozoic (and Archean) lithosphere recently hypothesized by Yuan & Romanowicz (2010b).

2.5.2 Support for high elevations

Previous estimates of mantle buoyancy contributions beneath the CRM relied upon seismic data of lower resolution than are now available. Sheehan et al. (1995) estimated a 1% density anomaly beneath the CRM, using (single-station) receiver function estimates of ∼50 km average CRM crustal thickness to match observed topography and gravity patterns. S wave variations of 9% from Lee & Grand (1996) were consistent with these estimates when temperature variations of 350 K and 1.5% partial melt were invoked. Multi-station receiver function crustal thickness estimates from the CREST dataset are nearly 5 km lower and anticorrelated with topography [Hansen and Dueker, (in prep)], implying a larger degree of crustal and/or mantle density compensation. Mantle V_s anomaly patterns and amplitudes imaged in the present study and others (Schmandt & Humphreys, 2010; Obrebski et al., 2010) are similar to those of Lee & Grand (1996). If crustal velocities (densities) are not significantly lower than those assumed in the previous studies, than a higher degree of compensation must be attributed to the mantle.

An alternate explanation to high temperature and partial melt content for low lithospheric velocities beneath the SRM is the presence of wet mantle conditions, which would reduce the predicted temperature (and hence density) variations of the mantle lithosphere. This may create a problem, however, in terms of compensation for high elevations, if density variations are reduced. A contribution from buoyant sublithospheric mantle may explain this discrepancy. A

northwest dipping low velocity channel is imaged from 150 km depth to approximately the top of the mantle transition zone (Figure 2.18). The geometry and amplitude of the anomaly is consistent with regional tomography of Schmandt & Humphreys (2010), Obrebski et al. (2010), and global tomography of Simmons et al. (2006), the latter of which was used to model mantle flow beneath and adjacent to the Colorado Plateau to explain its high elevations (Moucha et al., 2008). The upwelling was coupled to the downgoing Farallon slab, and it was predicted to produce young (<10 Ma) dynamic topography of ∼750 m. This deep source, combined with low density lithosphere, may provide the buoyancy necessary to produce the high average elevations of the SRM, though uncertainties in seismic velocity amplitudes, velocity scaling, and dynamic modeling preclude precise prediction of elevation.

2.6 Conclusions

Tomographic inversions of P and S body wave travel time delays across the Southern Rocky Mountains produce high resolution 3D models of V_p and V_s of the upper mantle to the top of the transition zone. We find pervasive low velocities in the lithosphere beneath the San Juan volcanic centers, as well as a northwest dipping low–velocity channel beneath the northern Colorado Pleateau. The amplitude of low velocities may imply a strong contemporary thermal and density perturbation and partial melt beneath the SRM, depending on the assumed hydration state of the uppermost mantle. Sublithospheric low velocity patterns are consistent with large–scale convective modeling of upwelling mantle beneath the Colorado Plateau (Moucha et al., 2008; Moucha et al., 2009). Growing evidence for widespread low velocity mantle above the transition zone in the south-

western US Song et al. (2004); Gao et al. (2006); Jasbinsek et al. (2010) may also imply a role for low–velocity hydrated mantle upwellings (Richard et al., 2010).

CHAPTER 3

EFFICIENT STOCHASTIC ESTIMATION OF THE MODEL RESOLUTION MATRIX DIAGONAL AND GENERALIZED CROSS VALIDATION FOR LARGE GEOPHYSICAL INVERSE PROBLEMS

Abstract

In recent years, larger geophysical datasets and novel model parameterizations have dramatically increased both the data and model space dimensions of many inverse problems. Because of their relatively low computational expense, trade–off curve corner estimation for choosing regularized models and "checkerboard" tests for evaluating model resolution are commonly applied, despite their limitations. We present and demonstrate a low cost method for accurately estimating the diagonal elements of the model resolution matrix diagonal and for implementing generalized cross validation (GCV) for optimal regularization parameter selection. The ability to estimate the diagonal of the resolution matrix and GCV function thus facilitates the introduction of additional tools for diagonal resolution analysis and regularization evaluation, even for very large inverse problems. We demonstrate the method using a Tikhonov regularized teleseismic body wave velocity inversion example with approximately 260,000 model parameters, where we validate selected $\mathbf{R_m}$ diagonal elements against explicitly calculated values and compare GCV-estimated regularized model results to those obtained through traditional methods.

3.1 Introduction

Recent expansion of seismic data availability and innovations in model parameterization motivate the need for computationally tractable, unbiased, and easy to implement resolution estimators.

Regularized linear inversions are central to geophysics, due in part to their favorable statistical characteristics (Berryman, 2000; Aster et al., 2005), the availability of efficient iterative solvers for large systems, such as LSQR (**?**), and the commonly ill–posed nature of the inverse problem. Even as the size and complexity of linear or linearized inverse problems grows, iterative solvers are able to produce solutions efficiently. Analyzing the balance between model resolution and regularization, however, becomes considerably more computationally intensive than producing solutions.

The choice of regularization parameters affect solution resolution, which generally degrades as regularization constraints, such as solution bounds or smoothness, are added. An optimal degree of regularization is commonly estimated through the use of trade–off curves between a model norm (or seminorm) and the forward modeled misfit with observed data (Hansen & O'Leary, 1993). When the statistical character of the data noise is unknown or only roughly estimated, as is commonly the case, this choice can be rather arbitrary. Generalized cross validation (GCV) provides a well-characterized method of selecting a regularization parameter that minimizes the predictive data errors in a least squares solution (Golub et al., 1979). However, GCV requires calculating the trace of a large matrix, which, when approached straightforwardly, is commonly computationally prohibitive for large inverse problems.

Recent work by Bekas et al. (2007) on the statistical estimation of the large matrix diagonals provides a notable new tool to facilitate both resolution analysis and implementation of GCV for large geophysical inversions. Here, we illustrate the application of this stochastic method to produce unbiased and accurate estimates of the GCV function and the diagonal elements of the model resolution matrix, apply this method to a moderately large teleseismic tomographic inverse problem, and provide associated self-contained MATLAB functions (supplementary materials).

3.2 Resolution and regularization

Here we define the model resolution matrix for a Tikhonov regularized linear forward problem of the form

$$\mathbf{Gm} = \mathbf{d}, \tag{3.1}$$

where $\mathbf{G}$ is the forward operator matrix, $\mathbf{m}$ is an n–dimensional model vector, and $\mathbf{d}$ is an m–dimensional data vector. Each constraint equation in this system is assumed to be weighted by an estimate of the respective data error standard deviation.

Because many geophysical inverse problems are ill–conditioned and/or rank deficient, additional constraints are typically needed for solution stability and uniqueness (Menke, 1989; Parker, 1994). We implement regularization here by incorporating a roughening matrix, $\mathbf{L}$, and its associated weighting parameter, α, into the inverse problem (3.1). The resulting Tikhonov regularized least squares problem is

$$\min \left\| \begin{bmatrix} \mathbf{G} \\ \alpha\mathbf{L} \end{bmatrix} \mathbf{m} - \begin{bmatrix} \mathbf{d} \\ \mathbf{0} \end{bmatrix} \right\|_2 . \tag{3.2}$$

It can be shown using the normal equations that the least squares solution can be expressed by a linear matrix inverse operator acting on the data vector

$$\mathbf{m}_\alpha = \mathbf{G}^\sharp \mathbf{d} \,, \tag{3.3}$$

where

$$\mathbf{G}^\sharp = (\mathbf{G}^T\mathbf{G} + \alpha^2\mathbf{L}^T\mathbf{L})^{-1}\mathbf{G}^T \tag{3.4}$$

(Aster et al., 2005). The model resolution matrix characterizes the linear model space mapping between a (typically unknown) true model and that recovered using (3.3), i.e., for some true model $\hat{\mathbf{m}}$ with noise-free associated data $\hat{\mathbf{d}}$,

$$\mathbf{m}_\alpha = \mathbf{G}^\sharp\hat{\mathbf{d}} = \mathbf{G}^\sharp\mathbf{G}\hat{\mathbf{m}} = \mathbf{R}_\mathbf{m}\hat{\mathbf{m}} \,. \tag{3.5}$$

$\mathbf{R}_\mathbf{m}(\mathbf{ff}) = \mathbf{G}^\sharp\mathbf{G}$ is an n by n square matrix that characterizes the model bias inherent in the regularized inversion. Columns of $\mathbf{R}_\mathbf{m}$ are resolution kernels corresponding to point spread (i.e. spike test) functions for each model parameter. Off-diagonal entries represent smearing/trade–off between parameters in the recovered solution, and diagonal entries characterize the independent resolvability of each parameter. The closer $\mathbf{R}_\mathbf{m}$ is to the identity matrix, the less bias inherent in the inversion, and the higher the fidelity of the solution will be to the unknown true model that generated the observed data. A significant difficulty in calculating $\mathbf{R}_\mathbf{m}$ directly is that, although $\mathbf{G}$ may be sparse (as in a typical seismic tomography problem), $(\mathbf{G}^T\mathbf{G} + \alpha^2\mathbf{L}^T\mathbf{L})^{-1}$ in (3.4) is typically an n by n dense matrix. For problems with n larger than a few tens of thousands of parameters, this can require in excess of many tens of gigabytes of storage and prohibitively time consuming calculations.

Because of the central importance of this problem for large linear or linearized inverse problems, a number of methods have been proposed to estimate

or calculate the full resolution matrix (3.5). Approaches include iterative methods that complement the LSQR algorithm (Zhang & McMechan, 1995; Yao et al., 1999; Zhang & Thurber, 2007). These methods, while taking advantage of the computational efficiencies of the LSQR algorithm, produce an "effective resolution matrix," that may not fully represent the model resolution (Deal & Nolet, 1996; Berryman, 2000; Zhang & Thurber, 2007). Nolet et al. (1999) formulated an explicit expression for an approximation to the resolution matrix using a one-step back–projection method. This method, however, makes special assumptions about the structure of the forward operator. Finally, a highly computationally intensive class of methods exploits Choleski factorization and parallel computation to evaluate model resolution (Boschi, 2003).

Both the least squares solution and the model resolution in (3.3) and (3.5) are dependent on the choice of regularization roughening matrix $\mathbf{L}$ and its weighting parameter, α. GCV selects the regularization parameter that minimizes the predictive error for all data points when left out one at a time. This is done by minimizing the GCV function, $V_0(\alpha)$,

$$V_0(\alpha) \approx \frac{m\,||\mathbf{G}\mathbf{m}_\alpha - \mathbf{d}||_2^2}{\mathrm{Tr}(\mathbf{I} - \mathbf{G}\mathbf{G}^\sharp)^2}, \tag{3.6}$$

where Tr denotes the matrix trace and m is the data space dimension (Craven & Wahba, 1979). Golub & vonMatt (1997) applied a stochastic trace estimator to estimate (3.6), but did so by calculating upper and lower bounds through a more complex method than that presented here. The stochastic matrix diagonal estimator presented here is independent of the number of iterations used to find the model solution and makes no assumptions of the structure of the forward operator.

3.3 Stochastic estimation of a matrix diagonal

The following algorithm comes largely from Bekas et al. (2007), who applied it to atomic density functional theory and noted its broad relevance, and is in turn based upon work by Hutchinson (1990) and Girard (1987). Here, we apply the matrix diagonal estimator to the resolution matrix (3.5) and the calculation of the GCV function (3.6).

Consider a sequence of s n-length random vectors, $\mathbf{v}_1, \ldots, \mathbf{v}_s$, with independent elements drawn from a standard normal distribution. The s^{th} estimate for the diagonal of an n by n square matrix $\mathbf{A}$ is then

$$\mathbf{D}_s = \left[\sum_{k=1}^{s} \mathbf{v}_k \odot \mathbf{A}\mathbf{v}_k \right] \oslash \left[\sum_{k=1}^{s} \mathbf{v}_k \odot \mathbf{v}_k \right], \tag{3.7}$$

where $\odot$ signifies element-wise vector multiplication and $\oslash$ signifies element-wise vector division.

In practice, the choice of s will depend on the desired accuracy of the diagonal determination, which can be assessed by statistically examining repeated estimates generated with independent random vectors and by the convergence of the estimates $\mathbf{D}_s$. Equation (3.7) contains the matrix-vector product $\mathbf{A}\mathbf{v}_k$, which cannot be evaluated directly if $\mathbf{A}$ is incalculable. When $\mathbf{A}$ is the resolution matrix, $\mathbf{R_m}$, this product can be computed by noting that a product $\mathbf{y} = \mathbf{R_m}\mathbf{v}_k$ can be rewritten in terms of the known matrices $\mathbf{G}$ and $\mathbf{L}$ by combining (3.5) and (3.4) as

$$\mathbf{y} = (\mathbf{G}^T\mathbf{G} + \alpha^2\mathbf{L}^T\mathbf{L})^{-1}\mathbf{G}^T\mathbf{G}\mathbf{v}_k \,, \tag{3.8}$$

which is the normal equations solution for

$$\min \left\| \begin{bmatrix} \mathbf{G} \\ \alpha\mathbf{L} \end{bmatrix} \mathbf{y} - \begin{bmatrix} \mathbf{G}\mathbf{v}_k \\ \mathbf{0} \end{bmatrix} \right\|_2 . \tag{3.9}$$

In estimating the GCV function (3.6), let $\mathbf{A}$ be $\mathbf{G}\mathbf{G}^\sharp$. We first evaluate the product $\mathbf{y} = \mathbf{G}^\sharp\mathbf{v_k}$ as

$$\mathbf{y} = (\mathbf{G}^T\mathbf{G} + \alpha^2\mathbf{L}^T\mathbf{L})^{-1}\mathbf{G}^T\mathbf{v}_k \,, \tag{3.10}$$

which is the normal equations solution for

$$\min \left\| \begin{bmatrix} \mathbf{G} \\ \alpha\mathbf{L} \end{bmatrix} \mathbf{y} - \begin{bmatrix} \mathbf{v}_k \\ \mathbf{0} \end{bmatrix} \right\|_2 . \tag{3.11}$$

The least squares solution to (3.11) is subsequently left–multiplied by $\mathbf{G}$ to obtain the desired matrix–vector product $\mathbf{G}\mathbf{G}^\sharp\mathbf{v_k}$ in (3.7). Once the diagonal of $\mathbf{G}\mathbf{G}^\sharp$, and hence its trace, are estimated, calculating (3.6) is trivial. Both (3.9) and (3.11) can be readily solved with an iterative solver such as LSQR.

The computational cost of using this algorithm to minimize the GCV function in terms of the number of LSQR calls required, is $s \cdot p$, where p is the number of regularization weighting parameters tested. Estimating the resolution matrix diagonal requires only s calls to LSQR.

3.4 An example from teleseismic tomography

We apply the method to select the regularization parameter and estimate the resolution matrix diagonal for a moderately large seismic tomographic inversion. The CREST (Colorado Rockies Experiment and Seismic Transects; (Aster et al., 2009; MacCarthy et al., in prep)) teleseismic inversion data subset examined here consists of 19,608 mean-removed teleseismic P-wave travel time residuals and estimated data errors, measured at 167 broadband seismic stations in the region (MacCarthy et al., in prep). The model space is parameterized by 267,520 constant slowness blocks, each 0.25° by 0.25° by 25 km in size. The forward

problem matrix was constructed via infinite frequency raytracing through a one–dimensional reference velocity model (ak135; (Kennett et al., 1995)) with crustal corrections, and solutions are expressed as percent velocity or slowness variation from this model.

Forward problem constraint equations were scaled by respective standard deviations estimated from ensemble P arrival waveform crosscorrelation (using approximately one principal period of the first arrival) across the network (Vandecar & Crosson, 1990). Analysis of data errors suggested that the crosscorrelation methodology underestimates the true measurement errors. We note that other authors have reached similar conclusions, suggesting that a factor of 2–10 typically brings crosscorrelation derived error estimates in teleseismic inversion data sets closer to those estimated by data analysts (Waite et al., 2006; Pavlis & Vernon, 2010). We find that scaling crosscorrelation–determined error estimates by a factor of 4 brings the model seminorm versus residual trade–off curve corner and GCV minimum into consistency with the noise level, per the discrepancy principle describing statistically expected data fit (Hansen & O'Leary, 1993; Aster et al., 2005) and have adopted this scaling factor in further work with this data set.

Like most geophysical tomographic inversions, this example is rank–deficient. We thus regularize the inversion using superimposed zeroth–order and second–order (Laplacian) smoothing in equal proportion, scaled by the regularization parameter α, and by a constant level of edge–damping (MacCarthy et al., in prep). We examine the selection of the regularization parameter using trade–off curves and via GCV, and use the different recovered models to demonstrate the use of the diagonal resolution estimation algorithm in solution bias characterization.

In trade–off curve analysis, α was selected visually from the corner vicinity of the plot of data residual versus model seminorm (Figure 3.1a). The corner provides a heuristic for estimating an optimal degree of regularization, but its character will be influenced by the plotting range and scale (e.g., linear, linear-log, or log-log plotting are variously used in practice). It is common for preferred models in such studies to be somewhat over–regularized relative to the mathematically "best" solution in the interest of producing stable, conservative, or geologically reasonable models. We show a model that is slightly towards the smoother side of a linear-linear trade–off curve, corresponding to α = 0.7 (Figure 3.2a–c). This particular model has maximum amplitudes of $\pm$4.5% in V_p and corresponds to a data variance reduction of 78.7% (a root–mean–square data fit of 89%) compared to ak135.

We next determined α to minimize the GCV function (3.6). The GCV–optimal α for the CREST inversion, selected from its broad minimum, is near 0.1 (Figure 3.1b, 3.2d–f). While structurally similar to the model with $\alpha = 0.7$, maximum amplitudes in this model are $\pm$6.8%, with a data variance reduction of 91.7%. Note that these high amplitude P-wave variations are believed to be petrologically infeasible, and the high roughness (large seminorm) of the GCV–optimal model likely indicates that this particular solution is unduly rough.

We show both a checkerboard resolution test and estimated model resolution diagonals for the two example regularized solutions discussed above to illustrate the effect of regularization weighting on resolution and to highlight how the two methods of resolution analysis offer different insights. Alternating 3^3-block clusters of $\pm$2% Vp were used to generate synthetic travel time data

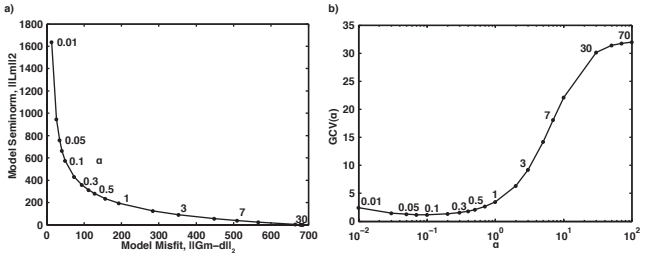

Figure 3.1: a) Example trade–off curve between model seminorm versus data residual 2-norms as a function of regularization weighting parameter, α (3.2) for regularization as described in the text. b) Generalized cross validation (GCV) curve, showing regularization parameter (α) versus GCV function value (3.6).

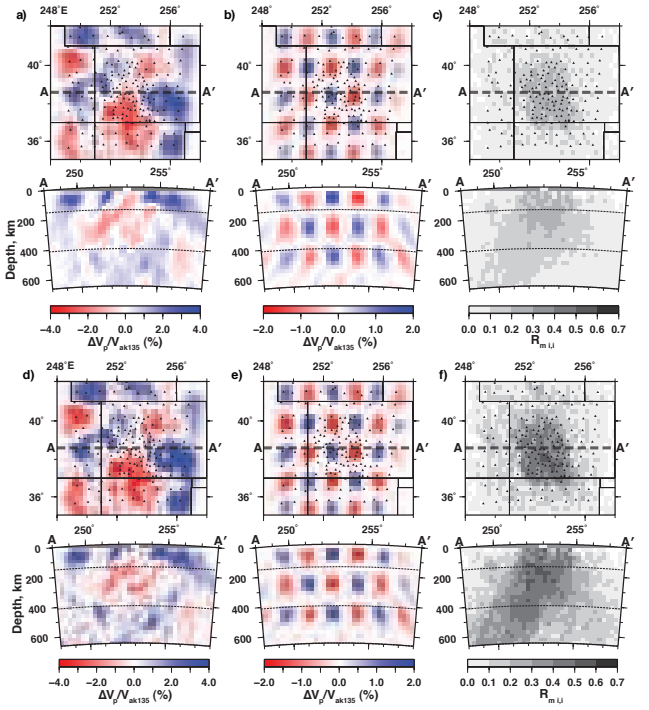

Figure 3.2: CREST Colorado-region model slices and resolution analysis of example regularized inversions with α = 0.7 (a–c) and with α = 0.1 (d–e). (a,d): depth slice of velocity model at 90 km depth (top). Seismic stations are small black triangles, and the dashed line $\mathbf{AA'}$ is the location of the paired cross section (bottom). Depths at 150 km and 440 km are shown as dashed lines in cross section. Velocities are %Vp relative to the ak135 reference model. (b,e): Checkerboard recovery at same depth and latitude as previous. Input perturbations were $\pm$2% P velocity relative to background across sets of 3^3 model blocks. (c,f): Stochastic estimate of diagonal elements of $\mathbf{R_m}$.

using the CREST forward problem, and the data were contaminated with noise at the same level as that estimated for the CREST data. The synthetic data were then inverted using the same α = 0.1 and 0.7 inversions as previously discussed. The resulting checkerboard recovery models are a rough approximation of a spatial distribution of superimposed respective resolution kernels within the model space (Figures 3.2b, 3.2e). The tests highlight regions with high shape and amplitude recovery, versus poorly constrained regions dominated by smearing. A significant shortcoming of this approach, however, is that interpreting amplitude recovery for a given parameter is complicated by smearing/superposition from adjacent parameters. For example, maximum amplitude recovery for the α = 0.1 and 0.7 solutions is greater than the input amplitude for both checkerboard inversions. Because of this effect, the recovered models for both inversions look very similar and quantitative distinctions of amplitude recovery between different inversions is difficult. The model resolution matrix diagonal is a more quantitative measure of amplitude recovery that is independent of the geometry of synthetic input models.

The stochastic method of Section 3.3, using s = 256 random vectors, was used to estimate the model resolution matrix diagonal for the two regularized inversions. For each diagonal estimation, a random subset of 100 estimated elements were validated against explicitly calculated elements. Estimated elements appeared to be approximately normally distributed. Stable values were obtained by running 20 realizations of the diagonal estimation and calculating median values. The mean absolute error of the estimates was 0.005 for the $\alpha = 0.1$ inversion and 0.002 for the $\alpha = 0.7$ inversion.

While the pattern of well-resolved regions is similar between the two inversions, the amplitude bias is notably different (Figures 3.2c, 3.2f). The resolu-

tion diagonal in the $\alpha = 0.7$ model is nearly half that of the $\alpha = 0.1$ model, with maximum $\mathbf{R_m}$ diagonal values of 0.375 and 0.618 respectively. This implies a much larger degree of smoothing inherent in the $\alpha = 0.7$ inversion that is not apparent through the corresponding traditional multiblock checkerboard analysis. A drawback of looking only at the $\mathbf{R_m}$ diagonal, of course, is not being able to visualize smearing bias in the inversion. However, the degree of smearing can be quantified by the $\mathbf{R_m}$ diagonal value complement $\mathbf{I} - \mathbf{R_m}$.

3.5 Conclusions

We present a low cost stochastic matrix diagonal method to estimate the model resolution matrix diagonal and the generalized cross validation (GCV) function. The method is demonstrated using a moderately large teleseismic P velocity linear inversion example, and the results are compared against those from trade–off curves and checkerboard resolution tests. The stochastic matrix diagonal estimation method presented here relies on LSQR and is comparable in computational demand to the effort necessary for obtaining model solutions. The method thus provides easily implemented estimation and assessment of the complete resolution matrix diagonal as well as wider usage of GCV–determined regularization parameter estimation and is scalable to very large inverse problems.

Acknowledgments

Seismic instruments were provided by the Incorporated Research Institutions for Seismology (IRIS) through the PASSCAL Instrument Center at New

Mexico Tech. The CREST project is funded by the National Science Foundation Continental Dynamics Program under award EAR-0607693. The facilities of the IRIS Consortium are supported by the National Science Foundation under Cooperative Agreement EAR-0552316, the NSF Office of Polar Programs and the DOE National Nuclear Security Administration. Data from the EarthScope Transportable Array network were made freely available as part of the EarthScope USArray facility supported by the National Science Foundation Major Research Facility program under Cooperative Agreement EAR-0350030.

CHAPTER 4

IMAGING OF THE UPPER MANTLE USING JOINT INVERSION OF TELESEISMIC BODY WAVE AND BOUGUER GRAVITY DATA

Abstract

The simultaneous inversion of datasets with complimentary model sensitivities offers the opportunity to reduce the nonuniqueness common many geophysical inversions. An iterative nonlinear joint inversion methodology is developed for simultaneously inverting teleseismic travel time data and gravity data. An approximate linear slowness–density relationship is derived from Birch's law and is tested using travel time data from the CREST seismic experiment and land–based Bouguer gravity data in the Southern Rocky Mountain region. The method is sensitive to errors in parameter mapping, particularly when respective data sensitivities are highly non-overlapping. Inclusion of short period ambient or ballistic surface wave constraints may improve the method.

4.1 Introduction

The ultimate goal of geophysical inversion is to produce a model of physical parameters that accurately represents geological structure. As many geophysical inversions are ill-posed, additional constraints (regularization) such as smoothness are commonly imposed in order to reduce the non–uniqueness or

improve stability of model solutions, but does so at the expense of introducing an *a priori* bias (Menke, 1989; Parker, 1994). These models, however, may still suffer from the ambiguities inherent in using a single dataset. In teleseismic body wave tomography, for example, source–station geometry generally dictates poor depth resolution due the nearly vertical and parallel model sensitivities of travel time data.

One possible way to alleviate non–uniqueness or poor resolution is to include data constraints from other datasets with complimentary model sensitivities. A "cooperative inversion" (Lines et al., 1988) is an iterative process by which multiple datasets are inverted in sequence. The model solution from one dataset's inversion is projected onto the model space of the next, and used as the starting model for its inversion (Parsons et al., 2001). Alternatively, both datasets can be inverted simultaneously in a "joint inversion" to produce a unified model to explain all data (Lees & Vandecar, 1991; Simmons et al., 2006; Maceira & Ammon, 2009).

Both cooperative and joint approaches require some mapping between model parameter types in order for dissimilar datasets to constrain each other. If the choice of coupling is inaccurate or spatially inconsistent, the joint inversion may be more strongly biased by noise in the mapping than that in the data. Lees & Vandecar (1991) used a linearized relationship between density and seismic velocity to jointly invert Bouguer gravity and local travel time data to produce a unified velocity model beneath western Washington state. In this application, a linear coupling between seismic velocity and density appeared to be appropriate for the short wavelength features investigated. It was found that 90% of the gravity data were explained by a joint velocity model that explained 36.1% of seismic

data, compared to 36.5% for a seismic–only inversion. Maceira & Ammon (2009) applied a nonlinear combination of two velocity–density relationships to jointly invert regional surface wave dispersion data and satellite free air gravity data in central Asia. Short period surface wave arrivals were better predicted by the joint velocity model than the seismic–only model, indicating improvements in the shallow velocity structure from joint inversion.

Another joint inversion approach is one in which the mapping between datasets is parameterized, but not precisely known. In this way, the precise relationship was inverted along with the joint models themselves. Zeyen & Achauer (1997) and Tiberi et al. (2003) performed a nonlinear Bayesian joint inversion of teleseismic travel time and gravity data from the Baikal rift zone for velocity and density above 200 km depth. In this application a depth–dependent linear relationship between velocity and density was assumed and was allowed to vary with depth. It was found that incorporation of Bouguer gravity data provided improved resolution of crustal features, though the results were highly sensitive to gravity data corrections for near–surface features, such as thick sedimentary basins. Tiberi et al. (2008) also applied the method in the Baikal–Mongolia region using lowpass–filtered gravity data, and achieved data RMS reductions of 90% and 43% for gravity and travel time data, respectively. The authors noted a poor correlation between velocity and density models above 100 km depth, despite allowing the relationship between the two datasets to vary, highlighting the strong sensitivity of gravity data to near–surface structure.

In this study, we explore the applicability of joint inversion methodologies to teleseismic body wave travel time and Bouguer gravity datasets. Teleseismic body wave travel times are primarily sensitive to variations in mantle

velocity, with high lateral but poor depth resolution. Bouguer gravity is primarily sensitive to variations in shallow density, also with high lateral but poor depth resolution. The complimentary nature of shallow and deep sensitivities make teleseismic travel time data and Bouguer gravity data an appealing combination for joint inversion. The method presented here departs from previous approaches in that crustal velocity/density variations are not explicitly inverted in the model. Instead crustal corrections from an *a priori* crustal model are applied to both datasets, in order to produce models of mantle heterogeneity.

4.2 Methods

4.2.1 Slowness–density relation

In order to couple velocity and density parameters in a nonlinear simultaneous joint inversion, we test Birch's law, a simple linear relationship (Birch, 1961), (Equation 4.1).

$$v = \beta\rho + c \tag{4.1}$$

In (4.1), v is seismic velocity, ρ is the density, c is a constant, and β is the scaling factor between density and velocity. If density is expressed in units of g/cm^3 and velocity is in m/sec, then $\beta = 3.124\frac{m/sec}{g/cm^3}$ and $c = -2.40$. The inverted parameter in traditional linear seismic tomography is not velocity, but its inverse, slowness. Additionally, both mean–removed travel time and Bouguer gravity data are sensitive to changes in slowness and density, respectively, relative to a background model. It is therefore necessary to recast Birch's law as relationship between velocity and density changes. We first invert and differentiate (4.1):

$$s = (\beta\rho + c)^{-1} \tag{4.2}$$

$$\delta s = -(\beta\rho + c)^{-2}\beta\delta\rho \tag{4.3}$$

Finally we rearrange for density change as a function of slowness change:

$$\delta\rho = -\frac{(\beta\rho + c)^2}{\beta}\delta s = -\frac{v^2}{\beta}\delta s = -\frac{\delta s}{\beta s^2}. \tag{4.4}$$

The relationship in (4.4) is later encoded into the joint inversion equations.

4.2.2 Calculating gravity anomaly

Gravity anomalies at the surface are calculated by summing the contribution of all density changes in the image volume:

$$\delta g = U \sum^{model} \delta\rho D\,, \tag{4.5}$$

where δg is the gravity anomaly vector for m points on the surface, U is the university gravitational constant, and $\delta\rho$ is the density perturbation model. Density elements in the image volume are parameterized as right rectangular prisms. The final term, D, is a volume–distance term for n model elements, measured from m points on the surface, represented by an $m \times n$ matrix. Elements in this term are calculated from the definite discrete integral:

$$D_i = \Big|\Big|\Big| x\ln(y+r) + y\ln(x+r) - z\tan^{-1}\frac{xy}{zr}\Big|_{x_1}^{x_2}\Big|_{y_1}^{y_2}\Big|_{z_1}^{z_2}, \tag{4.6}$$

where and x, y, and z are the cartesian distances from the measurement point, and $r = \sqrt{x^2 + y^2 + z^2}$ (Figure 4.1) (Nagy et al., 2000). A cross section of a gravity kernel calculated for latitude 37, longitude -107 for a model space comprised of blocks $0.25^\circ \times 0.25^\circ \times 25$ km in dimension is shown in Figure 4.2. Sensitivity as technically nonzero in all model parameters, and is visibly sensitive to depths of $\sim$200 km.

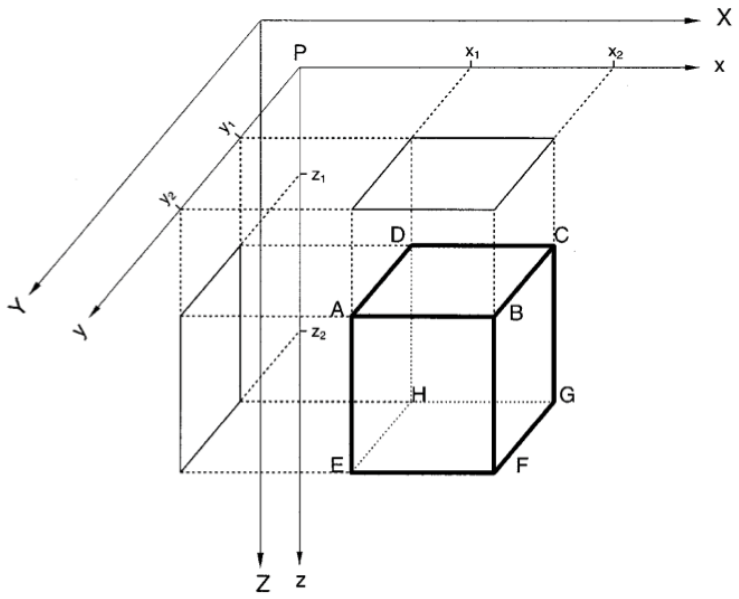

Figure 4.1: Cartesian coordinate representation of a right rectangular prism at vertices ABCDEFGH, measured from point P. From Nagy et al. (2000).

4.2.3 Inversion parameterization

The model space was parameterized by 267,520 constant slowness blocks of $0.25^\circ \times 0.25^\circ$ lateral dimension, and 25 km in depth. An image volume is $21.75^\circ \times 18.75^\circ \times$ 1000 km, much larger than the imaging target was chosen so that features in the joint inversion would not incorrectly constrained to a small volume, and to reduce the likelihood of edge effects from gravity. Teleseismic rays were traced through the image volume, producing a sparse travel time data kernel matrix of ray lengths through each model parameter. We calculated the density sensitivity along a grid of 1672 surface points corresponding to $0.25^\circ \times 0.25^\circ$ pixels of gridded Bouguer data points (Section 4.3.2). This produces a dense gravity kernel matrix of density sensitivities.

In order to accommodate linear and nonlinear relationships between ve-

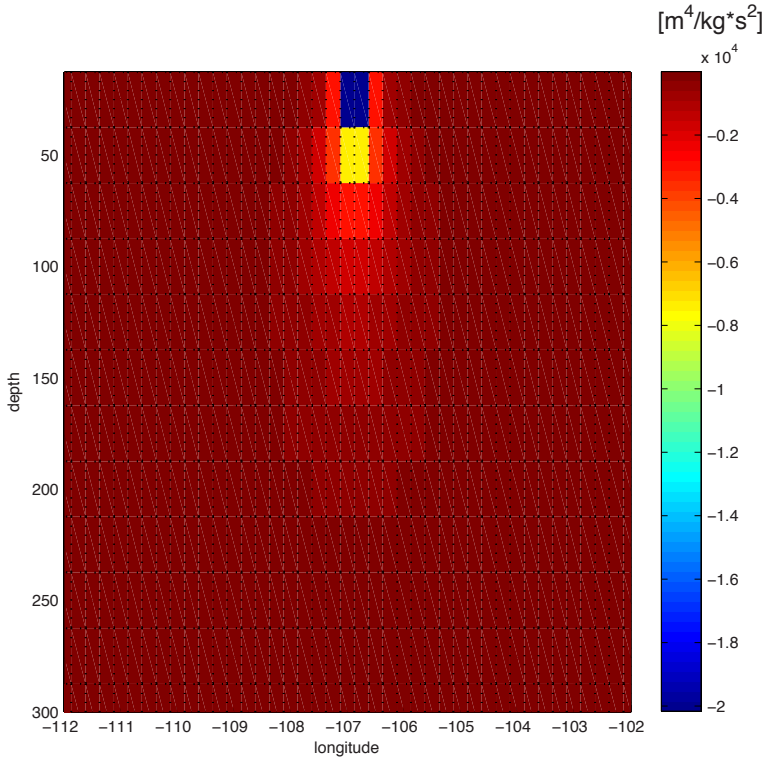

Figure 4.2: Cross section of gravity sensitivity to density (kernel) at latitude 37 calculated from Nagy et al. (2000). Gravity kernels are everywhere nonzero, and visible sensitivity extends to 200 km depth.

locity (slowness) and density, a nonlinear inversion scheme was chosen. The travel time objective function was adopted from MacCarthy et al. (in prep), with the addition of a term representing gravity misfit:

$$\varepsilon = ||\boldsymbol{G_\ell}(\boldsymbol{m}) - \boldsymbol{d_t}||^2 + c\,||\boldsymbol{G_g}(\boldsymbol{m}) - \boldsymbol{d_g}||^2 + \alpha_L\,||\boldsymbol{L_2 m}||^2 + \alpha_m\,||\boldsymbol{m}||^2 + \alpha_D\,||\boldsymbol{Dm}||^2. \tag{4.7}$$

$\boldsymbol{G_\ell}$ is the $m \times n$ ray length matrix, $\boldsymbol{m}$ is $n \times 1$ the model slowness vector, and $\boldsymbol{d_t}$ is the $m \times 1$ crust corrected travel time vector. $\boldsymbol{G_g}$ is the gravity forward operator, which is a combination of (4.4), (4.5), and (4.6),

$$\boldsymbol{G_g}(\boldsymbol{m^k}) = -\frac{UD}{\beta s^2}\boldsymbol{m^k} = \delta g, \tag{4.8}$$

and c is weighting parameter that adjusts the relative influence of the gravity data relative to travel time data. $\boldsymbol{d_g}$ is the $p \times 1$ gravity data vector. Equations in the first and second terms are divided by each datum's estimated standard error. The third term represents model smoothing, the fourth is norm damping, and last term is edge damping, each weighted by corresponding regularization weighting parameters, $\alpha_{L,m,D}$. $\boldsymbol{L_2}$ is a second–difference (Laplacian) roughening matrix, and $\boldsymbol{D}$ is a matrix that damps one layer on the top of the model and three layers on the sides and bottom. α_L and α_m are the preferred smoothing and damping parameters from independent inversions of the travel time data (MacCarthy et al., in prep).

The regularized inversion scheme that we've chosen is the Gauss–Newton method, an iterative nonlinear least squares algorithm. In this method, a starting model is chosen, m^0, and a model step, δm, is calculated using the Gauss–Newton equations for a regularized inversion (Aster et al., 2005):

$$\begin{aligned}&[(J(m^k)^T J(m^k) + \alpha_L L_2^T L_2 + \alpha_m I^T I + \alpha_D D^T D]\delta m = \\ &-J(m^k)^T[G(m^k) - d] - \alpha_L L_2^T L_2 + \alpha_m I^T I + \alpha_D D^T D\end{aligned} \tag{4.9}$$

Here, $G(m^k)$ is a compound forward operator on the k^{th} model, $J(m^k)$ is a compound Jacobian matrix, and d is a compound data vector:

$$G(m^k) = \begin{bmatrix} G_\ell(m^k) \\ G_g(m^k) \end{bmatrix} = \begin{bmatrix} G_\ell m^k \\ -\frac{UD}{\beta s^2} m^k \end{bmatrix}, \tag{4.10}$$

$$J(m^k) = \begin{bmatrix} J_\ell(m^k) \\ J_g(m^k) \end{bmatrix} = \begin{bmatrix} G_\ell \\ -\frac{UD}{\beta s^2} \end{bmatrix}, \tag{4.11}$$

$$d = \begin{bmatrix} d_t \\ d_g \end{bmatrix}. \tag{4.12}$$

The model step can be solved with LSQR (PAIGE & SAUNDERS, 1982). The model and Jacobians are then updated and (4.9) is solved again. This is repeated until acceptable convergence.

4.2.4 Synthetic nonlinear inversions

To test the fidelity of the nonlinear inversion method, two synthetic tests were performed. First, a known velocity (slowness) model was used to generate synthetic travel time data using the seismic data kernel matrix. The input model was a checkerboard of alternating 3^3 block clusters of $\pm 2\%$ velocity variation from ak135. Noise identical to that estimated for the measured P residuals was added to the synthetic data, and a single step of the Gauss–Newton method was performed using only the synthetic P residuals. This inversion is identical to the single–step seismic–only checkerboard inversion performed by MacCarthy et al. (in prep). The inverted models and associated variance reductions were found to be indistinguishable.

We also test the theoretical change in model resolution afforded by the joint inversion, under the assumption that Birch's law is strictly true. The same input model as above was used to produce synthetic gravity data, which then

contaminated with normally distributed noise with a standard deviation of 1 milligal (mGal). The two synthetic datasets where then jointly inverted. In this inversion, c was chosen to give equal initial weight between the seismic and gravity data. Jointly inverted solutions converged quickly after three Gauss–Newton outer iterations and 200 LSQR inner iterations. An identical inversion was performed using seismic data only, and the two inverted models were compared (Figures 4.3 and 4.4).

Under strict adherence to the slowness–density relation, the joint inversion provides additional feature recovery particularly in the shallow regions of the model. Above 200 km depth, both amplitude and shape recovery were improved by the inclusion of gravity data constraints. Additionally, shape recovery is improved in regions that are poorly sampled by seismic rays, such as depths above $\sim$300 km in cross sections 1 and 6 (Figures 4.3 and4.4), and the outer longitudes of most cross sections. This result is promising, but somewhat expected, in that the strict coupling between seismic and gravity measurements effectively transforms gravity stations into pseudo seismic stations. They each record the same velocity structure nearly perfectly, within their respective sensitivities. The following section extends the joint inversion methodology to real seismic and gravity data from the Southern Rocky Mountains, and tests the validity of the linear assumption.

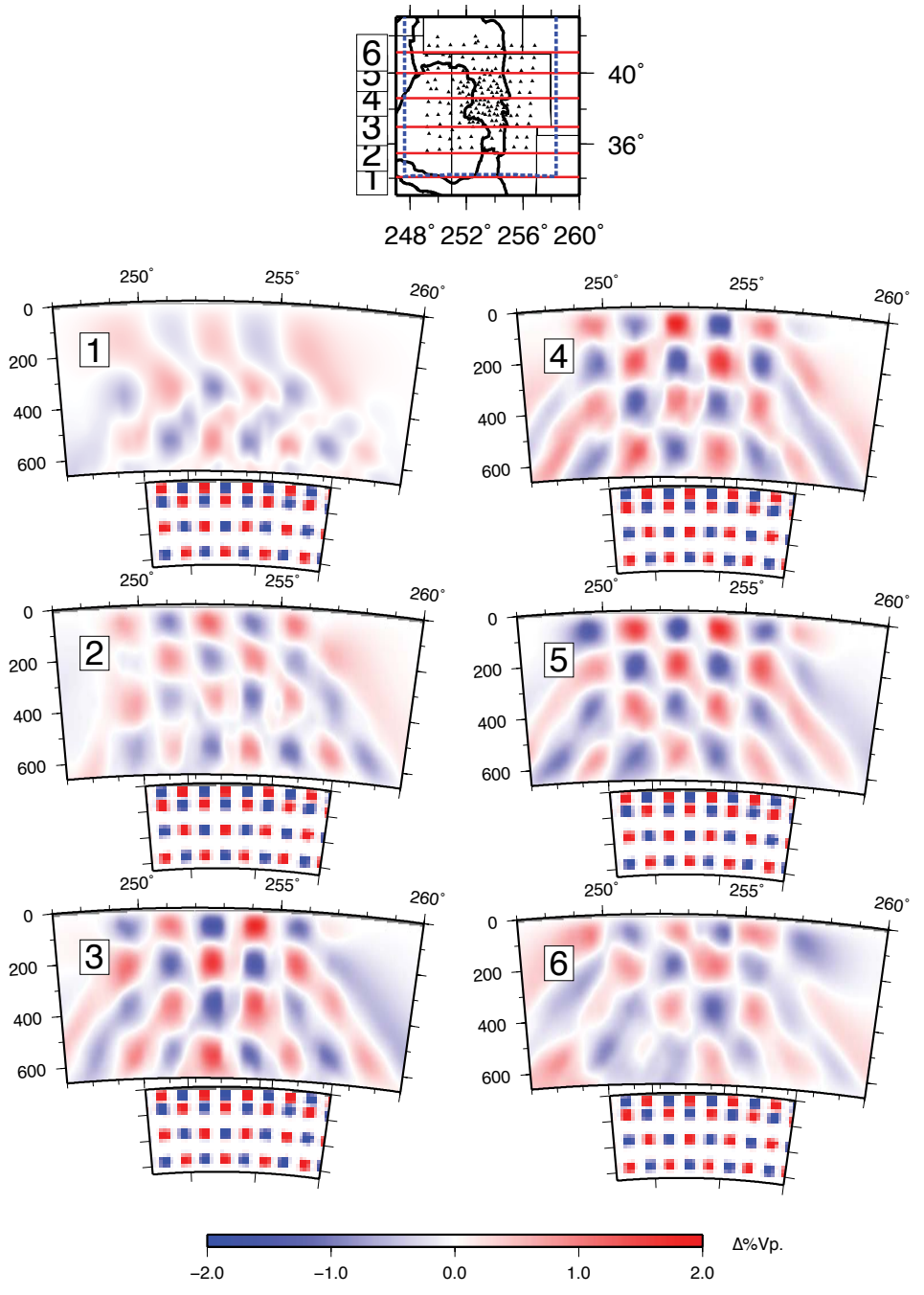

Figure 4.3: Checkerboard resolution test using only seismic data. Key: Labeled latitude slices are red lines. Seismic stations are small black triangles. The area containing Bouguer gravity data is outlined in dashed blue. Cross sections: Latitude slices through the recovered velocity model (top), and input checkerboard model (bottom).

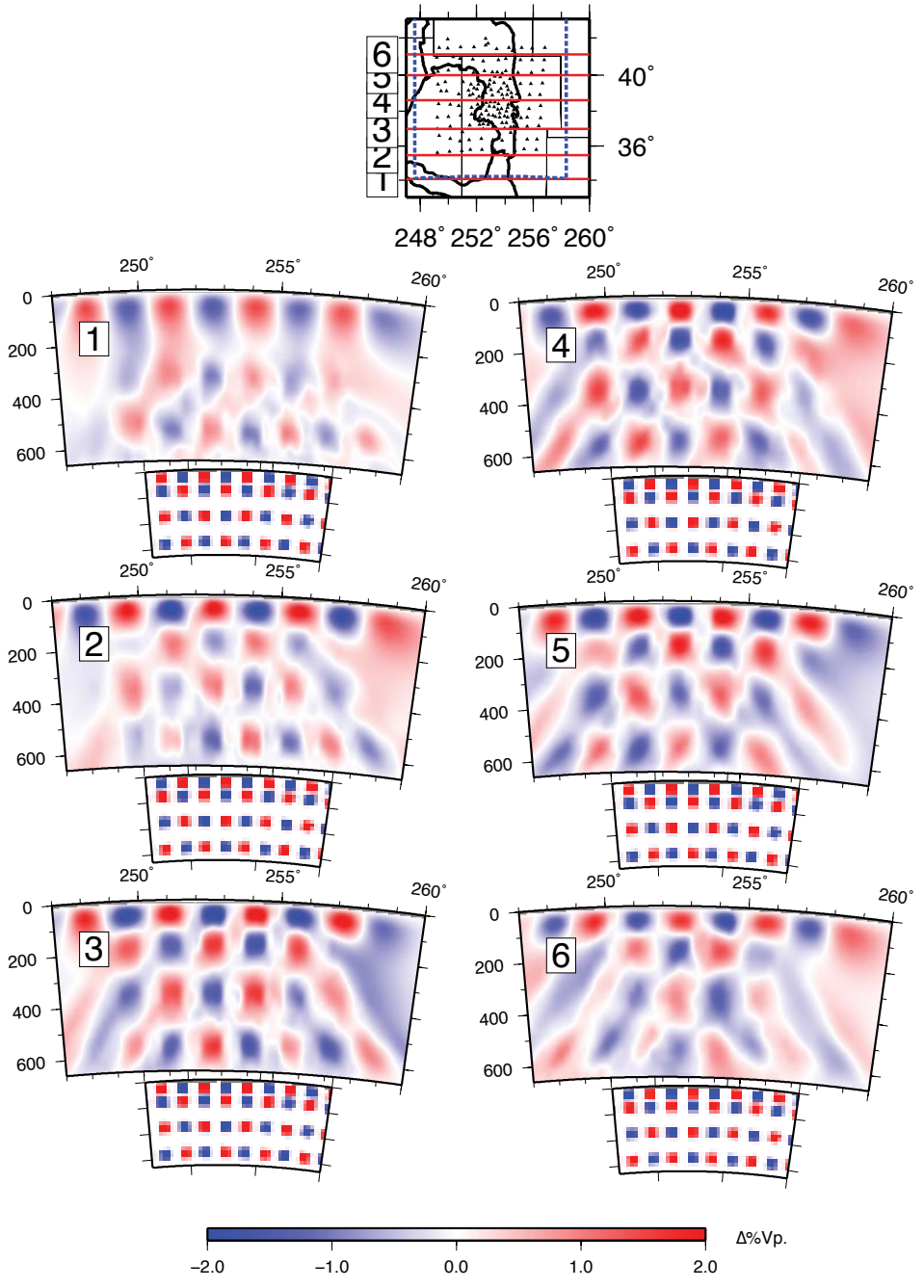

Figure 4.4: Checkerboard resolution test using seismic and gravity data.

4.3 Application to the Southern Rocky Mountains

4.3.1 Teleseismic travel times

Broadband seismic data from the CREST (Colorado Rockies Experiment and Seismic Transects) experiment (Aster et al., 2009; MacCarthy et al., in prep) and USArray network facility (Meltzer et al., 1999) were used to measure teleseismic P wave travel time residuals the the Southern Rocky Mountains (SRM) of Colorado. The primary goal of the CREST seismic experiment was to provide constraints on the structure and state of the upper mantle beneath the SRM. A complete description of seismic sources and data measurement is given in MacCarthy et al. (in prep); only a brief summary is provided here. The CREST seismic network was comprised of 59 broadband stations operating for 14 months, from July 2008 to October 2009, synchronously with 101 stations the USArray facility in Colorado and several other permanent broadband stations. The combined network of 167 stations spans portions of the Colorado Plateau (CP), Southern Rocky Mountains (SRM), Rio Grande Rift (RGR), and Great Plains (GP) physiographic provinces (Figure 4.5), with an aperture of $\sim$300 km and a mean station spacing of 23 km in the core CREST footprint.

Approximately 14,690 crosscorrelation derived P wave travel time residuals and estimated errors were measured from 183 teleseismic earthquakes. Raypaths were calculated by geometric raytracing through the 1D reference velocity model ak135 (Kennett et al., 1995). Residuals were corrected for travel time variations in the crust relative to the background velocity model caused by variations in crustal thickness and velocity. Finally, residuals from each event were demeaned so that inverted velocity models represent zero–mean velocity variations inside the image volume.

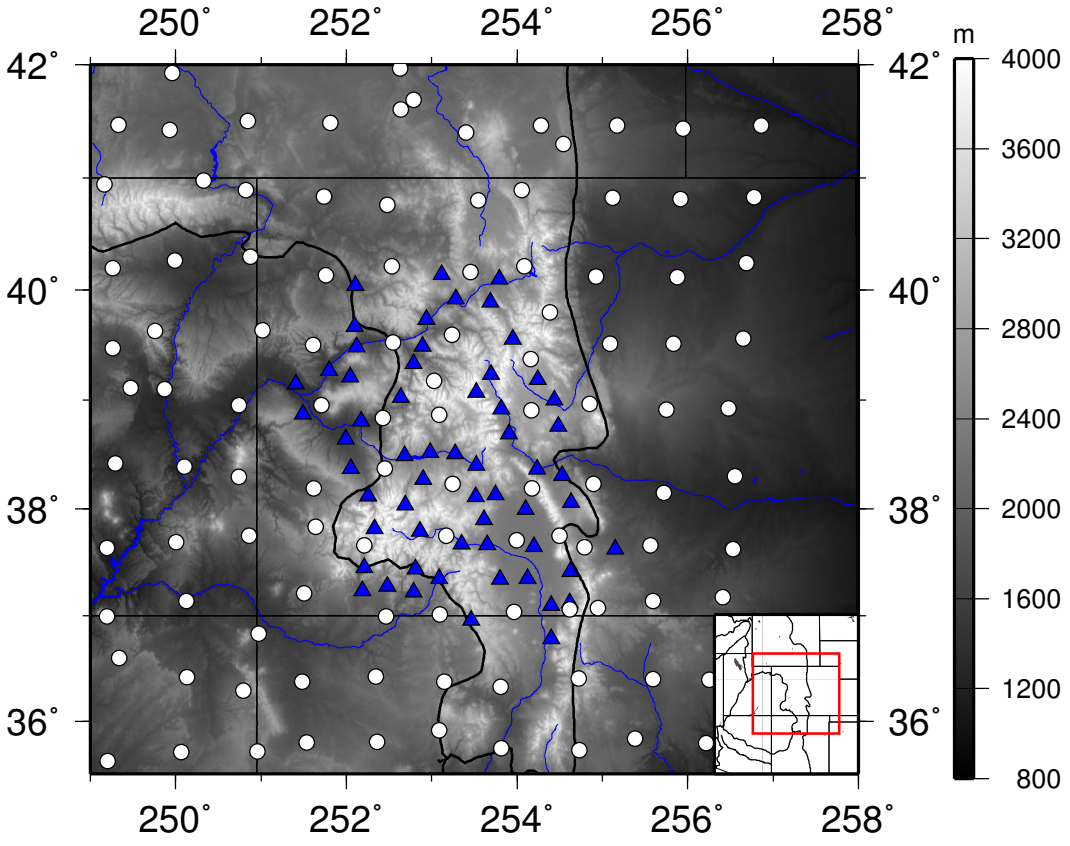

Figure 4.5: Location of CREST stations (blue triangles) and USArray stations (white circles). Physiographic provinces are outlined. Inset: the study area is outlined in red.

4.3.2 Bouguer gravity

Over 143,000 land–based Bouguer point data were downloaded from the Pan American Center for Environmental Studies (PACES) geophysical database (Figure 4.6) and gridded to $0.25^\circ \times 0.25^\circ$. A planar trend, representing a regional anomaly beyond the resolution of the inversion, was removed. The high–frequency components of the gravity field are below the resolution of teleseismic data, and were presumably removed from the travel time residuals during crustal correction. Gravity data were thus lowpass filtered at several corner frequencies, and the lowpassed data were correlated with mean uppermost mantle velocities ($<$100km depth) from the linear V_p inversion of MacCarthy et al. (in prep), in order to determine an appropriate spatial wavelength, c, above which gravity data may reflect changes in mantle density structure. It was found that the detrended, unfiltered data had the highest correlation, at 0.43. We suspect that this is due to several factors. Crest lateral resolution is 50–75 km, and some shallow structures resolved by gravity data may also be resolved by seismic data at these wavelengths. Therefore, lowpass filtering gravity data $>$50–75 km may impair the correlation. Also, laterally continuous shallow features in the gravity field, such as large basins or adjacent low density plutons, will remain in the lowpassed data. If these features such as these aren't underlain by low velocity mantle, than the correlation at large λ_k may also be impaired. Finally, the gridding of gravity data to $0.25^\circ \times 0.25^\circ$ pixels is a lowpass filter itself, and the highest frequency, least likely to correlate features may have already been removed from the gravity field.

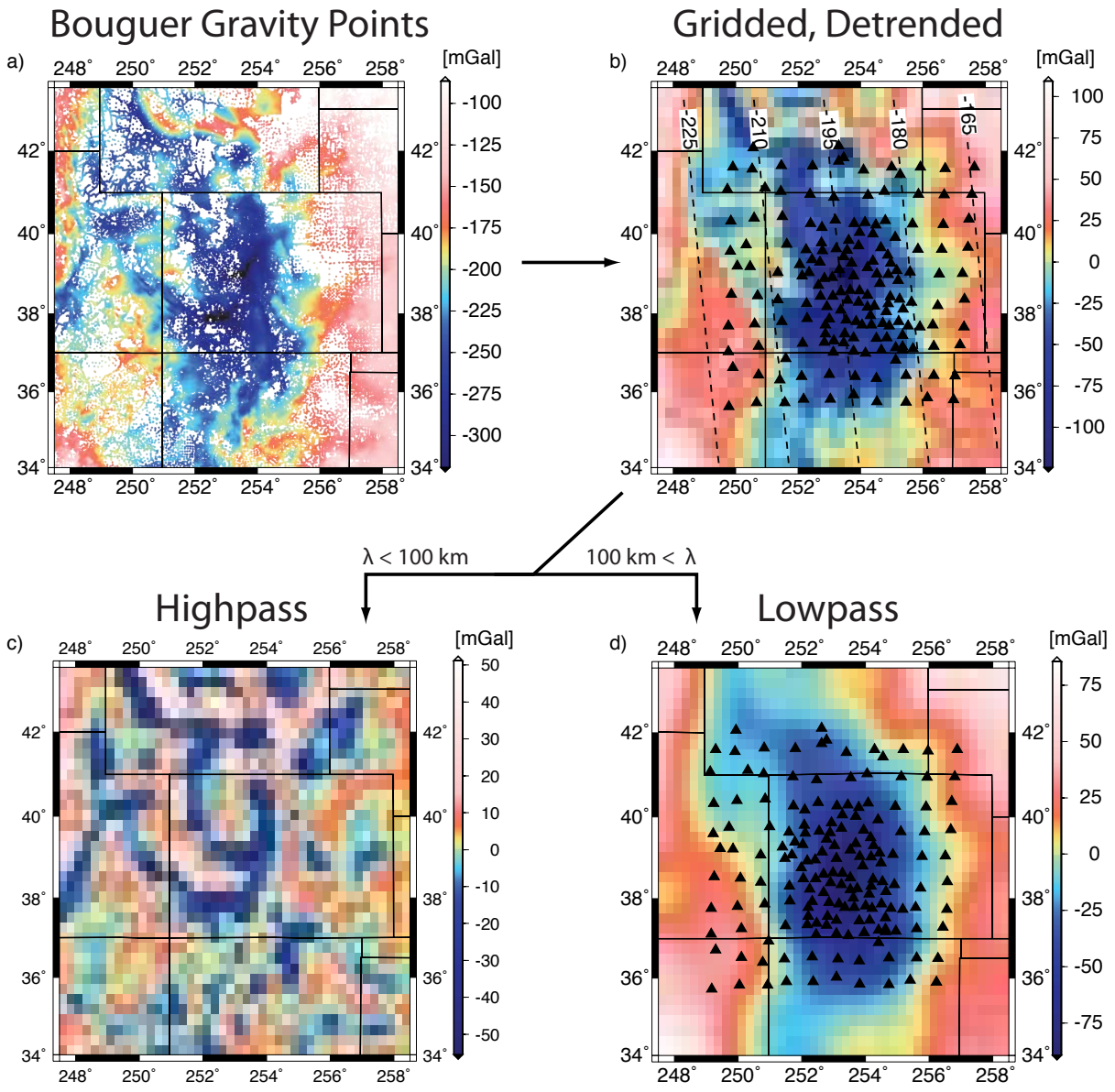

Figure 4.6: Land-based Bouguer point data were downloaded from the PACES geophysical database (a), gridded at $0.25^\circ \times 0.25^\circ$, and detrended (b). In (b), the removed trend is also shown. Example filtered data, λ_k = 100 km, are shown in (c),(d).

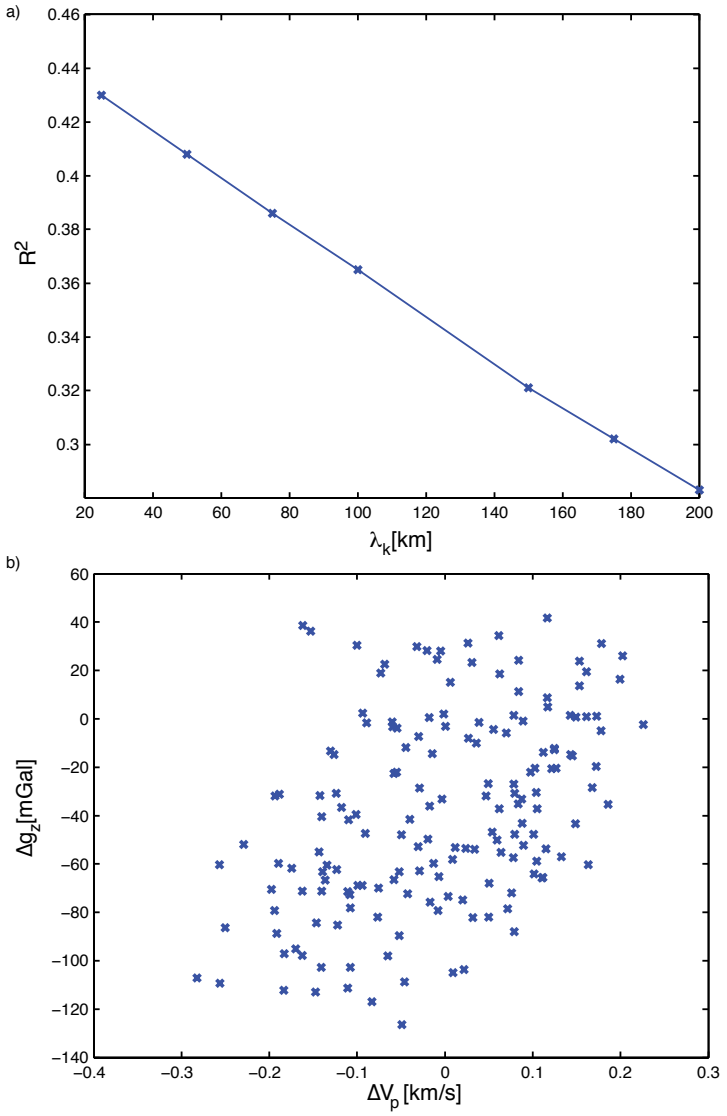

Figure 4.7: a) Gravity lowpass filter cutoff (λ_k) versus correlation coefficient with mean velocity–only perturbation above 100 km depth. The highest correlation is for unfiltered, detrended data (b).

4.3.3 Results

Body wave P residuals and gridded, detrended Bouguer gravity were jointly inverted using the methodology described above. Relative gravity data weights, c, between 0 and 2 were explored. Figures 4.8 and 4.9 illustrate models that are typical of the images produced through joint inversion, and represent equal initial scaling between the datasets. Each model slice is paired with its corresponding seismic–only inverted model slice, for comparison. The two most clear differences in the joint models compared to the seismic–only models is the general slowing of the uppermost mantle beneath Colorado ($<$ 100–150 km) and a pronounced anticorrelation between velocities at these depths and those deeper in the upper mantle. The gridded and detrended gravity field (Figure 4.6b) has a profound low anomaly feature in central Colorado. These are some of the lowest Bouguer gravity values in North America, and are thought to due to a combination of low–density volcanic piles, granitic crustal batholiths, and low–density upper mantle (McCoy et al., 2004). While there is reason to believe that the current state of the mantle lithosphere may be hot, partially molten, or otherwise low density (Lee & Grand, 1996; McMillan et al., 2006; Eaton, 2008; MacCarthy et al., in prep), the extensive lithospheric low velocities in the joint model overprint geologically reasonable high velocities in the northern Colorado Plateau and western Great Plains imaged by other experiments (Dueker & Yuan, 2004; Schmandt & Humphreys, 2010; Obrebski et al., 2010).

Perhaps more strikingly, broad high velocity regions underlie most of the SRM subcontinental lithosphere below 200–300 km depth. Similar regions in the mantle transition zone beneath the western US have been imaged in recent wide–aperture seismic experiments (Schmandt & Humphreys, 2010; Obrebski et al.,

2010), but these high velocities are contained within the transition zone, and low velocities are seen beneath the SRM above the transition zone. For these reasons, as well as the unreasonable geodynamic implications of such broad very low density upper mantle, we feel that laterally extensive crustal low densities in the gravity dataset are being incorrectly mapped into low velocity uppermost mantle during the inversion. As a result, the inversion is attempting to maintain fit to the travel time dataset by compensating in the subcontinental lithosphere with broad high velocities. Interestingly, the jointly inverted model retains high variance reductions for both travel time and gravity data. Seismic data variance reductions remain near 70-75% with and without inclusion of gravity data. Bouguer gravity is highly nonunique, so independently inverted density models from the SRM gravity dataset have variance reductions of $\sim$95%. Jointly inverted, the gravity dataset variance reduction is $\sim$83%.

4.4 Conclusions

We present a flexible nonlinear method to simultaneously invert body wave travel time and gravity data for velocity structure of the upper mantle. The technique employs a linear relationship between slowness and density changes in the upper mantle, though the nonlinear framework make the approach adaptable for nonlinear parameter mappings and other complimentary datasets. The method was applied to teleseismic travel time residuals and Bouguer gravity data in Colorado, and it was found to be strongly sensitive to laterally extensive shallow crustal features. The inversion introduced significant artifacts into the model,

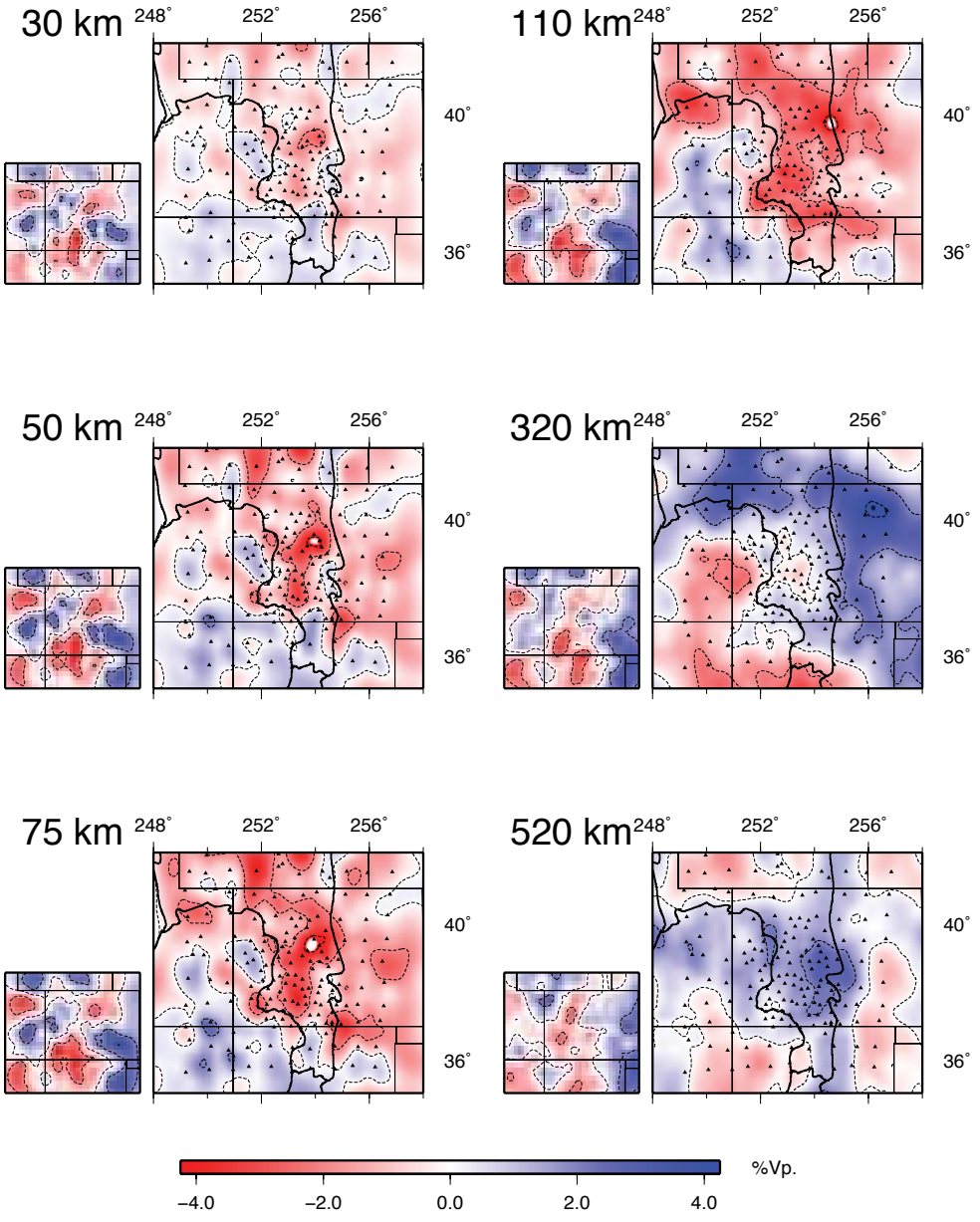

Figure 4.8: Joint inversion results for Southern Rocky Mountains. Depth slices showing jointly inverted velocity variations (large tiles), and seismic–only velocity model (small tiles).

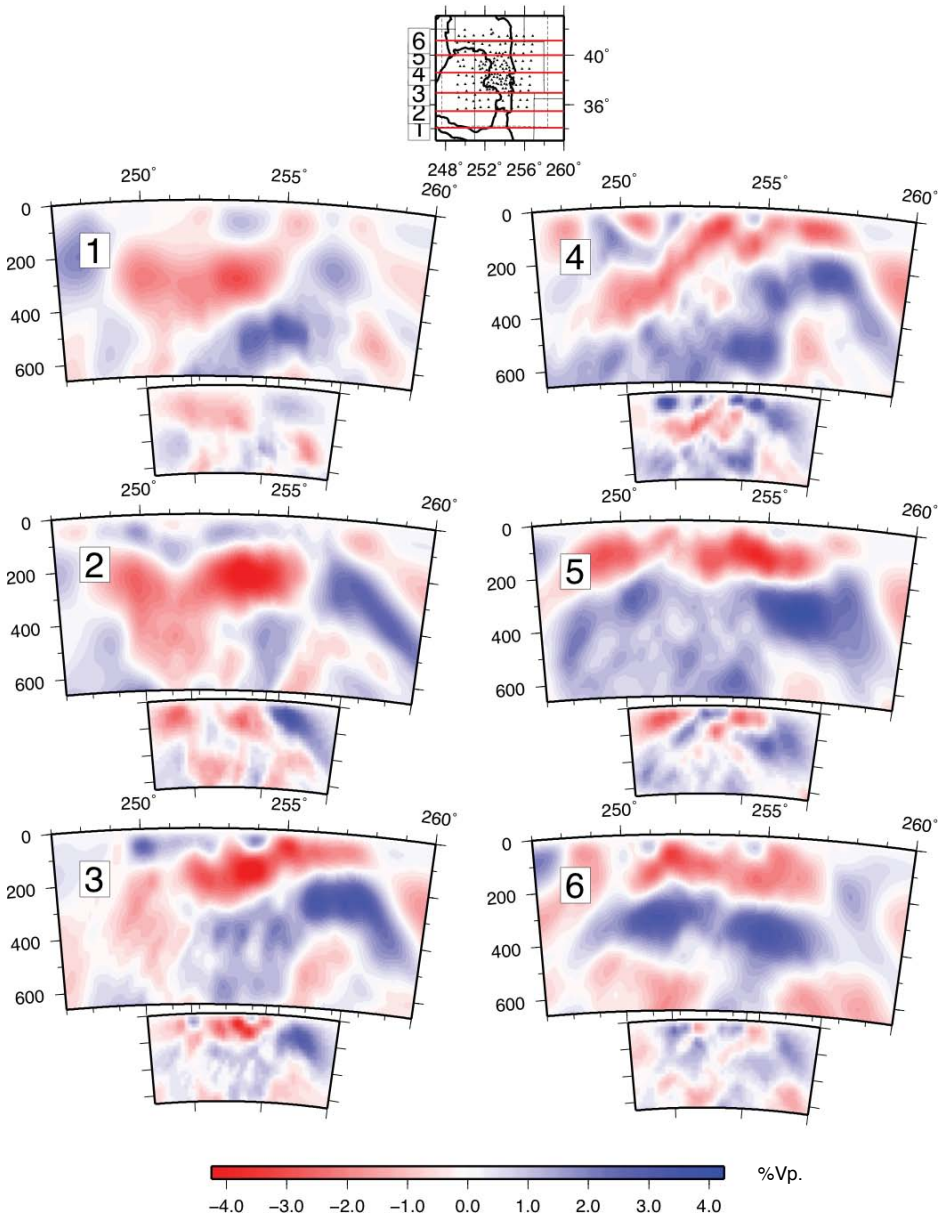

Figure 4.9: Joint inversion results for Southern Rocky Mountains. Key: showing cross sections (red lines), political and physiographic boundaries (solid black lines), seismic stations (small triangles), and extent of gravity data coverage (dashed line). Large tiles are jointly inverted V_p models, and small tiles are the corresponding seismic–only V_p models.

though still explaining both datasets to a high degree. Two possible solutions are analogous to those used in traditional travel time tomography. The first is the use of a "station term" in the inversion. This is a damped parameter used primarily to absorb any unexplained misfit between data and model. A station term may partially absorb unexplained structure in the mantle due to velocity anisotropy, incorrect or spatially varying parameter mapping, or incompatible data sensitivities. As this term may absorb true structure, it must be monitored carefully.

A second solution is a gravity "crustal correction", similar to that used in teleseismic tomography. This was the approach taken by Zeyen & Achauer (1997) for sedimentary basins and bodies of water. Predicted gravity effects from near surface structures were removed from the gravity data. A more extensive correction may be applied through the increasingly common Ambient Noise Tomography (ANT) technique (Shapiro et al., 2005), whereby high resolution 3D crustal shear velocity structure is derived from ambient noise sources (not earthquakes). If the gravity field is well correlated to ANT crustal velocities, than a mapping of crustal velocities to crustal densities provides the gravity crustal correction. For example, in Colorado, CREST ANT upper and middle crustal shear velocities (Stachnik, pers. comm.) show a remarkable correlation to Bouguer gravity lows (Figure 4.10). In the case of joint inversions using travel time data, this approach has the advantage of leveraging already existing seismic data, and without the need for high signal to noise local, regional, or teleseismic natural sources. It may ultimately be most advantageous, however, to include ANT dispersion data in the joint inversion.

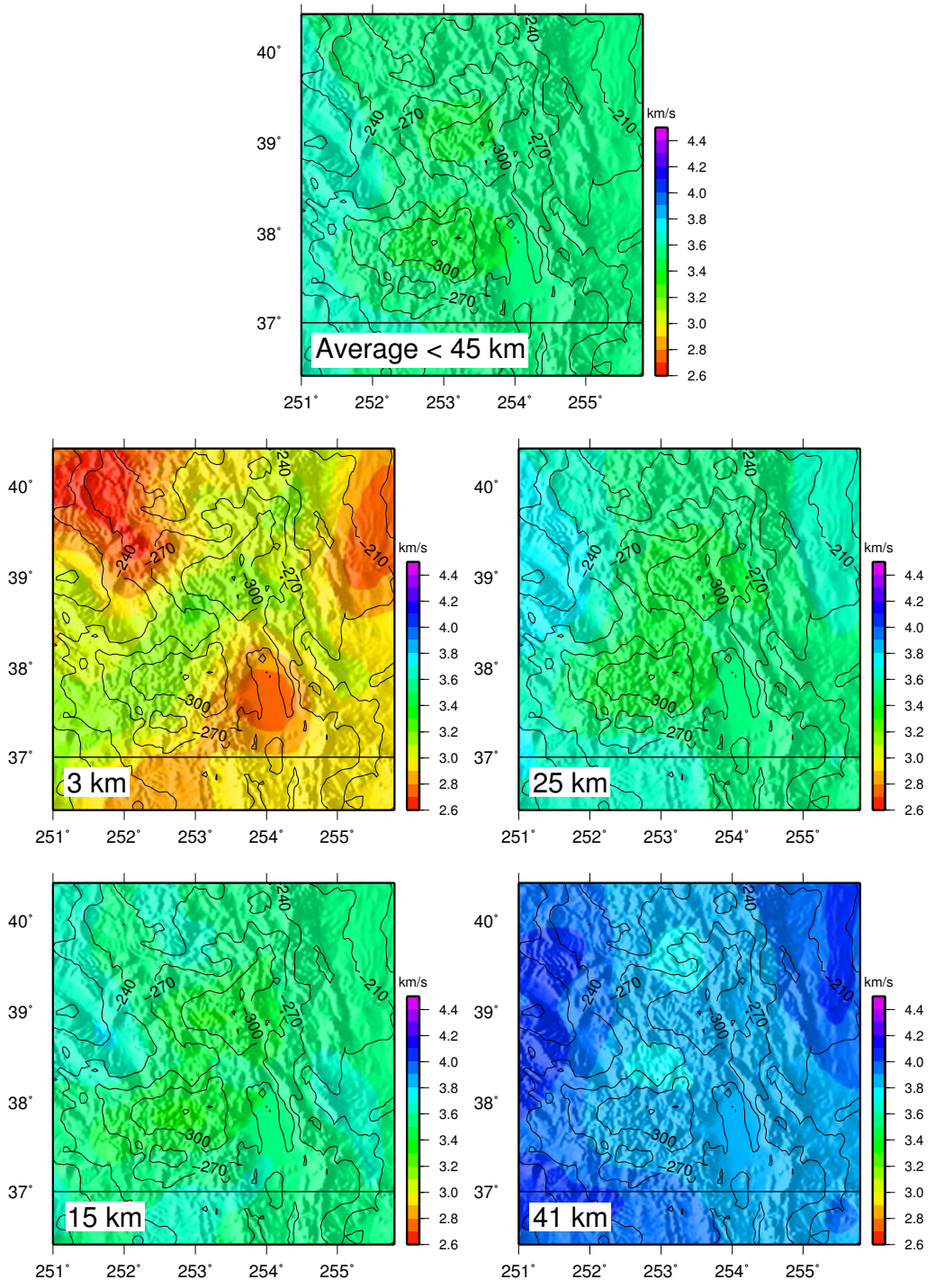

Figure 4.10: Depths slices of crustal V_s (colored) from CREST ambient noise tomography (ANT) in southwestern Colorado. Bouguer gravity contours are overlaid.

REFERENCES

Afonso, J. C., Ranalli, G., Fernàndez, M., Griffin, W. L., O'Reilly, S. Y., & Faul, U. (2010). On the Vp/Vs-Mg# correlation in mantle peridotites: Implications for the identification of thermal and compositional anomalies in the upper mantle. *Earth and Planetary Science Letters*, *289*(3-4), 606–618.

Allen, R. M., Nolet, G., Morgan, W. J., Vogfjörd, K., Bergsson, B. H., Erlendsson, P., Foulger, G. R., Jakobsdóttir, S., Julian, B. R., Pritchard, M., Ragnarsson, S., & Stefánsson, R. (2002). Imaging the mantle beneath Iceland using integrated seismological techniques. *Journal of Geophysical Research (Solid Earth)*, *107*(10.1029), 2325–+.

Aster, R., MacCarthy, J., Heizler, M., Kelley, S., Karlstrom, K., Crossey, L., Dueker, K., & the CREST Team (2009). CREST experiment probes the roots and geologic history of the colorado rockies. *Outcrop*, *58*(1), 6–21.

Aster, R. C., Rowe, C., & Taylor, S. R. (2005). Retroactive and real-time automatic discrimination and classification of seismic event types using multiple classification schemes and higher-order signal processing. Proposal, New Mexico Institute of Mining and Technology.

Bassin, C., Laske, G., & Masters, G. (2000). The current limits of resolution for surface wave tomography in North America. *Eos Trans AGU*, *81*, F897.

Bekas, C., Kokiopoulou, E., & Saad, Y. (2007). An estimator for the diagonal of a matrix. *Applied numerical mathematics*, *57*(11-12), 1214–1229.

Bennett, V., & Depaulo, D. (1987). Proterozoic crustal history of the western United States as determined by neodymium isotopic mapping. *Bulletin of the Geological Society of America*, *99*(5), 674.

Berryman, J. (2000). Analysis of approximate inverses in tomography ii. iterative inverses. *Optimization and Engineering*, *1*(4), 437–473.

Birch, F. (1961). The velocity of compressional waves in rocks to 10 kilobars, part 2. *Journal of Geophysical Research*, *66*(7), 2199–2224.

Bird, P. (1984). Laramide crustal thickening event in the Rocky Mountain foreland and Great Plains. *Tectonics*, *3*(7), 741–758.

Boschi, L. (2003). Measures of resolution in global body wave tomography. *GEOPHYSICAL RESEARCH LETTERS*, *30*(19), 1978.

Boyd, O., & Sheehan, A. F. (2005). Attenuation tomography beneath the rocky mountain front: Implications for the physical state of the upper mantle. In G. R. K. K Karlstrom (Ed.) *The Rocky Mountain Region: An Evolving Lithosphere Tectonics, Geochemistry, and Geophysics*, vol. 154 of *Geophysical Monograph Series*, (p. 482). AMER GEOPHYSICAL UNION.

Burdick, S., van der Hilst, R., Vernon, F., Martynov, V., Cox, T., Eakins, J., Mulder, T., Astiz, L., & Pavlis, G. (2009). Model Update December 2008: Upper Mantle Heterogeneity beneath North America from P-wave Travel Time Tomography with Global and USArray Transportable Array Data. *Seismological Research Letters*, *80*(4), 638.

Cammarano, F., Goes, S., Vacher, P., & Giardini, D. (2003). Inferring upper-mantle temperatures from seismic velocities. *PHYSICS OF THE EARTH AND PLANETARY INTERIORS*, *138*(3-4), 197–222.

Condie, K. C., & Selverstone, J. (1999). The crust of the colorado plateau: New views of an old arc. *Journal of Geology*, *107*(4), 387 – 397.

Condie, K. C., & Shadel, C. A. (1984). An early proterozoic arc succession in southeastern wyoming. *Canadian Journal of Earth Sciences*, *21*, 415–427.

Coney, P., & Reynolds, S. (1977). Cordilleran Benioff zones. *Nature*, *270*, 403–406.

Craven, P., & Wahba, G. (1979). Smoothing noisy data with spline functions. *Numerische Mathematik*, *31*, 377–403.

Crosswhite, J., & Humphreys, E. (2003). Imaging the mountainless root of the 1.8 Ga Cheyenne belt suture and clues to its tectonic stability. *Geology*, *31*(8), 669.

Crotwell, H., & Owens, T. (2005). Automated receiver function processing. *Seismological Research Letters*, *76*(6), 702.

Deal, M., & Nolet, G. (1996). Comment on'estimation of resolution and covariance for large matrix inversions' by j. zhang and ga mcmechan. *Geophysical Journal International*, *127*(1), 245–250.

Dixon, J., Dixon, T., Bell, D., & Malservisi, R. (2004). Lateral variation in upper mantle viscosity: role of water. *Earth and Planetary Science Letters*, *222*(2), 451–467.

Dueker, K., & Sheehan, A. (1998). Mantle discontinuity structure beneath the Colorado Rocky Mountains and High Plains. *Journal of Geophysical Research (Solid Earth)*, *103*(B4), 7153–7169.

Dueker, K., & Yuan, H. (2004). Upper mantle P-wave velocity structure from PASSCAL teleseismic transects across Idaho, Wyoming and Colorado. *Geophysical Research Letters*, *31*(8), 8603–+.

Dueker, K., Yuan, H., & Zurek, B. (2001). Thick-structured Proterozoic lithosphere of the Rocky Mountain region. *GSA Today*, *11*(12), 4–9.

Dziewonski, A., & Anderson, D. (1983). Travel times and station corrections for P waves at teleseismic distances. *J. geophys. Res*, *88*(B4), 3295–3314.

Eaton, G. P. (2008). Epeirogeny in the southern rocky mountains region: Evidence and origin. *GEOSPHERE*, *4*(5), 764–784.

Elder, W., & Kirkland, J. (1994). Cretaceous paleogeography of the southern Western Interior region. In *Mesozoic systems of the Rocky Mountain region, USA*, (pp. 415–456). SEPM (Society for Sedimentary Geology) Rocky Mountain Section.

English, J. M., Johnston, S. T., & Wang, K. (2003). Thermal modelling of the laramide orogeny: testing the flat-slab subduction hypothesis. *Earth and Planetary Science Letters*, *214*(3-4), 619–632.
URL http://www.sciencedirect.com/science/article/B6V61-49CT12P-3/2/202e230cb

Farmer, G. L., Bailley, T., & Elkins-Tanton, L. T. (2008). Mantle source volumes and the origin of the mid-tertiary ignimbrite flare-up in the southern rocky mountains, western us. *LITHOS*, *102*(1-2), 279–294.

Gao, W., Grand, S. P., Baldridge, W. S., Wilson, D., West, M., Ni, J. F., & Aster, R. (2004). Upper mantle convection beneath the central rio grande rift imaged by p and s wave tomography. *Journal of Geophysical Research-Solid Earth*, *109*(B3), B03305. Article 0148-0227 Times Cited:9 Bibliography:70 English JGREA2 000220439500003 Copyright 2007 The Thomson Corporation.

Gao, W., Matzel, E., & Grand, S. (2006). Upper mantle seismic structure beneath eastern Mexico determined from P and S waveform inversion and its implications. *Journal of Geophysical Research*, *111*(B8), B08307.

Gilbert, H. J., & Sheehan, A. F. (2004). Images of crustal variations in the intermountain west. *JOURNAL OF GEOPHYSICAL RESEARCH-SOLID EARTH*, *109*(B3), B03306 –.
URL http://linkseeker.lanl.gov/nmt?url$_ver$ = $Z39.88-2004ctx_ver$ = $Z39.88-2004ctx_enc = info:ofi/enc:UTF-8rft_val_fmt = info:ofi/fmt:kev:mtx:journalrft.genre = articlerft.issn = 0148-0227rft.coden = JGREA2rft.date = 2004rft.volume = 109rft.issue = b3rft.spage = b03306rft.atitle = Images + of + crustal + variations + in + the + intermountain + westrft.jtitle = JOURNAL + OF + GEOPHYSICAL + RESEARCHD + EARTHrft.aulast = Gilbertrft.auinit = HJrft.pub = AMER + GEOPHYSICAL + UNIONrft_id = info : lanl - repo/isi/$000220439700003

Girard, D. (1987). Un algorithme simple et rapide pour la validation croisée généralisée sur des problèmes de grande taille. *RR 669-M, Grenoble, France: Informatique et Mathématiques Appliquées de Grenoble*.

Godey, S., Deschamps, F., Trampert, J., & Snieder, R. (2004). Thermal and compositional anomalies beneath the north american continent. *JOURNAL OF GEOPHYSICAL RESEARCH-SOLID EARTH*, *109*(B1), B01308.

Goes, S., Govers, R., & Vacher, P. (2000). Shallow mantle temperatures under europe from p and s wave tomography. *J. Geophys. Res.*, *105*(B5), 11153–11169.
URL http://dx.doi.org/10.1029/1999JB900300

Goes, S., & van der Lee, S. (2002). Thermal structure of the north american uppermost mantle inferred from seismic tomography - art. no. 2050. *JOURNAL OF GEOPHYSICAL RESEARCH-SOLID EARTH*, *107*(B3), 2050 – 2050.
URL http://linkseeker.lanl.gov/nmt?url$_v$er = Z39.88 − 2004ctx_ver = Z39.88 − 2004ctx_enc = $info$: ofi/enc : $UTF-8rft_val_fmt$ = $info$: ofi/fmt : kev : mtx : $journalrft.genre$ = $articlerft.issn$ = 0148 − 0227$rft.coden$ = $JGREA2rft.date$ = 2002$rft.volume$ = 107$rft.issue$ = $b3rft.spage$ = 2050$rft.epage$ = 2050$rft.atitle$ = $Thermal + structure + of + the + North + American + uppermost + mantle + inferred + +Hrft.aulast$ = $Goesrft.auinit$ = $Srft.pub$ = $AMER + GEOPHYSICAL + UNIONrft_id$ = $info : lanl - repo/isi/$000178909900008

Golub, G., Heath, M., & Wahba, G. (1979). Generalized cross-validation as a method for choosing a good ridge parameter. *Technometrics*, *21*(2), 215–223.

Golub, G. H., & vonMatt, U. (1997). Generalized cross-validation for large-scale problems. *JOURNAL OF COMPUTATIONAL AND GRAPHICAL STATISTICS*, *6*(1), 1–34.

Hammond, W., & Toomey, D. (2003). Seismic velocity anisotropy and heterogeneity beneath the Mantle Electromagnetic and Tomography Experiment (MELT) region of the East Pacific Rise from analysis of P and S body waves. *JOURNAL OF GEOPHYSICAL RESEARCH-SOLID EARTH*, *108*(B4).

Hammond, W. C., & Humphreys, E. D. (2000). Upper mantle seismic wave attenuation: Effects of realistic partial melt distribution. *JOURNAL OF GEOPHYSICAL RESEARCH-SOLID EARTH*, *105*(B5), 10987 – 10999.
URL http://linkseeker.lanl.gov/nmt?url$_v$er = Z39.88 − 2004ctx_ver = Z39.88 − 2004ctx_enc = $info : ofi/enc : UTF-8rft_val_fmt = info : ofi/fmt : kev$: mtx : $journalrft.genre$ = $articlerft.issn$ = 0148 − 0227$rft.coden$ = $JGREA2rft.date$ = 2000$rft.volume$ = 105$rft.issue$ = $b5rft.spage$ = 10987$rft.epage$ = 10999$rft.atitle$ = $Upper + mantle + seismic + wave + attenuationrft.jtitle = JOURNAL + OF + GEOPHYSICAL + RESEARCHHft.auinit = WCrft.pub = AMER + GEOPHYSICAL + UNIONrft_id = info : lanl - repo/isi/$000087027400013

Hansen, P., & O'Leary, D. (1993). The use of the l-curve in the regularization of discrete ill-posed problems. *SIAM Journal on Scientific Computing*, *14*(6), 1503.

Humphreys, E., Hessler, E., Dueker, K., Farmer, C. L., Erslev, E., & Atwater, T. (2003). How laramide-age hydration of north american lithosphere by the farallon slab controlled subsequent activity in the western united states. *INTERNATIONAL GEOLOGY REVIEW*, *45*(7), 575 – 595.

Hutchinson, M. F. (1990). A stochastic estimator of the trace of the influence matrix for laplacian smoothing splines. *COMMUNICATIONS IN STATISTICS-SIMULATION AND COMPUTATION*, *19*(2), 433–450.

Jasbinsek, J., Dueker, K., & Hansen, S. (2010). Characterizing the 410 km discontinuity low-velocity layer beneath the LA RISTRA array in the North American Southwest. *Geochemistry Geophysics Geosystems*, *11*(3), Q03008.

Jordan, T. (1981). Continents as a chemical boundary layer. *Philosophical Transactions of the Royal Society of London. Series A, Mathematical and Physical Sciences*, *301*(1461), 359.

KARATO, S. (1993). Importance of anelasticity in the interpretation of seismic tomography. *GEOPHYSICAL RESEARCH LETTERS*, *20*(15), 1623–1626.

Karato, S., & Jung, H. (1998). Water, partial melting and the origin of the seismic low velocity and high attenuation zone in the upper mantle. *Earth and Planetary Science Letters*, *157*(3-4), 193 – 207.
URL `http://www.sciencedirect.com/science/article/B6V61-3T1FD5P-6/2/072372874`

Karlstrom, K., & Bowring, S. (1988). Early Proterozoic assembly of tectonostratigraphic terranes in southwestern North America. *The Journal of Geology*, *96*(5), 561–576.

Karlstrom, K., & Humphreys, E. (1998). Persistent influence of Proterozoic accretionary boundaries in the tectonic evolution of southwestern North America: Interaction of cratonic grain and mantle modification events. *Rocky Mountain Geology*, *33*(2), 161.

Karlstrom, K., Whitmeyer, S., Dueker, K., Williams, M., Bowring, S., Levander, A., Humphreys, E., & Keller, G. (2005). Synthesis of results from the CD-ROM experiment: 4-D image of the lithosphere beneath the rocky mountains and implications for understanding the evolution of continental lithosnhere. *Geophysical monograph*, *154*, 421–441.

Karlstrom, K., et al. (2002). Structure and evolution of the lithosphere beneath the Rocky Mountains: Initial results from the CD-ROM experiment. *GSA Today*, *12*(3), 4–10.

Karlstrom, K. E., Crow, R., Crossey, L., Coblentz, D., & Van Wijk, J. W. (2008). Model for tectonically driven incision of the younger than 6 ma grand canyon. *Geology*, *36*(11), 835–838.
URL `http://geology.gsapubs.org/cgi/content/abstract/36/11/835`

Keller, G., KARISTROM, K., Williams, M., Miller, K., Andronicos, C., Levander, A., Snelson, C., & Prodehl, C. (2005). The dynamic nature of the continental crust-mantle boundary: Crustal evolution in the Southern Rocky Mountain region as an example. *Geophysical monograph*, *154*, 403–420.

Kennett, B. L. N., Engdahl, E. R., & Buland, R. (1995). Constrains on seismic velocities in the earth from travel-times. *Geophysical Journal International*, *122*(1), 108–124. Article 0956-540X Times Cited:350 Bibliography:15 English GJINEA A1995RG96900008 Copyright 2007 The Thomson Corporation.

Kluth, C., & Coney, P. (1981). Plate tectonics of the ancestral Rocky Mountains. *Geology*, *9*(1), 10.

Lee, C. T. A. (2003). Compositional variation of density and seismic velocities in natural peridotites at stp conditions: Implications for seismic imaging of compositional heterogeneities in the upper mantle. *JOURNAL OF GEOPHYSICAL RESEARCH-SOLID EARTH*, *108*(B9), 2441 –.
URL `http://linkseeker.lanl.gov/nmt?url`$_v$`er` $= Z39.88 - 2004ctx_v er = Z39.88 - 2004ctx_e nc = info : ofi/enc : UTF - 8rft_v al_f mt = info : ofi/fmt : kev : mtx : journalrft.genre = articlerft.issn = 0148 - 0227rft.coden = JGREA2rft.date = 2003rft.volume = 108rft.issue = b9rft.spage = 2441rft.atitle = Compositional + variation + of + density + and + seismic + velocities + in + natural + plications + for + seismic + imaging + of + +mantlerft.jtitle = JOURNAL + OF + GEOPHYSICAL + RESEARCHerft.auinit = CTArft.pub = AMER + GEOPHYSICAL + UNIONrft_i d = info : lanl - repo/isi/000185652100001$

Lee, D. K., & Grand, S. P. (1996). Upper mantle shear structure beneath the colorado rocky mountains. *JOURNAL OF GEOPHYSICAL RESEARCH-SOLID EARTH*, *101*(B10), 22233 – 22244.

Lees, J. M., & Vandecar, J. C. (1991). Seismic tomography constrained by bouguer gravity-anomalies - applications in western washington. *Pure and Applied Geophysics*, *135*(1), 31–52. Article 0033-4553 Times Cited:22 English PAGYAV A1991EZ28200003 Copyright 2007 The Thomson Corporation.

Lerner-Lam, A., Sheehan, A., Grand, S., Humphreys, E., Dueker, K., Hessler, E., Guo, H., Lee, D., & Savage, M. (1998). Deep structure beneath the southern Rocky Mountains from the Rocky Mountain Front broadband seismic experiment. *Rocky Mountain Geology*, *33*(2), 199.

Levander, A., Zelt, C., & Magnani, M. (2005). Crust and upper mantle velocity structure of the southern Rocky Mountains from the Jemez Lineament to the Cheyenne belt. *Geophysical monograph*, *154*, 293–308.

Li, A. B., Forsyth, D. W., & Fischer, K. M. (2002). Evidence for shallow isostatic compensation of the southern rocky mountains from rayleigh wave tomography. *Geology*, *30*(8), 683–686.

Li, C., van der Hilst, R. D., Engdahl, E. R., & Burdick, S. (2008a). A new global model for p wave speed variations in earth's mantle. *GEOCHEMISTRY GEOPHYSICS GEOSYSTEMS*, *9*, Q05018.

Li, Z., Lee, C., Peslier, A., Lenardic, A., & Mackwell, S. (2008b). Water contents in mantle xenoliths from the Colorado Plateau and vicinity: Implications for the mantle rheology and hydration-induced thinning of continental lithosphere. *Journal of Geophysical Research*, *113*(B9), B09210.

Lines, L., Schultz, A., & Treitel, S. (1988). Cooperative inversion of geophysical data. *Geophysics*, *53*, 8.

Livaccari, R., & Perry, F. (1993). Isotopic evidence for preservation of Cordilleran lithospheric mantle during the Sevier-Laramide orogeny, western United States. *Geology*, *21*(8), 719.

MacCarthy, J., Aster, R. C., Dueker, K., Hansen, S., & Borchers, B. (in prep). The structure of the lithosphere beneath the colorado rocky mountains and support for high elevations. *Journal of Geophysical Research (Solid Earth)*.

MacCarthy, J., Borchers, B., & Aster, R. (2010). Efficient stochastic estimation of the model resolution matrix diagonal and generalized cross validation for large geophysical inverse problems. *Geophysical Research Letters*, *(submitted)*.

Maceira, M., & Ammon, C. J. (2009). Joint inversion of surface wave velocity and gravity observations and its application to central asian basins shear velocity structure. *J. Geophys. Res.*, *114*.
URL `http://dx.doi.org/10.1029/2007JB005157`

MCCOY, A., KARLSTROM, K., SHAW, C., & WILLIAMS, M. (2005). The Proterozoic ancestry of the Colorado Mineral Belt: 1.4 Ga shear zone system in central Colorado. *Geophysical monograph*, *154*, 71–90.

McCoy, A., Roy, M., Trevino, L., & Keller, G. (2004). Gravity modeling of the Colorado Mineral Belt. *The Rocky Mountain Region: An Evolving Lithosphere: Tectonics, Geochemistry, and Geophysics, Geophys. Monogr. Ser*, *154*, 99–106.

McMillan, M., Heller, P., & Wing, S. (2006). History and causes of post-Laramide relief in the Rocky Mountain orogenic plateau. *GEOLOGICAL SOCIETY OF AMERICA BULLETIN*, *118*(3-4), 393–405.

McMillan, M. E., Angevine, C. L., & Heller, P. L. (2002). Postdepositional tilt of the miocene-pliocene ogallala group on the western great plains: Evidence of late cenozoic uplift of the rocky mountains. *Geology*, *30*(1), 63–66.
URL `http://geology.gsapubs.org/content/30/1/63.abstract`

Meltzer, A., Rudnick, R., Zeitler, P., Levander, A., Humphreys, G., Karlstrom, K., Ekstrom, G., Carlson, R., Dixon, T., Gurnis, M., et al. (1999). USArray initiative. *GSA Today*, *9*(11), 8–10.

Menke, W. (1989). *Geophysical Data Analysis: Discrete Inverse Theory*. Academic Press.

Montelli, R., Nolet, G., Masters, G., Dahlen, F. A., & Hung, S. H. (2004). Global p and pp traveltime tomography: rays versus waves. *Geophysical Journal International*, *158*(2), 637–654.
URL http://dx.doi.org/10.1111/j.1365-246X.2004.02346.x

Morgan, P. (2003). Colorado Plateau and Southern Rocky Mountains uplift and erosion. *Cenozoic systems of the Rocky Mountain region: Denver, Rocky Mountain Section SEPM (Society for Sedimentary Geology)*, (pp. 1–31).

Moschetti, M. P., Ritzwoller, M. H., Lin, F. C., & Yang, Y. (2010). Crustal shear wave velocity structure of the western united states inferred from ambient seismic noise and earthquake data. *J. Geophys. Res.*, *115*(B10).
URL http://dx.doi.org/10.1029/2010JB007448

Moucha, R., Forte, A. M., Rowley, D. B., Mitrovica, J. X., Simmons, N. A., & Grand, S. P. (2008). Mantle convection and the recent evolution of the colorado plateau and the rio grande rift valley. *Geology*, *36*(6), 439–442.

Moucha, R., Forte, A. M., Rowley, D. B., Mitrovica, J. X., Simmons, N. A., & Grand, S. P. (2009). Deep mantle forces and the uplift of the Colorado Plateau. *Geophysical Research Letters*, *36*(19), 19310–+.

Mutschler, F., Larson, E., & Gaskill, D. (1998). The Fate of the Colorado Plateau—A View from the Mantle. *US Geological Survey bulletin*, (pp. 203–222).

Nagy, D., Papp, G., & Benedek, J. (2000). The gravitational potential and its derivatives for the prism. *JOURNAL OF GEODESY*, *74*(7-8), 552–560.

Nolet, G., & Dahlen, F. (2000). Wave front healing and the evolution of seismic delay times. *Journal of Geophysical Research*, *105*(19), 043–19.

Nolet, G., Montelli, R., & Virieux, J. (1999). Explicit, approximate expressions for the resolution and a posteriori covariance of massive tomographic systems. *GEOPHYSICAL JOURNAL INTERNATIONAL*, *138*(1), 36–44.

Obrebski, M., Allen, R. M., Xue, M., & Hung, S. (2010). Slab-plume interaction beneath the Pacific Northwest. *Geophysical Research Letters*, *37*, 14305–+.

Owens, T., Crotwell, H., Groves, C., & Oliver-Paul, P. (2004). SOD: standing order for data. *Seismological Research Letters*, *75*(4), 515.

PAIGE, C. C., & SAUNDERS, M. A. (1982). Lsqr - an algorithm for sparse linear-equations and sparse least-squares. *ACM TRANSACTIONS ON MATHEMATICAL SOFTWARE*, *8*(1), 43–71.

Parker, R. (1994). *Geophysical Inverse Theory*. Princeton Univ. Press.

Parker, R. L. (1972). Inverse theory with grossly inadequate data. *Geophysical Journal of the Royal Astronomical Society*, *29*(2), 123–138.
URL http://dx.doi.org/10.1111/j.1365-246X.1972.tb02203.x

Parsons, T., Blakely, R. J., & Brocher, T. M. (2001). A simple algorithm for sequentially incorporating gravity observations in seismic traveltime tomography. *INTERNATIONAL GEOLOGY REVIEW*, *43*(12), 1073–1086.

Pavlis, G. L., & Vernon, F. L. (2010). Array processing of teleseismic body waves with the usarray. *Computers & Geosciences*, *36*(7), 910 – 920.
URL http://www.sciencedirect.com/science/article/B6V7D-4YXK4GR-1/2/22ae63712

Premo, W., & Van Schmus, W. (1989). Zircon geochronology of Precambrian rocks in southeastern Wyoming and northern Colorado. *Proterozoic geology of the southern Rocky Mountains: Geological Society of America Special Paper*, *235*, 13–32.

Reiter, M. (2008). Geothermal anomalies in the crust and upper mantle along southern rocky mountain transitions. *Geological Society of America Bulletin*, *120*(3/4), 431 – 441.
URL http://(targetURLDomain)proxyhost.nmt.edu:2048/(targetURLRemainer)

Richard, G., Iwamori, H., Suetsugu, D., Bina, C., Inoue, T., Wiens, D., & Jellinek, M. (2010). Stagnant slab, wet plumes and Cenozoic volcanism in East Asia. *Physics of the Earth and Planetary Interiors*.

Roy, M., Jordan, T. H., & Pederson, J. (2009). Colorado plateau magmatism and uplift by warming of heterogeneous lithosphere. *Nature*, *459*(7249), 978–982.
URL http://dx.doi.org/10.1038/nature08052

Roy, M., Kelley, S., Pazzaglia, F., Cather, S., & House, M. (2004). Middle tertiary buoyancy modification and its relationship to rock exhumation, cooling, and subsequent extension at the eastern margin of the colorado plateau. *GEOLOGY*, *32*(10), 925–928.

Savage, M. K., Sheehan, A. F., & LernerLam, A. (1996). Shear wave splitting across the rocky mountain front. *GEOPHYSICAL RESEARCH LETTERS*, *23*(17), 2267–2270.

Schmandt, B., & Humphreys, E. (2010). Complex subduction and small-scale convection revealed by body-wave tomography of the western united states upper mantle. *Earth and Planetary Science Letters*, *297*(3-4), 435 – 445.
URL http://www.sciencedirect.com/science/article/B6V61-50J9VXP-1/2/9c12456cb

Schmandt, B., & Humphreys, E. (2010). Seismic heterogeneity and small-scale convection in the southern California upper mantle. *Geochemistry, Geophysics, Geosystems*, *11*(5), 5004–+.
URL http://dx.doi.org/10.1029/2010GC003042

Schutt, D. L., & Lesher, C. E. (2006). Effects of melt depletion on the density and seismic velocity of garnet and spinel lherzolite. *JOURNAL OF GEOPHYSICAL RESEARCH-SOLID EARTH*, *111*(B5), B05401.

Shapiro, N., Campillo, M., Stehly, L., & Ritzwoller, M. (2005). High-resolution surface-wave tomography from ambient seismic noise. *Science*, *307*(5715), 1615.

Sheehan, A. F., Abers, G. A., Jones, C. H., & Lerner-Lam, A. L. (1995). Crustal thickness variations across the colorado rocky mountains from teleseismic receiver functions. *J. Geophys. Res.*, *100*(B10), 20391–20404.
URL http://dx.doi.org/10.1029/95JB01966

Simmons, N. A., Forte, A. M., & Grand, S. P. (2006). Constraining mantle flow with seismic and geodynamic data: A joint approach. *EARTH AND PLANETARY SCIENCE LETTERS*, *246*(1-2), 109–124.

Sine, C. R., Wilson, D., Gao, W., Grand, S. P., Aster, R., Ni, J., & Baldridge, W. S. (2008). Mantle structure beneath the western edge of the colorado plateau. *GEOPHYSICAL RESEARCH LETTERS*, *35*(10), L10303.

Smith, D. (2000). Insights into the evolution of the uppermost continental mantle from xenolith localities on and near the Colorado Plateau and regional comparisons. *Journal of Geophysical research*, *105*(B7), 16769.

Snelson, C., Keller, G., Miller, K., Rumpel, H., & Prodehl, C. (2005). Regional crustal structure derived from the CD-ROM 99 seismic refraction/wide-angle reflection profile: The lower crust and upper mantle. *Geophysical monograph*, *154*, 271–291.

Song, T., Helmberger, D., & Grand, S. (2004). Low-velocity zone atop the 410-km seismic discontinuity in the northwestern United States. *Nature*, *427*(6974), 530–533.

Song, T. R., & Helmberger, D. V. (2007). Validating tomographic model with broad-band waveform modelling: an example from the la ristra transect in the southwestern united states. *Geophysical Journal International*, *171*(1), 244–258.
URL http://dx.doi.org/10.1111/j.1365-246X.2007.03508.x

Spencer, J. E. (1996). Uplift of the colorado plateau due to lithosphere attenuation during laramide low-angle subduction. *JOURNAL OF GEOPHYSICAL RESEARCH-SOLID EARTH*, *101*(B6), 13595–13609.

Spetzler, J., & Snieder, R. (2004). The fresnel volume and transmitted waves. *Geophysics*, *69*(3), 653–663.

Steck, L. K., Phillips, W. S., Begnaud, M., & Stead, R. (2009). Tomography of pg and sg across the western united states using usarray data. *Eos Trans AGU Trans. AGU*, *90*(52), Fall Meet. Suppl., Abstract U53B–0075.

Tiberi, C., Deschamps, A., Deverchere, J., Petit, C., Perrot, J., Appriou, D., Mordvinova, V., Dugaarma, T., Ulzibaat, M., & Artemiev, A. A. (2008). Asthenospheric imprints on the lithosphere in central mongolia and southern siberia from a joint inversion of gravity and seismology (mobal experiment). *GEOPHYSICAL JOURNAL INTERNATIONAL*, *175*(3), 1283–1297.

Tiberi, C., Diament, M., Deverchere, J., Petit-Mariani, C., Mikhailov, V., Tikhotsky, S., & Achauer, U. (2003). Deep structure of the baikal rift zone revealed by joint inversion of gravity and seismology - art. no. 2133. *Journal of Geophysical Research-Solid Earth*, *108*(B3), 2133–2133. Article 0148-0227 Times Cited:4 Bibliography:65 English JGREA2 000182146400007 Copyright 2007 The Thomson Corporation.

Tweto, O., & Sims, P. (1963). Precambrian ancestry of the Colorado mineral belt. *Geological Society of America Bulletin*, *74*(8), 991.

Van der Lee, S., & Nolet, G. (1997). Upper mantle S velocity structure of North America. *Journal of Geophysical Research*, *102*(B10), 22815.

van Wijk, J. W., Baldridge, W. S., van Hunen, J., Goes, S., Aster, R., Coblentz, D. D., Grand, S. P., & Ni, J. (2010). Small-scale convection at the edge of the colorado plateau: Implications for topography, magmatism, and evolution of proterozoic lithosphere. *GEOLOGY*, *38*(7), 611–614.

Vandecar, J. C., & Crosson, R. S. (1990). Determination of teleseismic relative phase arrival times using multi-channel cross-correlation and least squares. *Bulletin of the Seismological Society of America*, *80*(1), 150–169.

Waite, G., Smith, R., & Allen, R. (2006). VP and VS structure of the Yellowstone hot spot from teleseismic tomography: Evidence for an upper mantle plume. *Journal of Geophysical Research*, *111*(B4), B04303.

Waldhauser, F., Lippitsch, R., Kissling, E., & Ansorge, J. (2002). High-resolution teleseismic tomography of upper-mantle structure using an a priori three-dimensional crustal model. *Geophysical Journal International*, *150*(2), 403–414.

Whitmeyer, S. J., & Karlstrom, K. E. (2007). Tectonic model for the proterozoic growth of north america. *GEOSPHERE*, *3*(4), 220–259.

Wilson, D., Leon, J., Aster, R., Ni, J., Schlue, J., Grand, S., Semken, S., Baldridge, S., & Gao, W. (2002). Broadband Seismic Background Noise at Temporary Seismic Stations Observed on a Regional Scale in the Southwestern United States. *BULLETIN OF THE SEISMOLOGICAL SOCIETY OF AMERICA*, *92*(8), 3335–3342.
URL `http://www.bssaonline.org/cgi/content/abstract/92/8/3335`

Xue, M., & Allen, R. M. (2010). Mantle structure beneath the western united states and its implications for convection processes. *J. Geophys. Res.*, *115*(B7).
URL `http://dx.doi.org/10.1029/2008JB006079`

Yao, Z. S., Roberts, R. G., & Tryggvason, A. (1999). Calculating resolution and covariance matrices for seismic tomography with the lsqr method. *GEOPHYSICAL JOURNAL INTERNATIONAL*, *138*(3), 886–894.

Yuan, H., & Dueker, K. (2005). Upper mantle tomographic Vp and Vs images of the Rocky Mountains in Wyoming, Colorado and New Mexico: evidence for a thick heterogeneous chemical lithosphere. *Geophys. Monogr*, *154*, 329–345.

Yuan, H., & Romanowicz, B. (2010a). Depth dependent azimuthal anisotropy in the western us upper mantle. *Earth and Planetary Science Letters*, *(submitted)*.

Yuan, H., & Romanowicz, B. (2010b). Lithospheric layering in the north american craton. *Nature*, *(submitted)*.

Zeyen, H., & Achauer, U. (1997). Joint Inversion of Teleseismic Delay Times and Gravity Anomaly Data for Regional Structures. Theory and Synthetic Examples. *NATO ASI SERIES 1 DISARMAMENT TECHNOLOGIES*, *17*, 155–168.

Zhang, H., & Thurber, C. H. (2007). Estimating the model resolution matrix for large seismic tomography problems based on lanczos bidiagonalization with partial reorthogonalization. *GEOPHYSICAL JOURNAL INTERNATIONAL*, *170*(1), 337–345.

Zhang, J., & McMechan, G. A. (1995). Estimation of resolution and covariance for large matrix inversions. *GEOPHYSICAL JOURNAL INTERNATIONAL*, *121*(2), 409–426.

Zhou, H., & Wang, H. (1994). A revisit to P wave travel time statics at teleseismic stations. *Journal of Geophysical Research*, *99*(B9), 17849.